DESIGN OF AN EXPERIMENTAL FACILITY

FOR FROST GROWTH STUDY

IN MICROCHANNEL

HEAT EXCHANGERS

By

SHANSHAN CAI

Bachelor of Science in Building Environment

and Equipment Engineering

Huazhong University of Science and Technology

Wuhan, China

2007

Submitted to the Faculty of the
Graduate College of the
Oklahoma State University
in partial fulfillment of
the requirements for
the Degree of
MASTER OF SCIENCE
in Mechanical Engineering
July, 2009

DESIGN OF AN EXPERIMENTAL FACILITY

FOR FROST GROWTH STUDY

IN MICROCHANNEL

HEAT EXCHANGERS

Thesis Approved:

Dr. Lorenzo Cremaschi

Thesis Adviser

Dr. Jeffrey D. Spitler

Dr. Daniel E. Fisher

Dr. A. Gordon Emslie

Dean of the Graduate College

ACKNOWLEDGMENTS

TABLE OF CONTENTS

LIST OF TABLES

LIST OF FIGURES

NOMENCLATURE

A	Area
C	Capacitance Rate
c	Specific Heat
cfm	Cubic Feet per Minute
D	Diameter
DAQ	Data Acquisition System
f	Friction Factor
FPI	Fin per Inch
fpm	Feet per Minute
G_c	Mass Flux at Minimum Flow Area
gpd	Gallon per Day
gpm	Gallon per Minute
h	Enthalpy
h_{in}	Inside Heat Transfer Coefficient
h_{out}	Outside Heat Transfer Coefficient
j	Colburn j Factor
k	Conductivity
L	Length
m	Mass Flow Rate

MCHX	Microchannel Heat Exchanger
N	Circuits Number
NTU	Number of Transfer Units
Nu	Nusselt Number
NPSHA	Available Net Positive Suction Head
NPSHR	Required Net Positive Suction Head
P	Pressure
Pr	Prandtl Number
Q	Flow Rate
Q_{dot}	Heat Transfer Rate
R	Row number
Re	Reynolds Number
RH	Relative Humidity
RMS	Root Mean Square
RPM	Revolutions per Minute
SSM	Sample System Module
T	Temperature
U	Total Heat Transfer Coefficient
v	Velocity
VFD	Variable Frequency Drive

Greek Symbols

ε	Effectiveness

η	Efficiency
ρ	Density
δ	Thickness

Subscripts

a	Air
in	Inside
out	Outside
ref	Refrigerant
surf	Surface

CHAPTER I

INTRODUCTION

Energy consumption in residential and commercial buildings is an important aspect for energy costs and environmental concerns on a global scale. In recent years, novel technologies that promote a rational usage of the energy, reduce the global warming emissions, utilize alternative energy sources, and reduce the energy operational cost of buildings are receiving more and more attention.

Heat pumps are devices that have an increased efficiency when compared to other traditional heating methods and they are often employed to provide both cooling and heating to the building. However, before their expanded implementation in residential and commercial applications, these systems need to become more energy efficient, reliable, and more cost-effective in retrofit applications.

Microchannel heat exchangers have the potential for a cost-effective increase of the heat exchanger performance and for a 'packed-in' solution that can be adopted by the heat pump system industry to provide heating and cooling. Microchannel heat exchangers are compact because they consist of arrays of flat multi-port tubes and louvered fins. These elements enhance the heat transfer performance while maintaining small internal volume for the refrigerant charge inventory. They are usually made of Aluminum, which makes them resistant to corrosion, suitable for high pressure applications and formable in

extrusion manufacturing processes. In addition, they are smaller and lighter than conventional fin-and–tube heat exchangers currently used in commercial heat pump systems.

Microchannel heat exchangers (MCHXs) have been widely used in air conditioning, refrigeration and heat pump systems due to their better performance as condensers. Compared to traditional fin-and-tube heat exchangers, microchannel coil has a more compact configuration. With multi-ports, in the same coil size, MCHXs come out with a larger surface area, which lead to higher heat transfer rates.

Although several researchers have investigated microchannel heat exchangers in air conditioners for residential applications, the question of whether or not microchannels are suitable in outdoor evaporator coils of heat pump systems is still open.

Figure 1.1 shows a schematic of a microchannel heat exchanger with louvered folded fins used in heat pump systems. This heat exchanger consists of one refrigerant passage in a straight vertical orientation, which means that the refrigerant flows inside the microchannels tubes in the vertical direction. The air flows across the surface of louvered folded fins as shown in Figure 1.1 c. During the cooling season, the heat exchanger works as an outdoor condenser, in which refrigerant vapor condenses to liquid by rejecting heat to the outdoor environment. In a heat pump system the same heat exchanger would work as the outdoor evaporator coil during the heating season. In this condition, a 2-phase mixture of vapor and liquid refrigerant entering the evaporator is brought to a superheated vapor by absorbing heat from the outdoor air. Often, vertical microchannel orientation provides better drainage of the water condensate on the coil during the heating season. Furthermore, the 2-phase refrigerant mixture enters the outdoor coil from the

bottom header to avoid possible stagnation of liquid refrigerant in the top header. The design and development of these heat exchangers must take into account the refrigerant distribution, the frost growth, the water condensate retention, the energy impact of the heat exchanger on the overall system performance, the dynamic performance as well as the cost and manufacturability of the coil.

Refrigerant Flow
Microchannel Ports
Louvered fins
Air Flow
(c) Microchannel and Fins
(d) Heat Exchanger Top Header Detail
Refrigerant flow out
Refrigerant flow in
(b) Heat Exchanger Bottom Header Detail
(a) Microchannel Heat Exchanger
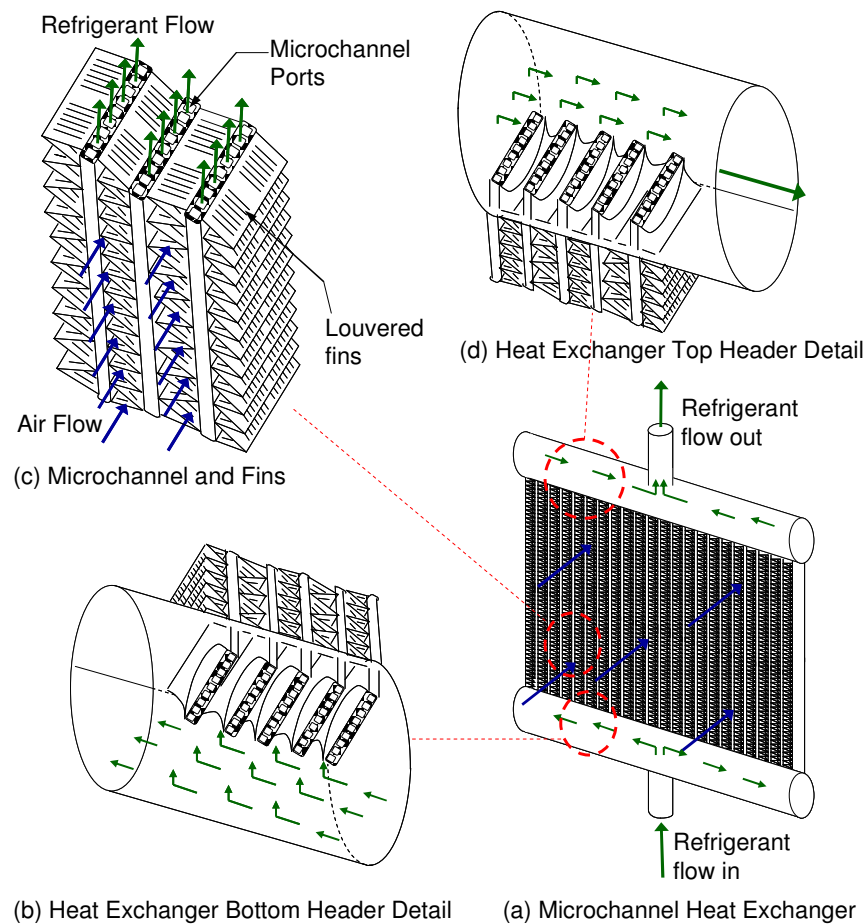
Figure 1.1 Microchannel coil schematic

One of the main issues with this type of heat exchanger is condensate retention and frost nucleation on porous heat transfer surfaces, when MCHXs are used as outdoor evaporators in the heating mode. Condensate and frost accumulated among the fins and

tubes works as thermal insulation between the coil surface and the humid air, greatly hit the heat exchanger performance. Frost accumulation also leads to a blockage problem. With a narrower air passage, the total heat transfer coefficient drops dramatically and air pressure loss increases significantly.

There are several parameters that are affected by frost formation on the outdoor coils. While, researchers investigated this issue in conventional fin-and-tube coils, the impact of frost formation on microchannel coils of the heat pump systems is not well reported in the literature. Most researchers investigated MCHXs under dry and wet conditions only for limited ranges of geometries and operating conditions. When it comes to the frost conditions, researchers focused more on the performance of fin-and-tube heat exchangers. Little or no information is found that provide guidelines to design MCHXs under frost conditions. If these coils are adopted by the heat pump industry, it is difficult to characterize both air side and refrigerant side heat transfer performance under cold and wet frosting conditions.

The work presented in this thesis is part of a broader program that seek to develop a new microchannel heat exchanger that can be used as the outdoor evaporator coil in compact heat pump systems for residential and commercial applications. This research program started in 2007 and it consists of a three-year joint collaboration between Oklahoma State University (Stillwater, OK), Johnson Controls, Inc. Building Efficiency Division, (JCI, Norman, OK), and the Oklahoma Center for Advancement in Science and Technology (OCAST). The project aims to advance the technology of fin folded microchannel heat exchangers and address the main challenges that arise when these heat exchangers are used as outdoor evaporator coils in R22 and R410A systems. Both

modeling and experimental efforts are currently ongoing and they will provide the basic research required to address three significant problems related to the adoption of microchannel heat exchangers:

a) refrigerant maldistribution inside the heat exchangers,

b) water condensate buildup on the coils,

c) frost buildup leading to long defrost cycles

In addition, a physics-based semi-empirical model of outdoor microchannel evaporator coils is under development. Using the results from the experiments and the simulations, a microchannel coil prototype will be designed, manufactured, and tested in the third and final year of the project. The project brings together a research team that successfully collaborated to develop the heat pump simulation and design program currently used by JCI Unitary Products Division engineers.

I was involved with the entire team work but my specific tasks were to design, build, and upgrade the air flow lab wind tunnel at Oklahoma State University. This experimental facility serves to collect data of frost and defrost performance for a broad range of heat exchanger geometries and operating conditions. The data will be then used to experimentally validated models and provide design recommendations of frost-less microchannel heat exchanges.

1.2 RESEARCH OBJECTIVES

Overall, the scope of the project is to increase the energy efficiency of the entire heat pump system by the optimal application of microchannel technology. My thesis focuses on the experimental facility developed to conduct research laboratory measurements of frost nucleation and condensate retention in fin-and-tube and microchannel small scale

heat exchangers. With respect to my part of the project, three main objectives of the work presented in this thesis are listed as follows:

➢ To develop an experimental methodology to investigate the frost and defrost thermal hydraulic performances of louvered folded fin microchannel heat exchangers under initial cycle, defrost cycle, and subsequent re-frost cycles conditions. In particular these heat exchangers must be exposed in our laboratory to the same operating conditions as in the field of air-source heat pump systems for residential and commercial applications

➢ To design, build, upgrade, and calibrate the air flow laboratory wind tunnel in order to simulate heat pump operating conditions during frosting (heating) periods and defrost cycles.

➢ To provide a complete and throughout uncertainty analysis of the experimental methodology and provide guidance of the range of the independent variables that could be controlled by using this new experimental set up

1.3 OVERVIEW OF THE THESIS

This thesis contains six chapters.

Frost accumulation study is described in chapter 2. This chapter also gives a brief overview of recent experimental methods and facility design for frost test, either on fin-and-tube heat exchangers, or MCHXs.

Chapter 3 is a detailed explanation of the design work that has been done in the air flow lab. The whole design can be divided to three main parts: air loop design, refrigerant design and frost weighing system design. Design guidelines, equipment selection and performance comparison are separately discussed.

Based on the equipment and instrumentation, uncertainty of the system is analyzed in chapter 4. Two coil models were created according to fin-and-tube and microchannel configuration. The uncertainty on total heat transfer coefficient (U) and air-side heat transfer coefficient (h_{out}) were calculated. Recommended measuring ranges are obtained from the results of uncertainty models.

In chapter 5, Refrigeration coil model and dehumidification process are analyzed by using preliminary experimental test data. Based on the data analysis, different ways are suggested for calibration and facility improvement.

Conclusions for the range of the experimental conditions attainable with this facility are drawn in chapter 6 based on previous chapters. Another group data shows the results after calibration. Future work is also listed in this chapter for broadening the range of experimental conditions if this facility could be extended further. Start-up, run and shut-off procedures of Labview program and chiller are detailed described in Appendices. This thesis and its appendixes will serve also as references for operating the low temperature wind tunnel in the air flow laboratory at OSU.

CHAPTER II

REVIEW OF LITERATURE

Since frosting is a transient phenomenon in which both heat transfer and mass transfer simultaneously take place, the question of how frost growth affects the heat pump system performance and its reliability is not trivial. The addition of a porous layer of air and ice in addition to the normal air-side and refrigerant side parameters makes the theoretical analysis difficult (Ohkubo, 2006).

There are several parameters that are affected by frost formation on outdoor coils. Peng et al. (2003) investigated the behavior of an air-source heat pump with a fin-and-tube heat exchanger operating under frosting and defrosting conditions. A similar investigation was performed more recently by Guo et al. (2006), in which they consider the effects of outdoor air temperature and relative humidity on the frost accumulation of a fin-and-tube outdoor coil and on the dynamic heating capacity of an air source heat pump system. While several researchers investigated this issue in conventional fin-and-tube coils, the impact of frost formation on outdoor microchannel evaporators is not fully understood in the open literature. Few examples can be found in the work presented by Kim and Groll (2003). Frost growth and the frequency of the defrost cycles were considered the major factors in determining system performance. They concluded that water condensate drainage removal during the defrost cycles needed to be improved and that the manifolds

should be designed for more even refrigerant distribution.

In the next sections, the literature reviewed is summarized and divided in two categories: relevant experimental facilities under frost conditions and variables to be considered when studying frost accumulation on heat exchangers. As mentioned before, the review of the literature in this field shows that a large number of researches focused on fin-and-tube heat exchangers, while little work has been done on MCHXs, especially under frost conditions.

2.1 VARIABLES THAT IMPACT THE FROST ACCUMULATION

Numerous factors are reported which would influence frost growth during the frost cycle. Air side, refrigerant side parameters and fin geometry all have their own effects to the frost formation.

Lee and Ro (2002) studied the influence of the air humidity, velocity, inlet air temperature and the surface temperature to the frost formation on a flat plate, and validate the empirical frost thickness and density correlations. In their experiments, a CCD camera was used to estimate the frost thickness. Frost on the surface was scraped off at the end of each experiment and weighed in a balance. Lee's results showed air humidity and surface temperature are two dominant parameters for frost accumulation. Higher humidity ratios lead to a thicker frost layer, while lower surface temperature causes a denser one. These results reached an agreement with Kondepudi and O'Neal's conclusion for fin-and-tube heat exchangers.

Kondepudi and O'Neal (1989) conducted frost experiments on louvered folded finned tube heat exchanger in 1989. Their experiment results showed higher relative humidity led to a more obvious frost accumulation. In 80% relative humidity (RH)

9

ambient air, over 2.5 times more frost mass was recorded, compared to 60% RH air at the end of 50min time interval of the measurements. Air velocity was another factor mentioned in Kondepudi and O'Neal's work. They reported that a 53% increase in the face velocity would give approximate 28% more frost deposition. Pressure drop also changed with humidity, fin spacing and face velocity. They believed fin geometry would have an extremely strong effect. Humidity of the air, air velocity and the fin spacing are all important factors on frost growth.

Seker et al. (2002) conducted various tests on frost of traditional fin-and-tube heat exchangers. They mentioned the thermal conductivity of frost was determined by the density and the frost formation process could be simplified with the following assumptions:

➢ The temperature of all surface points are below freezing point;

➢ The process is quasi-steady-state;

➢ Frost distribution is homogenous and uniform;

➢ Frost thermal conductivity only is the function of density;

➢ Neglect radiation;

➢ One dimensional heat and mass transfer

Seker's experiments looked into the effect of air temperature, surface temperature and relative humidity. Higher inlet air temperature and lower surface temperature caused an increase in the frost thickness and larger pressure drop, where the surface temperature gave remarkable changes. Seker also found there was a higher heat transfer coefficient when increasing the air relative humidity, which is similar to Rita and Kondepudi's (1989) results. They also reached a consistence on the effect of the air mass flow rate.

Higher air mass flow rate brought in severer frost accumulation and larger pressure drop by increasing total heat transfer rate.

Yan et al. (2005) found a contradiction to this point, when they compared their results with Kondepudi and O'Neal, Rite and Crawford's. During their frost experiments for finned tube coil, more frost accumulation was observed when air flow decreased. They discussed the phenomenon and thought the reason was a lower surface temperature. However, both Rite and Seker reported that higher air flow rate increased frost thickness, pressure drop and total heat transfer coefficient at the same time. Kondepudi gave detailed information that higher air flow rate would first increased the total heat transfer coefficient, then decreased. In spite of the air flow rate, Yan et al. also found other parameters that could affect fin-and-tube heat exchanger performance, including air temperature, humidity ratio, surface temperature and fin pitch and row number. They came to the conclusion that i) moisture effect is more important than surface temperature; ii) fin pitch would not effect significantly on frost amount; iii) the row number may have an effect due to different geometry of the heat exchanger (thickness in the flow direction).

Na and Webb (2003) paid more attention to the frost deposition and growth. Frost growth should be treated as two parts: volume growth and densification. In their model, accurate mass transfer rate balances should be the preliminary request to reach an accurate result on frost accumulation. They pointed our that a large number of previous models for frost accumulation on heat exchangers are valid only based on specific assumptions, like the one that water vapor around the frost section was actually saturated. Some of those assumptions appeared to be inaccurate to some degree. The chemical

potential difference between water and air determines the growth of frost. Based on Fletcher's equation:

$$v = K \exp[-A/\ln(P_V/P_{VS})]$$

where K and A are constant, $P_V/P_{VS} = (1+S)$, v represents ice crystal growth velocity and S is the supersaturated ratio. Thus, if there is a frost growth, which means v is an increasing function, P_V/P_{VS} must be larger than 1. So in actual frost growth process, water vapor is supersaturated around the thermal boundary layers of the fins. By validating in his model, they recommended Prager correlation for frost growth rate and densification analysis.

Ogawa et al. (1993) studied the performance improvements for plate fin-and-tube heat exchanger under frost conditions. Instead of looking into air and refrigerant side factors, he started a new study on the fin geometry effect. They believed leading edge effect gave a dilemma in the heat exchanger design. Due to the large heat transfer coefficient, the frost layer grows quickly at the leading edge, and the air flow begins to be blocked. Compared to the leading edge, the rear part of the heat exchanger has less frost accumulation. Because of the blockage in the front row of the coil, the air stream hardly reaches the rear part of the fins. These rear sections of the fins do not contribute markedly to the total heat transfer coefficient of the fin. Ogawa et al. believed that it would be better if fresh air is bypassed to the rear part of the heat exchanger to decrease the ratio of blockage. Then they suggested adopting fin staging. Staging means arranging fins in different sizes. In their experiments, they tried with front staging, side staging, fin width extension and partial cutting of fins. In front staging, there is a large fin spacing in the front, followed by a narrow one in the back. This fin staging efficiently decreased airflow

blockage in the leading edge, and meanwhile reduced the pressure drop. Side staging was guided part of the fresh air to the rear of the heat exchanger by side cutting of the front fin. It brought advantages because it promoted heat transfer rate in the back. Ogawa's results showed by combining front staging with side staging give an overall higher heat transfer rate, with a lower pressure drop. The third type of fin staging that Ogawa investigated was fin width extension. Due to the larger area before the coil tube, higher surface temperatures were achieved, leading to less air flow blockage and frost accumulation. Partial cutting was similar to front staging and it promoted frost piled around the tube, eliminating serious blockage problem.

Based on Ogawa's study, Watters specified the experiments on a two-row heat pump evaporator under frost condition. Watters's results showed fin staging can improve the cycle time, but reduce the benefit in COP at the same time. The 15/25 coil Watters used had a 76% longer time period than 20/20 baseline coil. But the COP was increased by only 4%. Watters believed some fin staging manufacturing techniques need to be investigated if engineers want to take full benefit from different fin geometries. Frost height measuring method also needs to be improved since the observed data were not enough and interior frost conditions could not be measured during the experiments.

Kim and Groll (2003) conducted several cooling tests before running the heat exchanger under frost conditions in the heating mode. In the cooling tests, they found that the orientation of the coil and the fin per inch (FPI) had an effect on the overall system performance. Different orientation represents diverse airflow patterns through the fins. Results showed that a slanted installed coil could provide higher capacities than the vertical heat exchangers with the same fin density. Kim et al. (2001) pointed out the heat

transfer coefficient depended on the airflow turning angle, which was determined by the fin spacing when the angle was greater than 45º. By comparing between the heat exchanger with 20 FPI and 15 FPI in both angular and vertical configuration, they believed the airflow patterns of the inlet and outlet of the fins were the major factors to the system performance. In the heating tests, Kim and Groll concluded the microchannel sample units ran continuously for about half an hour before the first defrost cycle. After that, the frosting cycle time period decreased and longer period was recorded for complete defrosting of the coils. Uneven frost on the front surface of the heat exchanger also indicated a refrigerant mal-distribution issue. Kim and Groll suggested a careful designed baffle could improve the refrigerant distribution. Orientation of the coil caused a more obvious effect than FPI. With a more normal air flow to the surface, a higher capacity can be reached. However, the frequency of defrost cycle will be increased at the same time.

Song et al. (2002) did a research on the refrigerant distribution in MCHXs. They found that it was the mal-distribution problem that usually caused the experimental date quite inconsistent with the model results. From their results, a vertical header was reported that should help enhancing refrigerant distribution. For the two-phase refrigerant, inlet quality results in different frost distribution. By testing with the quality in the header varied from 0.10 to 0.85, they came to the conclusion that lower quality gave a more uniform frost, demonstrating a better distribution.

Xia et al. (2005) studied louvered folded fin microchannel coil under frosting, defrosting and refrosting conditions. It was found that both total heat transfer coefficient

and pressure drop did not change significant after the third frost cycle. Xia et al. concluded there was a periodic characteristic after the third or fourth cycle.

Padhmanabhan et al. (2008) focused on measuring frost and defrost periods for both microchannel and fin-and-tube heat exchanger and they recorded the amount of frost mass accumulated during the heating (frosting) period and the amount of watere drained during the defrost period. Their results showed that when starting from a dry condition, the frost time of MCHX was 25% less than the fin-and-tube heat exchanger. If both of them start from steady periodic conditions, MCHX performs even worse, and the frost cycle time is almost 50% shorter than the one for the fin-and-tube coil. From their experiments, the starting condition of fin-and-tube coil does not affect frost accumulation much, only 4% difference in frost cycle time between dry and wet condition, while for MCHX, the frost time will be 60% longer if it starts from dry condition. They also looked into the effect of water retention on the frost accumulation by blowing Nitrogen gas towards the coils right after the defrost cycle ends. In this way, almost 95% of the remaining water was forced away from the coil, while in actual cycle, only 85% water drains out of the coil. Comparing the frost growth rate between Nitrogen gas defrost cycles and actual defrost cycles, they found that the absolute amount of water mass residual retained in the microchannel coil does not affect much the amount of frost accumulation and the frost cycle time. The authors pointed out that the initial frost nucleation is the predominant root cause of short frost cycles in micrichannel coils.

2.2 EXPERIMENTAL FACILITIES FOR THE PERFORMANCE OF HEAT EXCHANGERS UNDER FROST CONDITIONS

An experimental investigation of the effects of frost growth on the performance of tube heat exchangers with louvered fins has been conducted by Kondepudi in 1988. Figure 2.1 illustrates the schematic of the experimental arrangement and corresponding state points in psychrometric diagram. When the air comes out of the testing coil, it is at a lower temperature and humidity. By passing the cooling coil, both the temperature and humidity is further reduced. Then, a primary saturation system was used to increase the humidity, making the air saturated. The dry bulb temperature was controlled by resistance heaters. The secondary saturation system was adjusted to achieve desired humidity levels.
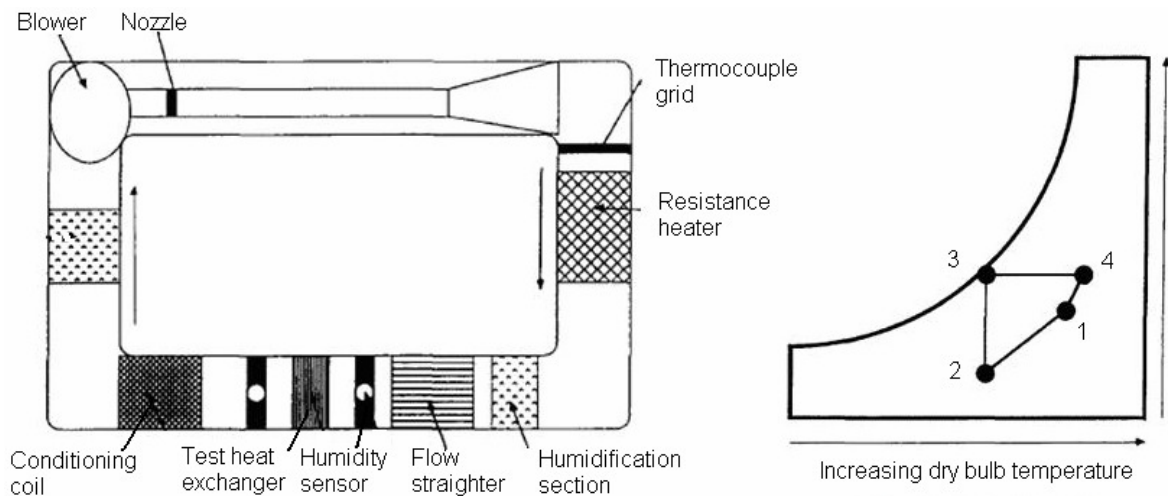
Figure 2.1 Schematic of Kondepudi (1988) experimental arrangement and

Psychrometric process

Because of the extreme low temperature range, water can not be used as refrigerant inside the cooling coils. In Kondepudi's work, they used 50% ethylene glycol-water mixture, which was circulated between the heat exchanger and the tank. The mass flow rate would be adjusted to keep the temperature inside the heat exchanger constant.

Since they preferred to looking into air side effect, relative humidity was changed from 60% to 85%, while the air velocity was in a range between 125ft/min and 250ft/min, provided by a centrifugal blower. In Kondepudi and O'Neal's experiment, frost accumulation was estimated by measuring inlet and outlet absolute air humidity. By the end of the experiment, the value was checked with the weight of condensate. However, this method gave a 20% discrepancy with the calculated value due to two main, inevitable reasons:

a) Partial vaporization of the condensate;

b) Surface tension and fin effect. Especially in those high fin density heat exchangers, condensate would be trapped between fins.

Watters et al. (2002) specified the experiment on a two-row heat pump evaporator under frost condition. The test facility included five major components: psychrometric rooms, test heat pump, indoor test part, outdoor test part and data acquisition system.
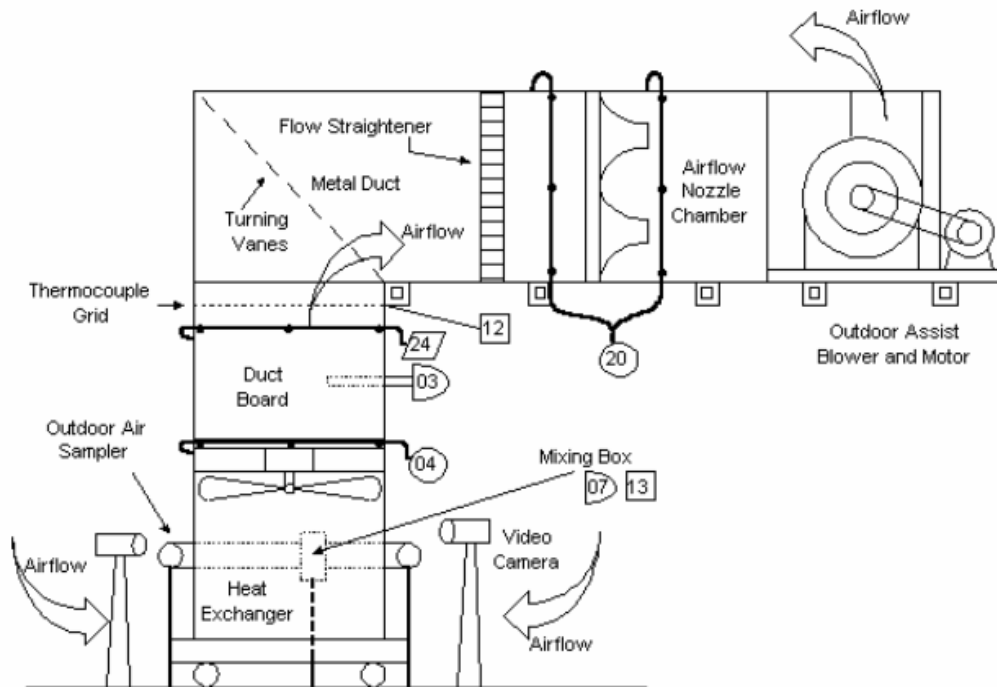
Figure 2.2   Outdoor equipment and instrumentation (Watters et al. 2002)

Figure 2.2 showed outdoor room equipment and instrumentation of Watter's work. Inside the indoor chamber, a three-row, three-circuit coil was used. With a blower and damper combination system, the flow rate was maintained constant. A flow chamber was designed according to relevant standards to measure the flow rate. The outdoor chamber was the main section to observe frost. At the outlet of the coil, the static pressure was measured. This readout helps adjust the flow rate of the assist blower to keep the value always zero when frost began to form. Inlet air temperature and relative humidity were measured by one thermocouple and a RH sensor, while the exit air temperature was measured by a 6-node thermocouple grid. Another RH sensor was set in the downstream ductwork to calculate exit air relative humidity. The RH sensor was a check of the chilled mirror set in the indoor chamber. A flow straighter was designed between the thermocouple grid and flow chamber to solve the uniform problem. Frost heights were read from CCD camera at three locations of the coil.

Kim et al. (2003) compared the performance between microchannel and fin-and-tube coils in a unitary split system. Two psychrometric rooms were constructed to simulate actual indoor and outdoor conditions. Air temperatures of the environmental rooms could be adjusted by a direct expansion refrigeration system, together with an electric heater. The humidity in the rooms was controlled by a steam humidifier. Two heat exchangers, which were placed separately in the environmental rooms, were included in the loop. A nozzle apparatus was built in with the ASHRAE stand 116-1983. This instrument could measure the air flow rate with an uncertainty around ±0.24%. Evenly placed thermocouple grid was used to measure inlet and outlet air temperature through the heat exchangers. A microprocessor-based hygrometer read the dew points

with the sampling devices placed in front of and behind the test section. Kim selected R-22 according to its better performance in the previous test. Eight thermocouples with an accuracy of ± 1.8 ℉ (± 3.5 ℃) were submerged in the refrigerant to measure the fluid temperature.

In Kim's experiment, the frosting and defrost time for each cycle was tested, and the overall performances were compared among four different types of heat exchangers. Temperature-based defrost controller was designed to determine whether a defrost cycle was required or not. Compared to time-based defrost controller, temperature-based is more efficient and reliable.

Xia et al. (2006) constructed a wind tunnel to look into the performance of specific louvered-fin, flat-tube heat exchangers with sequential frost growth cycles. The experimental facility is shown in Figure 2.3.

Figure 2.3 Facility schematic of Xia's work (2006)

They suspended the heat exchanger on an electronic balance in the access section of the wind tunnel. A soft connection sealed the interval between heat exchanger and the inlet of the wind tunnel. Thus, they were able to measure the accumulated frost mass and measure the residual water during defrost cycle. A precooler helped to reach the desired temperature prior to the initiation of an experiment. During initial experiment, the precooler kept cooling down the air temperature before started the refrigerant cycle, until reached the desired temperature. The air flow was adjusted by a variable speed blower and the flow rate was measured by pressure drop across the standard nozzle. The air temperature was measured with type-T thermocouple which was placed at the inlet of the coil. Humidifier was connected to adjust humidity according to the readout of a chilled mirror. Both thermocouple and humidifier are connected to the PID controller. The fluid used in the refrigerant side was ethyl alcohol. An electric heater and a PID controller regulated the refrigerant temperature. Immersion thermocouple probes and Coriolis mass flow meter measured relevant parameters at the inlet and outlet of the heat exchanger.

Inlet air temperature, inlet refrigerant temperature, inlet air humidity and refrigerant mass flow rate were constant in Xia's experiment.

Figure 2.4 gives the method Xia used for weighing condensate retention during wet-surface experiments. The heat exchanger was suspended under a electronic scale. Gaps between test section and the heat exchanger were sealed by plastic films to prevent air leakage without introducing vertical friction. A flexible hose was used in refrigerant line to minimize influence on the weighing process. Results was sent and recorded automatically in a PC.
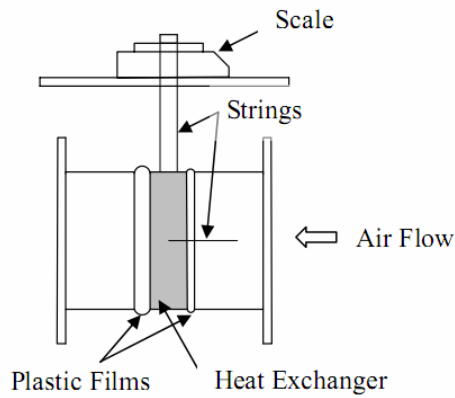
Figure 2.4 Schematic diagram of the test section for dynamic retention tests

(Xia et al., 2005)

Lee and Ro (2002) mentioned another way for frost measurement in their experimental study of frost formation on a horizontal cylinder. The apparatus is shown in figure 2.4. The way they used to measure surface temperature and thickness was a direct contact by attaching the thermocouple to the end of the micrometer, which was tipped parallel to the frost surface.
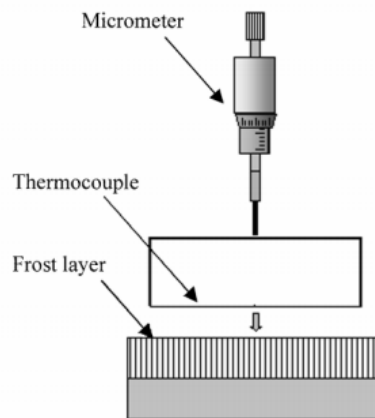
Figure 2.5 Frost measurement apparatus (Lee and Ro, 2002)

Padhmanabhan et al. (2008) used three load cells to measure frost weight. The load cells are calculated with standard weights before experiments. The frost thickness was measured by using videoscope installed 1 foot away from the lower header.

Detailed parametric study of microchannel heat exchanger under dry, wet and frost condition was reported by Jacobi et al. They focused on the performance and performance improvement of microchannel coil heat exchangers. They pointed out that although the microchannel heat exchangers are widely used in many fields, the potential of this geometry has not been fully explored yet.

In spite of the relatively large number of articles found in the literature, there are still several gaps and inconsistencies among the researchers in this field. The main challenge is that the empirical correlations used in literature are valid only for a limited range of geometries and operating conditions.

Table 2.1 gives a summary of the experimental methods used for frost measurement in the most recent literature. The reported uncertainty and experimental conditions are also listed in the table.

Table 2.1 Summary of frost measurement, test methods in the literature

Author and Year	Frost Thickness	Frost Weight	Accuracy and Uncertainty	Measured Range
Kondepudi and O'Neal 1988	Not measured	By measuring absolute humidity difference and check with condensate	Condensate was in 20% of calculated value	Air velocity: 130~200fpm (0.66~1m/s)
				RH: 65%-80%
Lee and Ro et al. 2001	Micrometer attached with thermocouple	By scraping the frost off and weighing in a balance	Frost thickness: ±0.02mm	Time: 0-180 min
				Air temperature: 49~69ºF (9.6~20.3ºC)
			Frost thermal conductivity: ±9.0%	RH: 30%-50%
Watters et al. 2001	By camera resolution	Not measured	Frost thermal conductivity: ±9.0%	Air temperature: 35ºF (1.7ºC)
				RH: 82%
Kim et al. 2002	By digital camera	By weighing the draining system and residual water and by weighing absorbent cotton and cotton tissues	Amount of frost: ±8.4%	Air temperature: 50 ºF (10ºC)
			Weight of residual water: ±11.8%	RH: 70%
			Frost density: ±9.1%	Air velocity: 2m/s(390fpm)
Jacobi and Xia 2005	Frost thickness is viewed from CCD camera	Suspend the specimen under precision scale	Scale accuracy: ± 0.06lb (±3g)	Air temperature: 30~36ºF(-1~2º C)
			Frost accumulation: ±13%	RH: 70~80%
			From humidity difference: ±15%	Air velocity: 197fpm (1m/s)
Padhmanabhan et al. 2008	Frost thickness is recorded by videoscope installed 1ft away from the lower header	The unit is put on three high accuracy load cells	Load cell calibrated in situation with accuracy of ± 0.6 lb (±28.3g)	Air temperature: 35/33 ºF (1.67/0.56 ºC)
				Air flow rate: 1800cfm (0.85m³/s)

CHAPTER III

TEST APPARATUS DESIGN AND INSTRUMENTATION

This chapter gives an overview of the entire test facility constructed for the project. Experimental method and design criteria are detailed discussed in the following sections. The facility includes three parts: the air loop, the refrigerant loop and the frost weighing mechanism. From the practical point of view, the design should not only be reliable in theory, but also feasible to be constructed in the OSU air flow laboratory. In each section below, equipment and instrumentations are described in detail and the reasons for specific selections or assumptions are highlighted.

3.1 AIR LOOP DESIGN

3.1.1 General methodology

A wind tunnel is already present in the OSU air flow lab for heat transfer performance of coils at room temperature. The wind tunnel is about 109 inches long and it has a square cross section measuring 24 inches per side. This wind tunnel was chosen to simulate the winter outdoor environmental conditions to which evaporators are typically exposed to. A thermal guard duct was constructed inside the existing wind tunnel to prevent heat gain from the surrounding air to the test section after the microchannel coil. It is also used as a test   device   for   air   flow   rate   measurement   in   accordance   with   the

24

ASHRAE standard 41.2. At one side downstream the microchannel coil and the flow nozzle, a various speed fan pumps air around the wind tunnel. The fan is capable to provide air speed in the range from 200 to 600 fpm. Figure 3.1 to 3.3 shows schematics of the air wind tunnel and the locations of the fan, humidifier, cooling and re-heating coil, and of the test section.
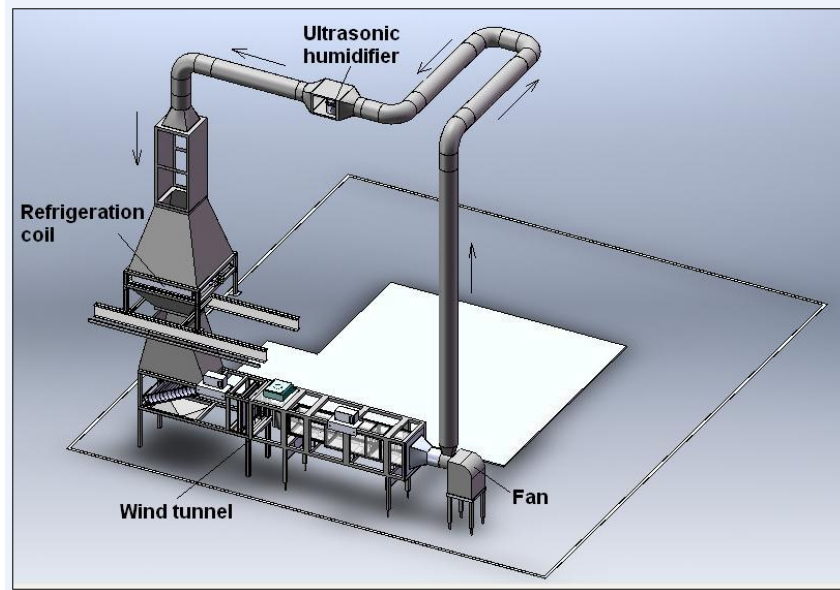
Figure 3.1 Air loop system 3D CAD drawing
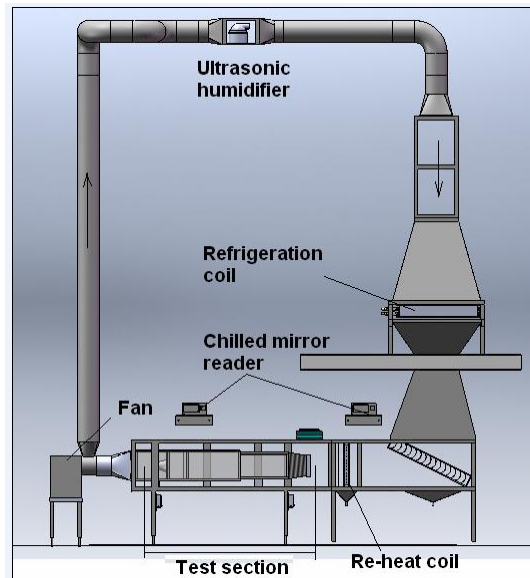
Figure 3.2 Air loop system (front view)
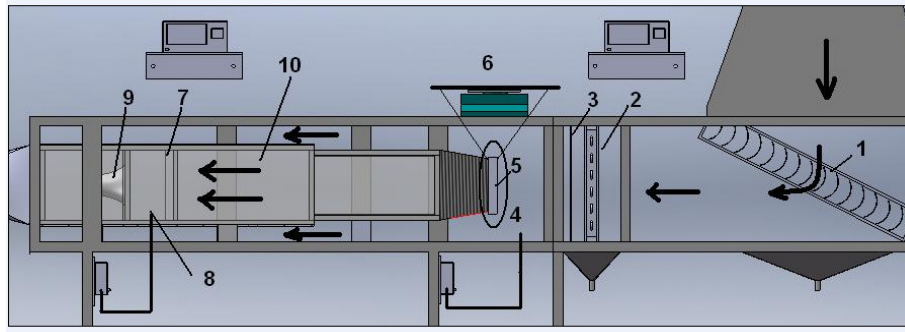
1 Turning vane	2 Re-heat coil
3 Temperature grid inlet	4 Dew point meter inlet
5 Test section location	6 Digital scale
7 Temperature grid outlet	8 Dew point meter outlet
9 Flow nozzle	10 Thermal guarded duct

Figure 3.3   Detailed instrumentation of wind tunnel

As specified by ARI/ASHRAE standard 210 "H2" test for heat pump system, the inlet air temperature must be controlled at 35/33 ºF (dry-/ wet-bulb temperature), with an average velocity of 200 to 400 fpm. In order to meet temperature and humidity requirements, an ultrasonic humidifier, a refrigeration coil and a re-heating coil were installed in the air loop. Figure 3.4 shows the processes I used to reach the desired air-side test condition. Point 4 represents the set point conditions of the air at the inlet of the test section. When air passes through the testing coil, which works as refrigerant evaporator and thus cooling the air, the air temperature is decreased and humidity ratio might be equal to or less than the inlet conditions. In psychrometric chart of figure 3.4 (a), the outlet air reaches point 5 in dry conditions and 5' in wet conditions, depending on the capacity of the test evaporator and of its sensible to latent heat ratio factor. Since the surrounding temperature in the building is at about 77F, even though the duct system is well insulated, certain amount of heat transfer and air infiltration are generally expected.

26
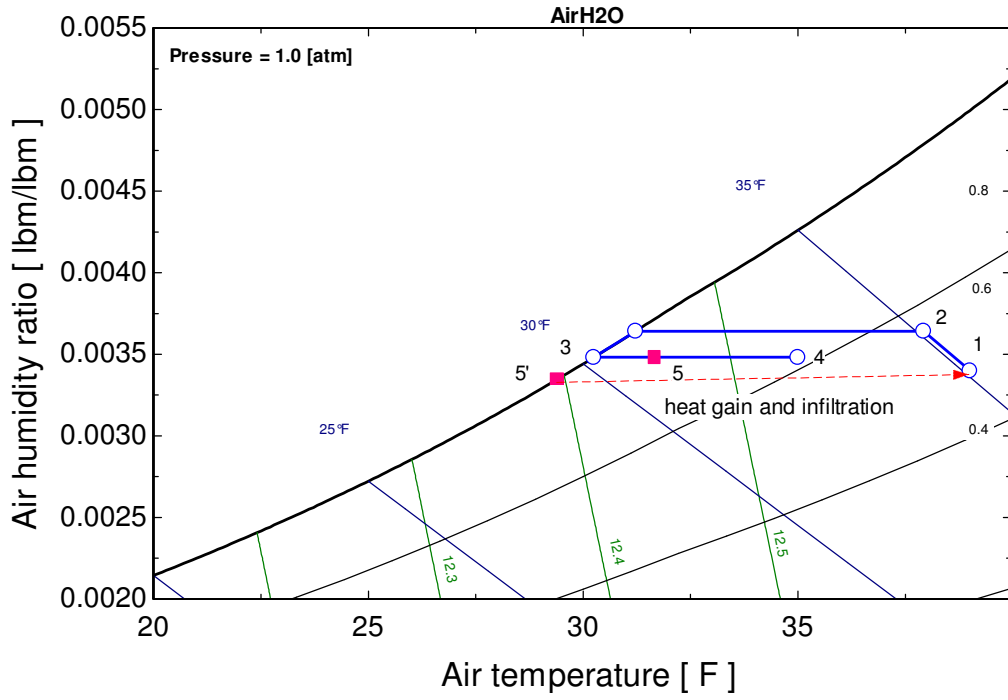
(a)
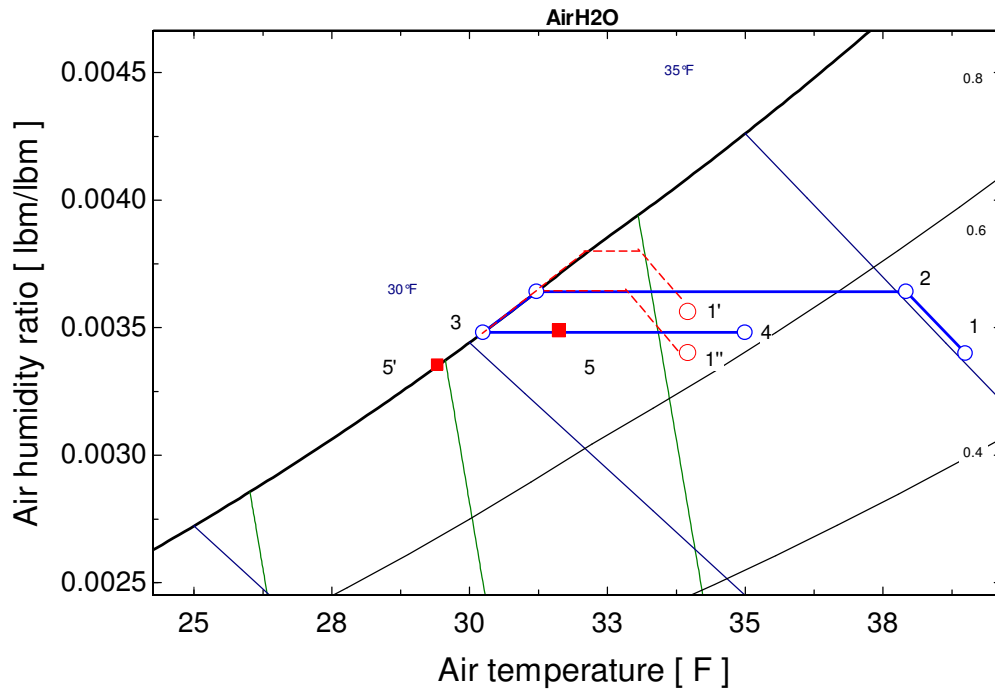
(b)

Figure 3.4 Air side processes to achieve desired psychrometric conditions of 35/33 ºF

dry-/wet-bulb temperature at the inlet of the test section

Thus, the air state point moves from state point 5 (5') to state point 1, in which the dry bulb temperature is higher than the set point (case 1 in figure 3.4 (a)). Point 1 represents the air condition before the humidifier. Between state point 1 and 2, there is a humidification process to guarantee that the absolute humidity ratio would be higher than the set point. An ultrasonic humidifier provides constant vapor flow and makes up for all water condensate in the test section. In case of long periods in which there is no water vapor condensation in the test section, the humidifier is turned off. However, the humidifier is usually completely open and provides excess vapor upstream of the refrigeration coil. Then the air goes into the cooling coil. It is important that the capacity of the cooling coil is designed high enough to cool the air down as saturated until reaching the standard humidity level. That is process 2 to 3 shown in the psychrometric chart. Right before the testing section, a re-heating coil completes and accurately controls the inlet air to the set point of 35/33 ºF dry-/wet-bulb temperature.

In case that the air approaching the refrigeration coil maintains a temperature below the set point, i.e. if state point 1 has lower temperature than the set point 4 as shown in figure 3.4 (b), then there are two cases:

    a)   the humidity ratio is above the set point (state point 1');

    b)   the humidity ratio is close to the set point (state point 1'').

For both cases, the refrigeration coil runs as dehumidification device for the air stream, which is dehumidified and then re-heated to achieve the set point.

This control strategy is preferred because no control is necessary on the humidifier. It would be difficult and expensive to accurately control the relative humidity in the air stream at such low temperatures.

3.1.2 Thermal guard duct design

Thermal guard duct is an important part in the air loop design. This configuration helps reducing heat transfer inside the wind tunnel, right after the test coil and realizes flow measurement. In order to save cost and time on the facility construction, it is desirable to use the existing wind tunnel as a thermal guarded duct by placing the flow measuring apparatus inside. This part was done by Spencer Lifferth, another master student in Mechanical Engineering, Oklahoma State University. The following paragraphs are a brief description of the work he has done.

ASHRAE standard 41.2 presents acceptable setups for measuring the airflow. Two pertinent options include a test duct and a test chamber. Either of these components are to be located downstream of the heat exchanger. Their purpose is to provide an acceptable method to measure airflow through the testing heat exchanger. Both the test duct and the test chamber have strict guidelines about dimensions, airflow, and instrument placement, which are set forth in standard 41.2. Figures 3.5 and 3.6 show the basics of what components are required in each of the test setups.
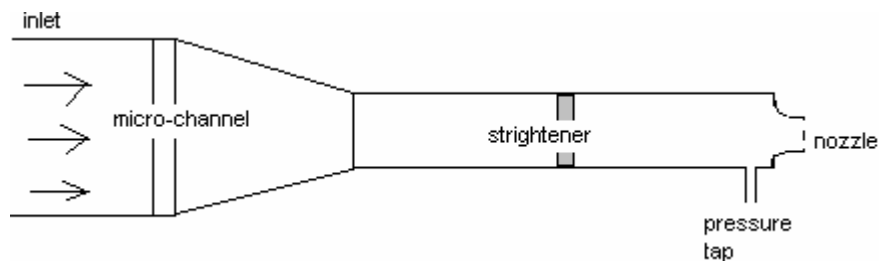
Figure 3.5   Basic components of a test duct
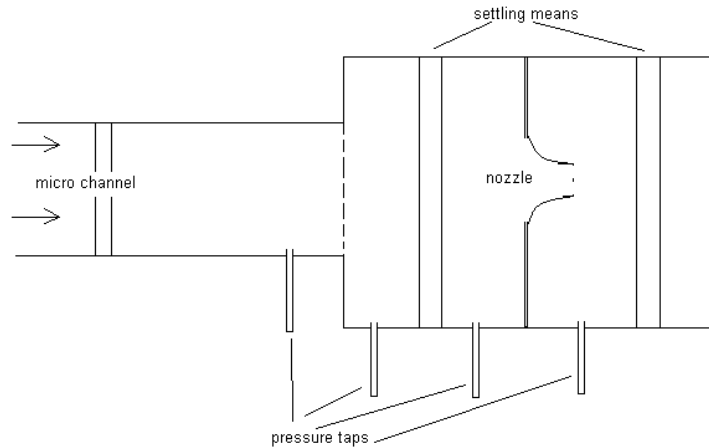
Figure 3.6 Basic components of a test chamber

Compared required geometry of these two test methods with existing wind tunnel, Spencer found only test chamber could be fit in the 109 inches duct and he gave the layout of the test chamber and instrumentation.
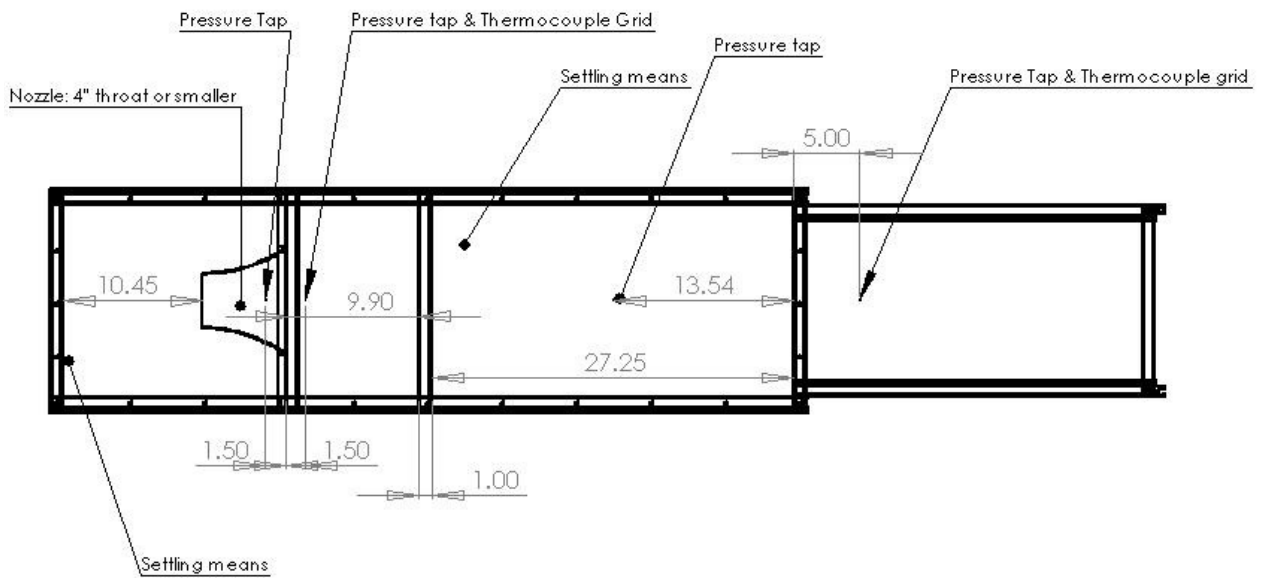
Figure 3.7 Location of instrumentation

The test chamber consists of two sections. The first section is a duct that must have a cross section equal to that of the test unit. The length of this duct must be at least

30

two diameters. The second section is the actual test chamber. The only guideline about the test chamber diameter is that it should be sufficiently large to reduce the velocity pressure head to a negligible value (ASHRAE 1992). According to Spencer's simulation model, 17 inches side dimension of the test chamber gave a reasonable trade off between pressure head and overall length. This also gives enough room for videoscope installation.

In heat transfer analysis, Spencer divided the whole test chamber into ten pieces; each section is 9.25 inches long. Then he calculated uncontrolled heat transfer under different flow and inlet temperature condition. Figure 3.8 gives the graph of uncontrolled heat transfer effect based on the inlet temperature. It is evident from the figure that the thermal guard duct can help prevent heat transfer from significantly altering downstream temperature measurements.
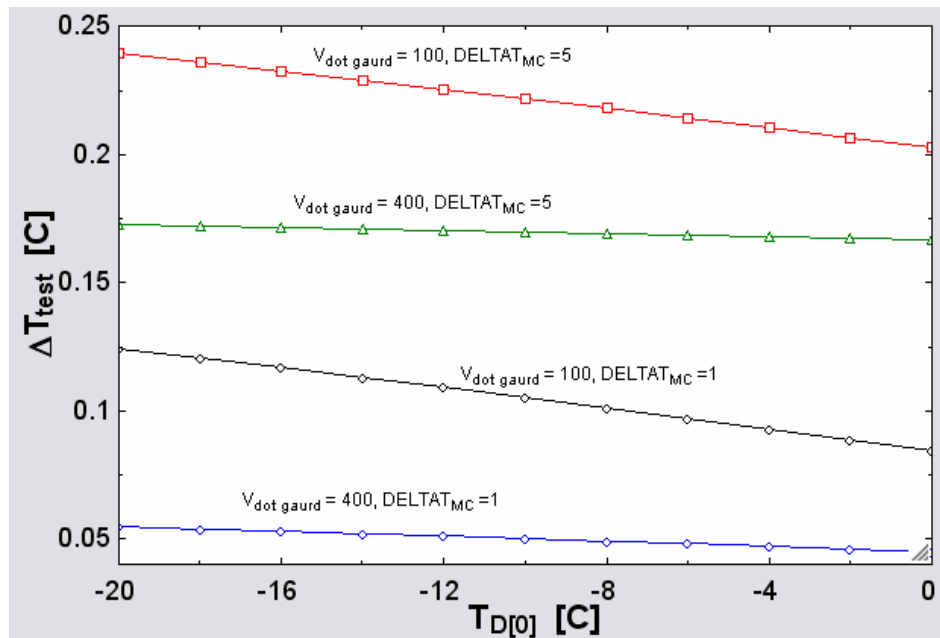
Figure 3.8 Temperature rise of test flow due to uncontrolled heat transfer

3.1.3 Equipment and sensors

3.1.3.1 *Fan*

Figure 3.9 shows the blower used in the air flow wind tunnel. The model is 60 CPS from Loren Cook Company. The dimensions of the fan are 22 ½ (L) x 22 ⅜ (H) x 22 ¼ (W). The fan is a single width, single inlet, backward inclined flat blade, belt driven centrifugal vent set. An electric motor drives the fan. The motor is controlled by a variable frequency drive (VFD), rated 1hp, 60 HZ, 208 volt, 3 phase. The blower is in Class I, which has a maximum speed of 3450 RPM, while Class III has a maximum speed of 4230 RPM. The fan was designed for specific speed, and is not able to withstand higher speed because of the shaft and the support of the bearings.
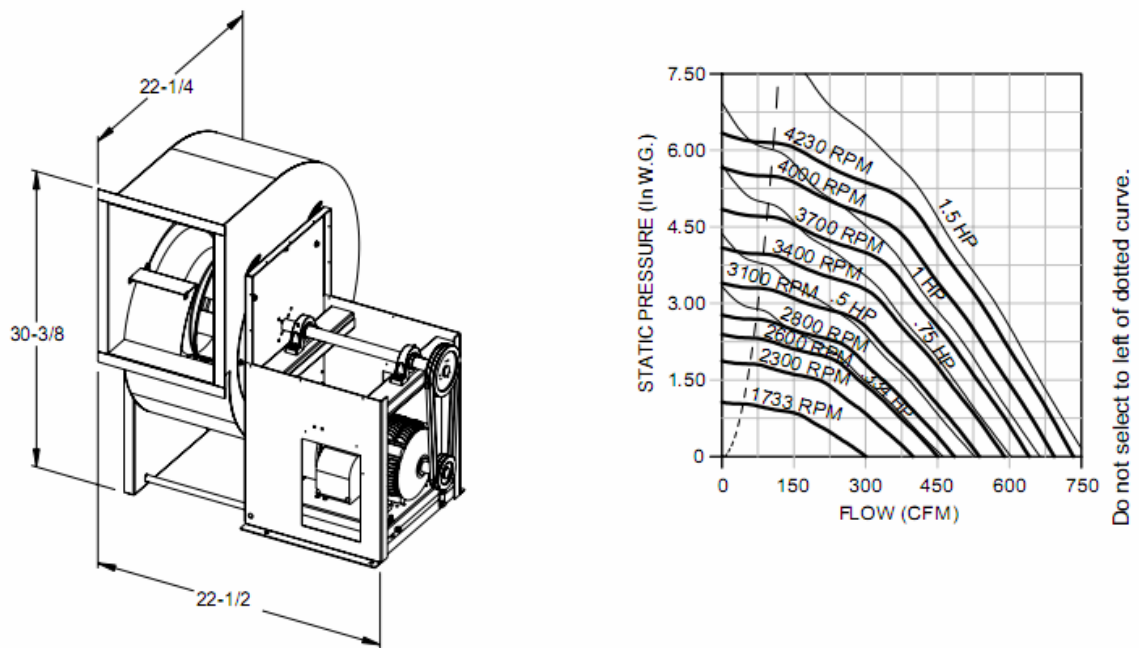
Figure 3.9 Fan configuration and performance curve

According to preliminary calculation of the air loop, the total pressure drop is 0.00125 bar (0.502 in. WG.). Assume a two times extension for the coil, the system

pressure drop at 750 cfm is around 0.0025 bar (1.004 in. WG). From the fan curve shown in figure 3.9, the actual maximum flow rate the fan can supply is 650 cfm. Figure 3.10 indicates the system resistance curve. The operation point is around 500 cfm.
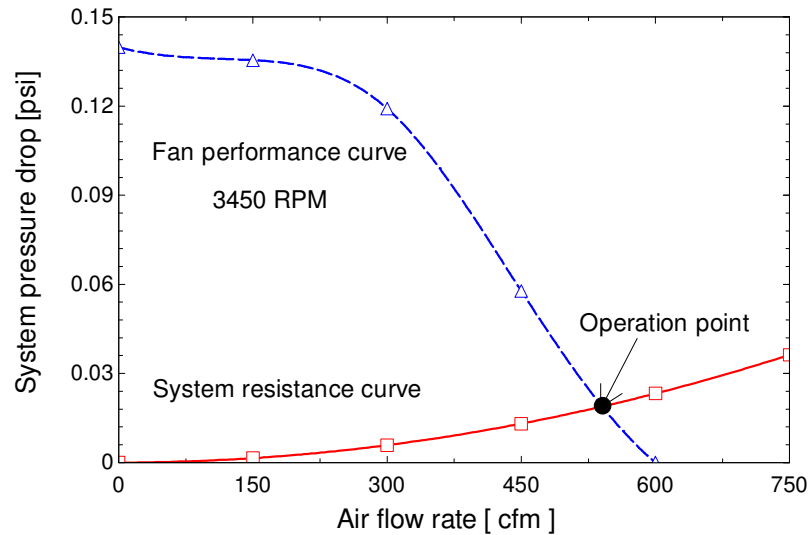
Figure 3.10 System curve

3.1.3.2 *Humidifier*

As mentioned in previous section, an ultrasonic humidifier was installed before the refrigeration coil. Once the air goes through the test heat exchanger under wet and frost condition, temperature decreases, accompanied with a mass transfer. Nevertheless, the humidity ratio before the refrigeration coil is required at a higher level than the test inlet condition. This is because air needs to be saturated and further cooled down in the refrigeration coil till reaching the desired dew point. The readout of chilled mirror, which is placed after the re-heat coil, determines the refrigeration coil capacity by adjusting the refrigerant flow rate coming from the chiller. Due to this measuring and control method, a humidification process is necessary in the whole system.

Figure 3.11 shows the humidification process in psychrometric chart.
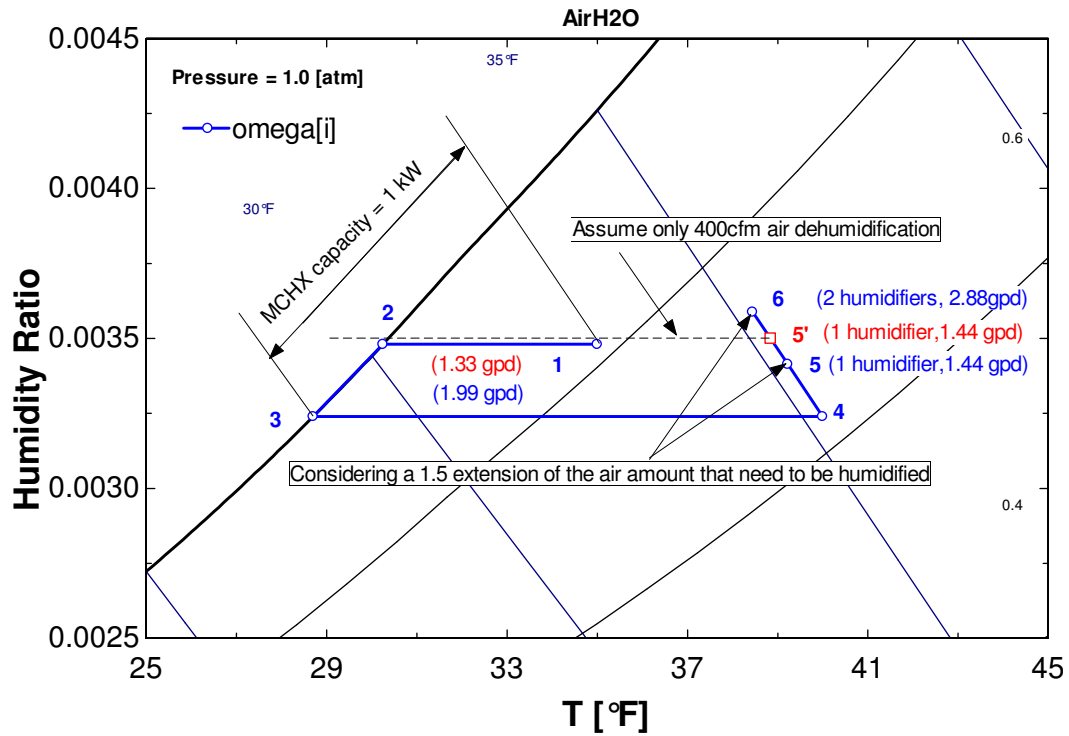
Figure 3.11 Humidification process

The calculation was based on a 1 ft x 1 ft MCHX test specimen. The maximum

capacity of the testing coil was estimated from preliminary experimental results while the

actual capacity was calculated using a first-principle heat exchanger model. The

microchannel coil model is described in the next chapter. Based on preliminary results

from a previous work (Padhmanabhan et al. (2008)), the maximum capacity of testing

heat exchanger was assumed to be 3412 Btu/h (1 kW). With the inlet air condition at

35/33 ℉, the humidity ratio after the test section could be determined. Taking into

account of the heat gain from outside environment, the air temperature increased to point

4 before humidification process. Assume no water/vapor absorption from the

environment, the total humidity difference between point 1 and 4 represents the minimum

amount of water that needs be added to the system. During the frosting experiments of

evaporators in the heat pump systems, the air passed through the test heat exchanger with

34

400 fpm maximum velocity. For a 1 by 1 foot cross section of the wind tunnel the estimated maximum flow rate is 400 cfm. If the air flow rate in the humidification process was constant at 400cfm, this process should supply water mist at least 1.33gpd (Gallon per day). Based on this value, an ultrasonic, 1.2 gallon per 20 hours humidifier was selected for previous purpose. State point 4 to 5' shows the process when include only one humidifier in the system. Due to actual situation, a 1.5 extension was taken into consideration on the dehumidified air flow. Since there was no automatically controlled damper system, the flow rate passes through the test heat exchanger can not be ensured at constant 400cfm. More water is needed with a lower flow rate. In this case, 1.99gpm was the minimum humidifier capacity. Point 5 and 6 shows the humidity level with one and two humidifiers and it demonstrates another humidifier should be set in the system. However, in the preliminary test, only one humidifier was included in the loop. Based on the preliminary test result, it can be decided whether another humidifier is needed or not for the further experiments.

The humidifier is always on at full capacity in the system with the following two reasons:

First, although it seems better if the humidifiers can be controlled automatically on and off, this idea requires at least one humidity sensor before the refrigeration coil, either a relative humidity (RH) sensor or a dew point meter together with thermocouple. Compared to the dew point meter, a RH sensor is much cheaper. However, the accuracy is usually around ±2% to ±5%. This will harm to the system uncertainty.

Second, the latent load of the water added by the humidifier is part of the heat that needs to be removed by the refrigeration coil. If the humidifier works intermittently on

and off, the refrigerant coil must react fast to stabilize the conditions. This requires flow rates of refrigerant from the chiller loop to respond fast to the changes in latent load. In order to minimize these instabilities, the humidifier is run on and at full capacity all time and it supplies constant amount of water droplets in the air flow independently from other components in the loop. The flow rate in the refrigeration coil still needs to be adjusted based on the load of the test section but its control depends on a much slower thermal response. The control method resulted simplified quite a lot and practically the cooling capacity of the refrigeration coil is set once the load conditions are known at the beginning of the tests.

3.1.3.3 *Flow nozzle and pressure tap*

A 4 inch nozzle was installed in the thermal guard duct and its flow coefficient is approximately around 0.9. In Spencer's previous work, he accurately designed the position of the nozzle, as shown in figure 3.4. Four pressure tap measurements are taken around the test section. According to ASHRAE standard, the pressure taps on either side of the nozzle should be connected together as a differential pressure measure, while other two measure the gage pressure. Figure 3.12 gives an idea about the configuration of those the pressure taps. Each tap should be centered on the face of the acrylic. A ¼ inch nipple was glued over each tap with a 0.04 inch hole drilled in the center of it.
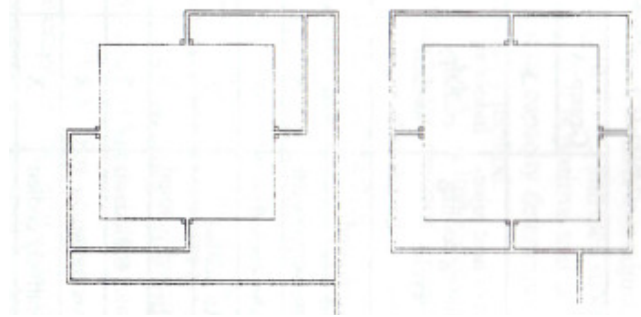
Figure 3.12 Pressure tap configuration

3.1.3.4 *Temperature instrumentation*

3.1.3.4.1 <u>*Chilled mirror and air sampling system*</u>

Two dew point meters were selected from TTI Instruments, Inc. The model number is GE OP-D-1-0-A-A-1-0-0 of General Eastern Optica Series, single stage (111H). An enhanced accuracy sensor with Rhodium mirror and mylar vapor barrier gives a system accuracy at ±0.27 ºF (±0.15 ºC) for dew/frost point. Operating temperature range is 32 ºF to 122 ºF (0 ºC to 50 ºC). The model outputs a 4 to 20 mA and 0 to 5 VDC signal, which are acceptable to Data Acquisition (DAQ) System. An additional sampling air system is needed for dew point measurement. The Sample System Module (SSM), with a model number P40230968 is consisting of a vacuum pump, flow meter and flow control valve. All these are enclosed in moisture resistant housing. The module works for 95-260 VAC, 50/60 HZ. Sampling air flow rate is required around 0.5 cfh.

3.1.3.4.2 <u>*Thermocouples*</u>

T-type wire thermocouples from Omega are used for temperature measurement. The measuring range is -328 to 662 ºF (-200 to 350 ºC) with an accuracy of ±0.36 ºF (0.2 ºC). Considering the possibility of a non-uniform flow, two thermocouple grids are set up at two locations, before and after the testing coil. For the inlet section, sixteen

37

thermocouples are evenly spaced across the cross-section area, four rows of four. For the smaller outlet section, nine thermocouples are distributed as three rows of three. The thermocouples were calibrated before using.

3.1.3.4.3 *RTDs*

In order to perform better on the uncertainty, four more accurate RTDs are used together with the thermocouple grids. Two of them are used for air loop while the other two measure fluid side temperatures. All of them are PR 20 series from Omega with a 2 inch compact design. Probe diameter is 3/16 inch. Measuring temperature range can be changed from -328 to 500 ºF (-200 to 260 ºC). These sensors are allowed to be used in most liquid and air applications. The probes can be used as stand-alone sensors or be configured with a variety of termination options by combing with controllers, indicators or precision thermometers to create complete measurement systems. The accuracy is Class "A" which equals ± (0.15 + 0.002| t |).

3.1.3.5 *Re-heating coil*

In the original wind tunnel, a heating coil has already been set in the duct and can be directly used for this experiment. It is a wavy fin-and-tube heat exchanger, single pass, one row, with FPI =10. The dimension is 20 inch (L) x 20 inch (H) x 4 inch (W). In this experiment, the process fluid is warm water, which is from the water to water heat pump installed in the air flow laboratory.

3.2 REFRIGERATION LOOP DESIGN

3.2.1 General design methodology

In the refrigerant section, there are two different refrigerant loops: one is the chiller loop

connected with the low temperature chiller; the other is test coil loop circulating coolant between plate frame heat exchanger and the test evaporator. The whole system is shown in figure 3.13.
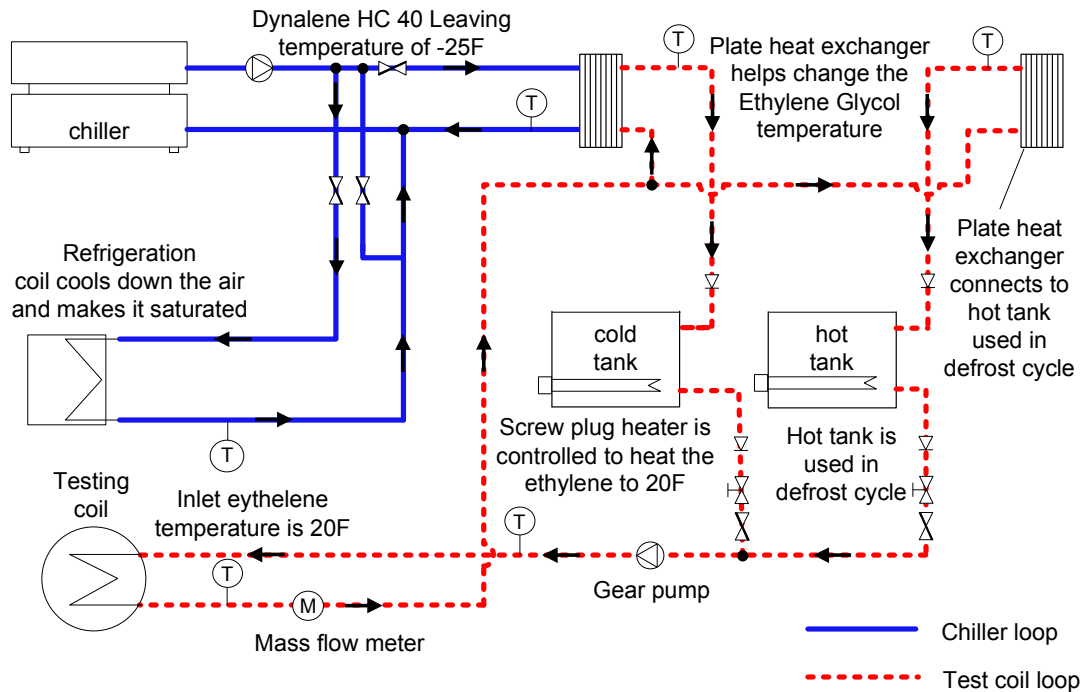
Figure 3.13 Sketch of refrigerant circulation

The low temperature chiller delivers a fluid flow at one temperature, which can be adjusted from -20 to +130F. The flow rate from the chiller adjusts automatically according to the capacity required by the external loads; in my case by the refrigeration coil and by the plate frame heat exchanger altogether.

In the chiller loop, the low temperature refrigerant coming from the chiller goes into two different loops. One loop is consist of the cooling coil to cool down the air temperature; the other one is connected with the plate heat exchanger, having a heat exchange with the ethylene glycol circulated in the test evaporator loop. The chiller loop is a closed system, while the test coil loop is an open one. It would be better to use a close

system in both two loops. However, without any air release apparatus, like the expansion tanks, there is the possibility that air bubble runs with fluid into the system. If these air bubbles rush into the pump, it will stop the whole system. In order to avoid this disadvantage, an open system is preferred, instead. In that case, appropriate refrigerant must be appropriately selected since moisture absorption and toxic problems can not be ignored in an open system.

3.2.2   Refrigerant selection

Because I need to weight the test evaporator coil during frost and wet tests, I must use a single phase heat transfer fluid in the test coil loop. Phase change refrigerants could not be used inside the microchannel evaporator. Single phase heat transfer fluids are also used inside the chiller loop to transport the heat from the refrigeration coil and plate frame heat exchanger to the chiller.

Dynalene HC[1], silicone and ethylene glycol are three types of environmentally friendly low to medium temperature heat transfer fluid. Dynalene HC operates efficiently in a temperature range of -58 ºF (-50 ºC) to 425 ºF (218 ºC). There is no flash point of dynalene HC since it is a non-combustible, aqueous based fluid. Silicon is another liquid phase heat transfer medium with a temperature range of -100 ºF (-73 ºC) to 500 ºF (260 ºC). It takes the advantage of its low viscosity, compared to most other alternative heat transfer fluids used at such low temperature applications. The freezing point of silicon oil can be lower than -100 ºF (-73 ºC). Nevertheless, compared to outstanding low pressure loss, the heat transfer ability is the worst among these three medium due to a small specific heat value. Ethylene glycol is widespread used because of the benefit of lower

---

[1]   http://www.dynalene.com/products/hc.asp

the freezing point when mixed with water. With higher concentration, the freezing point can be decreased to -70 ºF (-55 ºC). But the thermal properties of ethylene solution also vary significantly with different concentration and temperatures.

Table 3.1 gives an overall comparison among these three fluid at 20 ºF (-7 ºC) and -20 ºF (-29 ºC). Since the heat transfer of the refrigeration coil needs to be large enough to bring the air temperature down to the desired point, silicon would not perform well due to the low specific heat. Although dynalene HC and ethylene glycol will introduce a much higher pressure drop, the value can be limited in an acceptable range during piping design. Obviously, the refrigeration coil would give a higher capacity with ethylene glycol solution, which has a better heat transfer ability.

Table 3.1 Thermal properties comparison among three common refrigerants

Thermal properties at 20 ºF (-7 ºC)	Density	Specific heat	Thermal conductivity	Dynamic viscosity
	kg/m³	kJ/kg-K	W/m-K	Pa-s
	lbm/ft³	Btu/lbm-F	Btu/hr-ft-F	Cp
Dynalene HC 40	1330	2.88	0.482	0.0045
	83.03	0.68	0.279	4.5
50% Ethylene Glycol	1090	3.2	0.415	0.012
	68.05	0.76	0.2398	12
Silicone	898.8	1.616	0.1135	0.00295
	56.11	0.386	0.0656	2.95

Thermal properties at -20 ºF (-29 ºC)	Density	Specific heat	Thermal conductivity	Dynamic viscosity
	kg/m³	kJ/kg-K	W/m-K	Pa-s
	lbm/ft³	Btu/lbm-F	Btu/hr-ft-F	Cp
Dynalene HC 40	1340	2.8	0.482	0.0045
	83.65	0.67	0.279	4.5
50% Ethylene Glycol	1110	3.1	0.415	0.012
	69.3	0.74	0.2398	12
Silicone	921.2	1.562	0.1191	0.00473
	57.51	0.373	0.0688	4.73

However, the freezing point of 50% solution is around -22 ºF (-30 ºC), which limited the outlet condition of the low temperature chiller. Considering the low

temperature chiller selection, instead of silicone oil, dynalene HC is more suitable in the chiller loop. When it comes to the test coil loop, using dynalene HC as a refrigerant may cause problems. In this cycle, an open system is selected to avoid any possibility for the air goes into the pump. Dynalene HC is more inclined to absorbing water and this process affects its thermal properties gradually. Under this situation, the replacing procedure is required in a high frequency. From this point of view, eythlene glycol is more suitable in this open system. It is solution and will not absorb much moisture from the environment. Thus, ethylene glycol was used as appropriate refrigerant in the test coil loop, while the chiller runs with dynalene HC 40.

3.2.3 Chiller loop design

The main components in the chiller loop are a low-temperature chiller, a cooling coil and one plate heat exchangers. The plate heat exchanger connects the chiller loop with the test coil loop, helps lower the temperature of ethylene glycol goes into the test specimen.

3.2.3.1 Refrigeration coil

3.2.3.1.1   Position

Refrigeration coil plays an important role in the whole system and the reason has been emphasized several times in the previous sections. Air temperature before the refrigeration coil is lower than 35 ℉ (2 ℃) since it passes through the test section. Assume room temperature at 70 ℉ (21 ℃), the temperature difference between duct and environment achieves 35 ℉ (19 ℃). 1 inch Armflex insulation is used around the air system. It prevents heat transfer between testing duct and environment. Nevertheless, even with insulation thermal properties, it is hard to give an accurate prediction for the

coil capacity due to practical heat transfer. Any incomplete insulation and inappropriate sealing section may bring in certain amount of heat. Thus, a certain extension should be account on the total heat that should be getting rid of. Besides, the cooling capacity of the refrigeration coil is flexible controlled with refrigerant flow rate coming from the chiller. The process pump in the chiller is able to deal with 4 to 5 gpm flow at most, which means the refrigeration coil would run with a maximum flow rate lower than 4 gpm since part of the flow from the chiller goes to the plate heat exchanger. As a result, constrained with high capacity and low flow at the same time, the coil is required in an applicable large size.

By measuring the limited space in the lab, there were two appropriate positions to place the refrigeration coil.
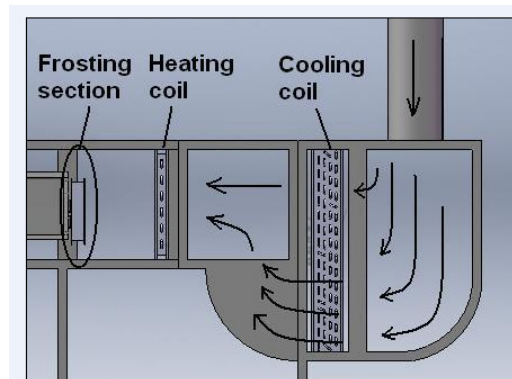
Figure 3.14 Location of refrigeration coil before the wind tunnel

One location is right before the current 2 x 2 ft wind tunnel. The design is shown in Figure 3.14. The largest size of the coil will be 45 x 45 inches with frame. Thus a larger duct needs to be built before the square wind tunnel. Arc shape of the duct will help the air flow goes smoothly through the refrigeration coil and the wind tunnel. A turnning vane at the end of the refrigeration coil duct may help change air flow direction before the cooling process. However, the uniform problem can not be easily solved under

43

wet condition with this design. In wet condition, air temperature is below the dew point, condensate occurs. As a result of gravity effect, condensate will accumulate at the bottom part of the coil. With such an uneven blockage effect, it is hard to maintain a uniform flow through the test heat exchanger.

A substitute way to avoid previous uniform problem is to bring the coil to the intermediate level above the wind tunnel as shown in figure 3.15. The refrigeration coil can be horizontally assembled in an area up to 50 in x 50 in. Expander and reducer are used for connection between the existed air duct and the wind tunnel. Theoretically, the second design would give a better performance. Thus, the dimensions of the coil are designed to be 46 inches x 48 inches with frame and it is placed horizontally at the intermediate level instead of vertically set in front of the heating coil. Condensate is drained out with a U-tube design next to the coil.
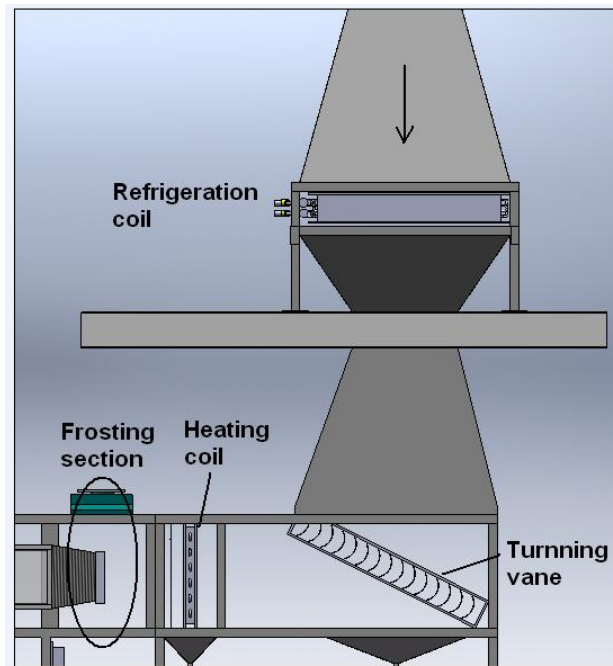
Figure 3.15 Location of refrigeration coil above the wind tunnel

3.2.3.1.2   *Refrigeration coil model*

A plain fin-and-tube coil model was created in Engineering Equation Solver (EES). This refrigeration coil model is developed based on ε – NTU method. Model codes are shown in Appendix A.

The refrigeration coil works under wet condition and the total heat transfer in the coil is determined from effectiveness of the coil (Yan et al., 2005):

$$\dot{Q} = \varepsilon C_{\min} (T_{a,wb,in} - T_{ref,in})$$ [3.1]

Where

ε : the effectiveness

$C_{\min}$: minimum capacitance rate, $C_{\min} = \min(c_{pf,a} m_a, c_{p,ref} m_{ref})$

The energy balance on air side is:

$$\dot{Q} = m_a (h_{a,in} - h_{a,out})$$ [3.2]

The energy balance on refrigerant side is:

$$\dot{Q} = C_{ref} (T_{ref,out} - T_{ref,in})$$ [3.3]

Where

C_{ref} : capacitance rate of the refrigerant

The thermal effectiveness of the heat exchanger depends on the flow pattern and heat exchanger configurations. For single-pass and cross flow, the effectiveness was selected from ESDU (Engineering Sciences Data Unit) [1991] as shown in table 3.2 below:

Table 3.2 Effectiveness for single-pass, cross flow

N_r	Side of C_{min}	Relation
1	Air	$\varepsilon = \dfrac{1}{C_r}[1-e^{-C_r(1-e^{-NTU})}]$
	Tube fluid	$\varepsilon = 1-e^{-(1-e^{-NTUC_r})/C_r}]$
2	Air	$\varepsilon = \dfrac{1}{C_r}[1-e^{-2KC_r}(1+C_rK^2)]$, $K=1-e^{-NTU/2}$
	Tube fluid	$\varepsilon = 1-e^{-2K/C_r}(1+\dfrac{K^2}{C_r})]$, $K=1-e^{-NTUC_r/2}$
3	Air	$\varepsilon = \dfrac{1}{C_r}[1-e^{-3KC_r}(1+C_rK^2(3-K)+\dfrac{3C_r^2K^4}{2})]$, $K=1-e^{-NTU/3}$
	Tube fluid	$\varepsilon = 1-e^{-3K/C_r}(1+\dfrac{K^2(3-K)}{C_r}+\dfrac{3K^4}{2C_r^2})]$, $K=1-e^{-NTUC_r/3}$
4	Air	$\varepsilon = \dfrac{1}{C_r}[1-e^{-4KC_r}(1+C_rK^2(6-4K+K^2)+4C_r^2K^4(2-K)+\dfrac{8C_r^3K^6}{3})]$, $K=1-e^{-NTU/4}$
	Tube fluid	$\varepsilon = 1-e^{-4K/C_r}[1+\dfrac{K^2(6-4K+K^2)}{C_r}+\dfrac{3K^4(2-K)}{C_r^2}+\dfrac{8K^6}{3C_r^3}]$, $K=1-e^{-NTUC_r/4}$

Where

$$NTU = UA/C_{min} \qquad\qquad [3.4]$$

$$c_{pf,a} = \frac{h_{a,in}-h_{a,out}}{T_{wb,in}-T_{wb,out}}$$

The total heat transfer coefficient depends on the inside and outside heat transfer coefficients and conduction in the tubes:

$$\frac{1}{UA} = \frac{1}{h_{in}A_{in}} + \frac{\ln\dfrac{D_{out}}{D_{in}}}{2\pi k_{tube}L_{tube}} + \frac{1}{h_{out}A\eta_{surf}} \qquad\qquad [3.5]$$

Where

A : total surface area

A_{in} : inside surface area

D_{in} : inner diameter of the tube

D_{out} : outer diameter of the tube

h_{in} : refrigerant side heat transfer coefficient

h_{out} : air side heat transfer coefficient

k_{tube} : tube material conductivity

L_{tube} : tube length

η_{surf} : surface efficiency

The refrigerant side heat transfer coefficient is based on Nusselt number:

$$Nu = \frac{h_{in}D_{in}}{k_{ref}}$$
[3.6]

Where

k_{ref} : refrigerant conductivity

The air side heat transfer coefficient in cross flow configuration depends on the j-factor:

$$j = \frac{h_{out}}{G_c c_a} \Pr^{2/3}$$
[3.7]

Where

G_c : mass flux evaluated at the minimum flow area

Correlations for Nusselt number and j-factor were selected from McQuiston (1989), Shah and London, and Wang et al. (1999). These correlations are detailed discussed in chapter 4.

From the coil model, it is easy to see that both *Nu* and *j* are propotional to the Reynolds number, which means higher *Re* results in higher heat transfer coefficients.

However, in the refrigeration coil design, both capacity and pressure drop should be taken into account at the same time. Higher *Re* represents a faster fluid movement and this increased velocity leads to a larger pressure drop across the heat exchanger:

$$\Delta P_{major} = \rho f \frac{L \dot{v}^2}{2g_c D}$$ [3.8]

$$\Delta P_{\min or} = \rho k \frac{\dot{v}^2}{2g_c}$$ [3.9]

Where:

ΔP_{major} : pressure drop in the pipes

$\Delta P_{\min or}$: pressure drop in the fittings

D : pipe diameter

f : friction factor from Moody chart

g_c : constant (1 in SI unit)

k : minor loss coefficient

v : flow velocity

ρ : flow density

One solution to this high capacity with low pressure drop is to separate one single loop to several parallel passes. The total pressure drop is then decreased to one pass with lower *Re*. The heat transfer capacity can be maintained by adding multiple rows.

Based on this approach, a one-row, one-circuit, a two-row, two-circuit and a four-row, four-circuit fin-and-tube models were modeled in EES. Figures 3.16 and 3.17 show the comparison results on heat transfer capacity and the total pressure drop.
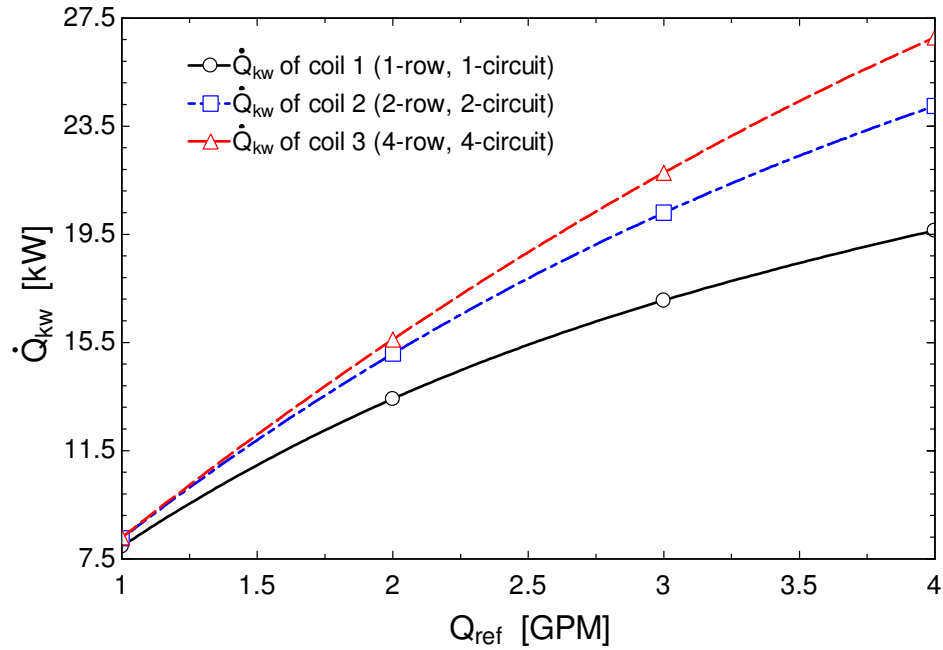
Figure 3.16 Capacity of the refrigeration coil under different flow rate
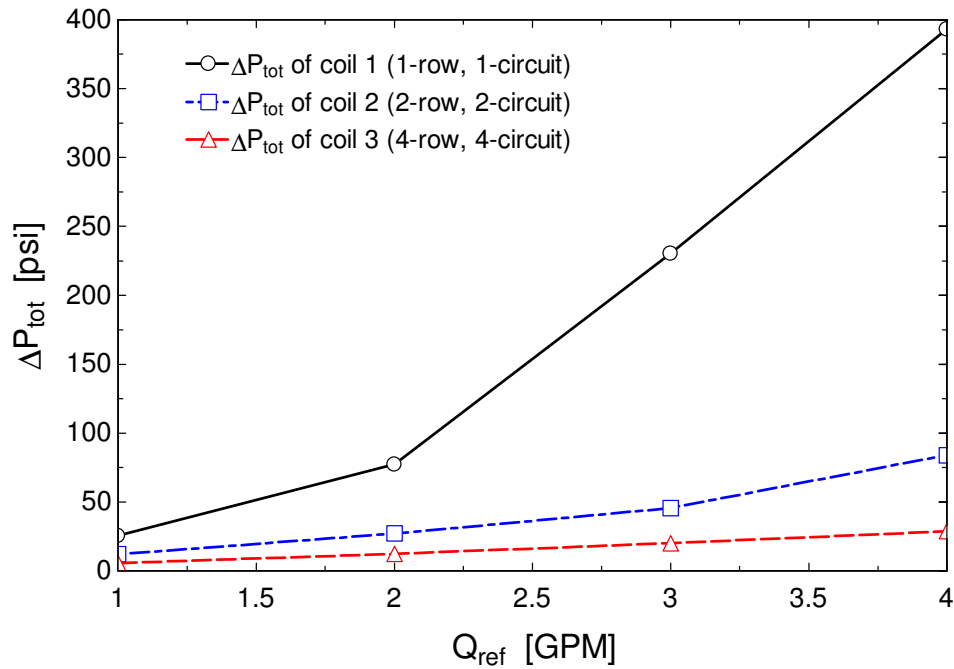
Figure 3.17 Total pressure drop of the refrigeration coil under different flow rate

The model results showed clearly that the fin-and-tube heat exchanger with a multiple circuits and several rows could achieve higher capacity with a much lower pressure drop. The capacity of the multiple rows coil gives a larger capacity range with different flow rates. Another big advantage of the multiple circuits configuration is shown in the pressure effect. Compared to the one-row, one-circuit model, the low *Re* in four-circuit coil gives an acceptable range of the total pressure drop.

Assume in the system, there is a 20 ºF temperature rise and the air flow rate is 2000cfm, the heat gain before the cooling coil is estimated to be 14kW, which means the refrigeration coil should remove at least 14kW heat from the air. From figure 3.16, either coil 2 or coil 3 can meet the required capacity. But when it comes to the pressure drop across the coil, the pressure drop in coil 3 is only half of coil 2. Considering the process pump in the chiller, the capacity and flow rate requirements, a 46 in x 48 in, four-row, four-circuit fin-and-tube heat exchanger was designed for cooling and dehumidification process.

3.2.3.1.3   Configuration of the fin-and-tube heat exchanger

After I designed the refrigeration coil and created the technical CAD drawings, the required fin-and-tube coil was custom-made by Johnson Control Inc. The coil has constant row pitch (P_r) at 0.866 inch and a tube pitch (P_t) of 1 inch. Details and dimensions are shown in figures 3.18 to 3.20 below.
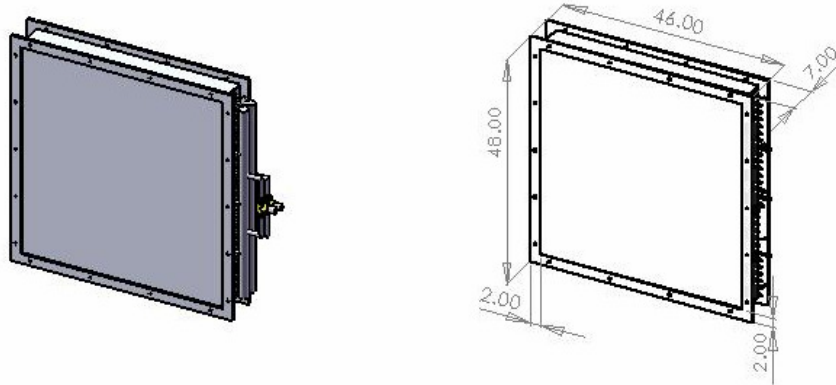
Figure 3.18 Overall dimension of the refrigeration coil installed in the wind tunnel of

the air flow lab (unit: inch)
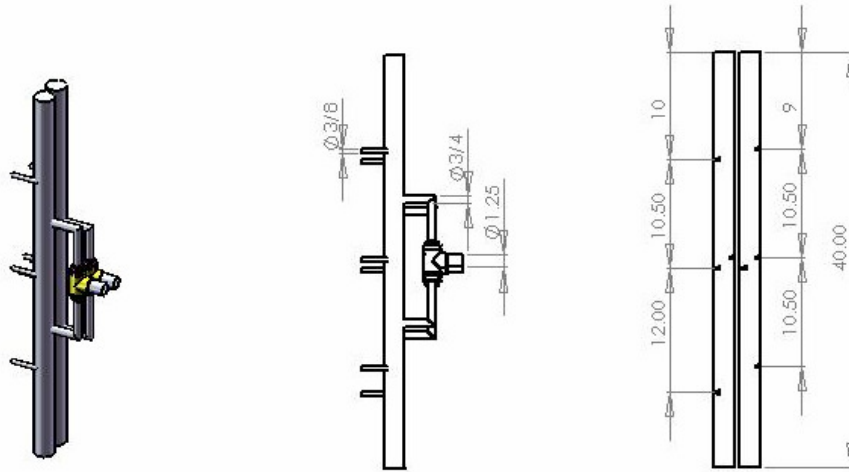
Figure 3.19 Configuration of the inlet and outlet header (unit: inch)
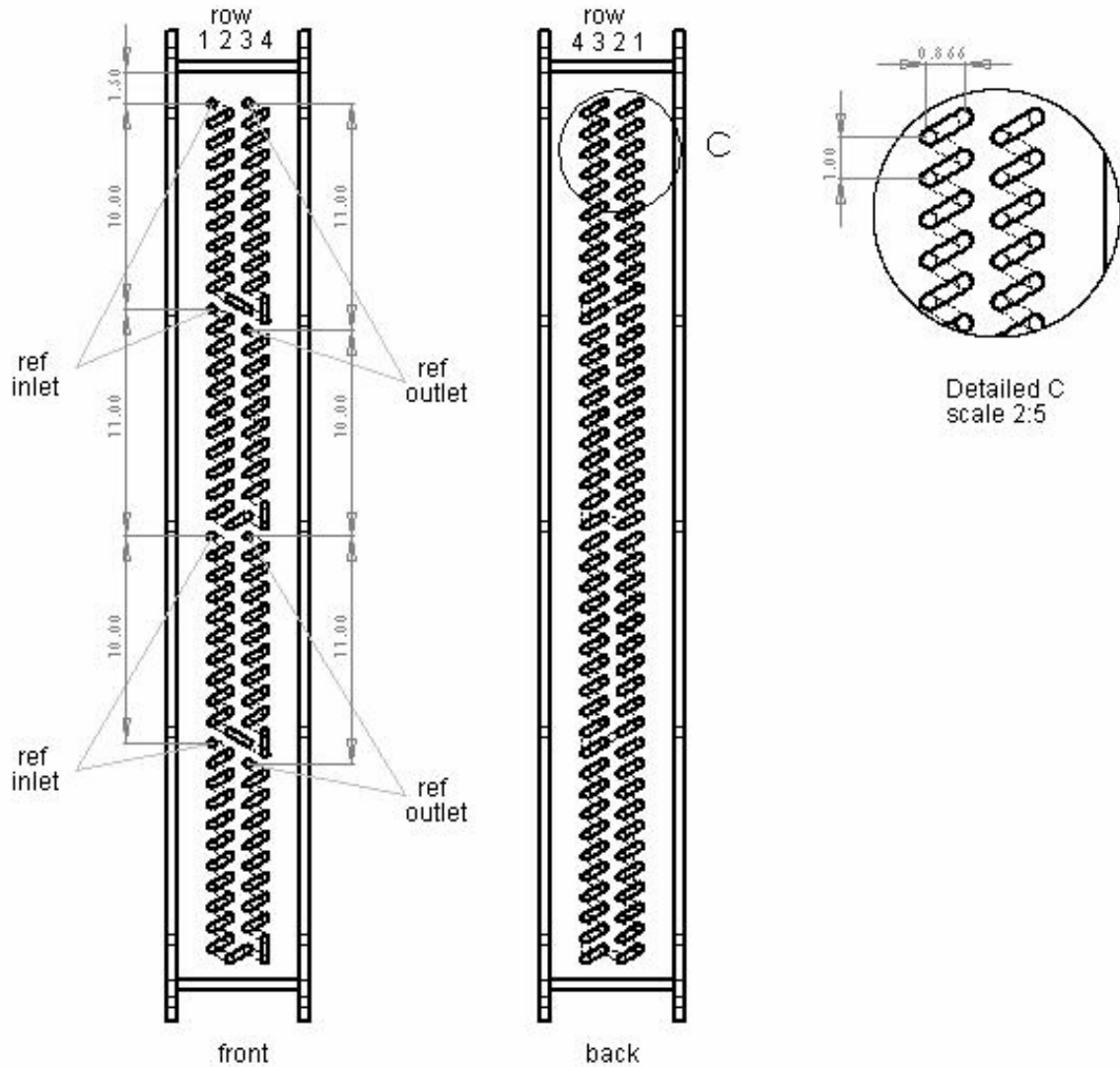
Figure 3.20 Circuits configuration of the refrigeration coil (unit: inch)

3.2.3.2 Hydronic system analysis and pump selection

The hydronic system analysis focuses on selecting the pipe sizes and determining the pressure drops in the loop that delivers low temperature water based heat transfer fluid (dynalene HC40) to the refrigeration coil in the wind tunnel and to plate frame heat exchanger of a compact temperature control unit. Since the process pump in the chiller is able to handle only 20 psi max of pressure head, pipe sizes needed to be carefully

selected. The two branches, the pipeline connected to the refrigeration coil and the pipeline connected to plate frame heat exchanger are installed in parallel to the main pipeline from the chiller. They should achieve similar pressure balance during normal operation of the hydronic system. Manually adjusted flow metering valves helps in achieving this pressure balance, but, appropriate size of the hydronic pipeline is required so that:

a) the total pressure drop in the entire chiller pipeline (including main pipeline and sub-branches), is always below 20 psi; this is chosen as the maximum value the process pump in the chiller is able to deal with;

b) there is a reasonable pressure balance between the two parallel branches of the hydronic system for a broad range of flow rates.

Equations [3.8] and [3.9] give the basic idea of pressure drop calculation. In addition to the major and minor pressure drop in the straight pipelines, the head loss across and refrigeration coil and plate heat exchanger needs to be added to the relevant loop sections.

The pressure drop in the refrigeration coil can be calculated by using the coil model created in previous section. The circuits and header were treated as several 180 return bends and tees.

According to manufacturer's data, the plate heat exchanger chosen for this project has a head loss of 3.55 psi at the cold side with a flow rate around 8 GPM. Assuming that there is a linear function between flow rate and the total head loss, the pressure drop of the plate heat exchanger at different flow rate is estimated in the range from 0.3 to 2.22 psi.

Figure 3.21 shows the pressure drop between two parallel branches with various pipe diameters.
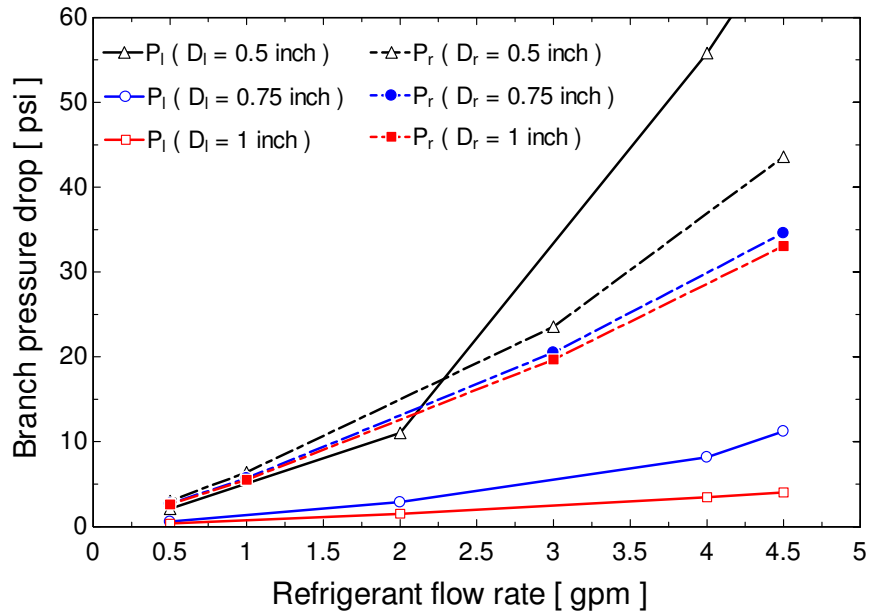
Figure 3.21 Pressure drop with different flow rates and pipe sizes

P_l represents the loop connected to the plate heat exchanger, P_r represents the loop

connected with the refrigeration coil

Results indicated the fin-and-tube heat exchanger was the predominant component and it contributed to the pressure drop of the refrigeration coil loop. 80% pressure losses happened in the 4-row, 4-circuit fin-and-tube coil. Compared to the coil branch, plate heat exchanger loop had a flatter trend. Thus, in order to reach a balance, the pipe size in the coil loop must be larger than the heat exchanger loop. In figure 3.21, the pipe sizes varies from 0.5 in to 1 in. When the flow rate is between 0 to 2 gpm, 0.5 in diameter for the plate heat exchanger loop has a good match with the 1 in diameter in the refrigeration coil loop. Total pressure drop is close to 10 psi. The chiller has a constant flow pump and the flow rate is around 4 to 5 gpm, using 0.5 in diameter pipe in the plate heat exchanger branch together with 1 inch pipe for refrigeration coil loop may cause

some problems. With the current chiller, the two branches might not operate at the same flow rate all the time. The flow rate in the coil loop can not exceed 3 gpm and it would be adjusted from 0 to 3 gpm, depending on the heat transfer in the air wind tunnel. In that case, heat exchanger loop would operate between 2 to 5 gpm. Based on this requirement, a 0.75 inch pipe was selected for the heat exchanger loop and 1 inch pipe for the coil loop. In order to achieve pressure balance, the coil loop should run between 0 to 2 gpm, while the heat exchangers loop in 3 to 5 gpm. The maximum pressure drop is estimated to be around 10 psi. A bypass line was added so that only the amount required for the plate frame heat exchanger is actually delivered to it via the flow metering valve. In practical cooling load conditions, the additional fluid flow rate that is required neither by the refrigeration coil nor by the plate frame heat exchanger is by-passed back to the chiller through a by-pass line and a third flow metering valve.

3.2.3.3 Equipment in the chiller loop

3.2.3.3.1 <u>Low temperature chiller</u>

A portable water cooled chiller was installed in the hydronic system. The model number is CPCW-12LT/TC2-1-9x2 from Cooling Technology and it is provided with integrated temperature controller. The unit is able to deliver 2.0 tons at -25 ºF (-32 ºC) LFT (leaving fluid temperature) and 60 ~ 65 ºF (16 ~ 18 ºC) entering condenser water temperature. Dynalene HC 40, a water based heat transfer fluid engineered to deliver the desirable low-end temperature performance of synthetic organic and silicone-based fluids[1], is used as the process fluid in the hydronic loop, while refrigerant R404A is used in the compressor side of the chiller. Because of the space available in the laboratory, the chiller was installed on one side of the lab while the refrigeration coil and the temperature

control unit were located on the opposite side. Thus, using a secondary coolent reduced the amount of refrigerant in the cooling system and it allows adopting low working pressure components in the hydronic system. The size of the whole chiller unit is about 90 in (L) x 32 in (W) x 72 in (H). It includes a 12 HP bitzer semi-hermetic compressor from Bitzer with single cylinder unloader and cooling fan, a 316L stainless steel brazed plate evaporator and cleanable tube-in-tube condenser with regulating valve. An end section recirculation pump is able to supply up to 6 to 8 gpm within a pressure rise between 25 to 30 psi. The process pump can deal with 4 to 5 gpm with a pressure increase of around 20 psi. A 25 gallon vented stainless steel chilled fluid tank with sight glass and valve drain is used for storage of Dynalene HC 40. Two 9 kW electronic heater with incoloy elements heat the Dynalene HC 40 above freezing point of the water before it goes into tank. The whole unit uses PID control. The temperature control unit can accurately maintain the process fluid temperature at ±1.5 ºF. All the components are mounted on common skid and enclosed by cabinet.

3.2.3.3.2   *Plate frame heat exchanger*

One plate heat exchanger is assembled in the chiller loop. It facilitates heat exchange between the refrigerant in the chiller loop with the test evaporator cycle. Another plate heat exchanger is used in the heating loop. Detailed information will be discussed in the following section.

3.2.4   Test evaporator loop design

The test evaporator loop is designed to control the fluid temperature and flow rate entering the microchannel test specimen. These variables could be varied from the chiller set point and from the fluid temperature required in the refrigeration coil of the wind

tunnel. The fluid temperature and flow rate in the test evaporator could be adjusted between 0 and 20°F and from 1 to 10 gpm, respectively. Because frost is weighted as it accumulates in the microchannel heat exchanger, single phase low temperature fluid must be used inside the microchannel tubes of the test specimen. Any phase change refrigerant would introduce an additional uncertainty in the measurements of the weight because the mass of liquid refrigerant in the heat exchanger volume is not known and it varies as the heat exchanger frosts up. The additional layers of frost on the heat transfer surfaces impair the heat transfer rate of the evaporator. The amount of liquid fraction in the evaporator tubes increases as the frost accumulates on the surfaces. Eventually, if the experiment is carried over for sufficient time, liquid refrigerant might flooded the evaporator under testing. Because the density of the liquid refrigerant is much higher than the one of vapor refrigerant, any increase of liquid refrigerant fraction in the tubes of the test specimen used as evaporator would be interpreted as frost weight increase during the measurements. Thus if a phase-change fluid is used inside the test specimen under frosting conditions, it would not be possible to differentiate the contribution of the weight due to the frost accumulated on the surfaces and due to the liquid refrigerant fraction increase. For this reason, a mixture of water and ethylene glycol 50/50 was selected for the test coil loop. This mixture provided a trade off between thermodynamic properties, chemical corrosion, and environmental concerns in case of catastrophic failure of the test specimen. The test loop consists of two plate heat exchangers, a gear pump, a cold reservoir for the frosting period and a hot reservoir for the defrost operation. In frost cycle, the plate heat exchanger connected with the chiller loop facilitates heat transfer between ethylene glycol (refrigerant in the test loop) and dynalene HC40 (refrigerant in

the chiller loop). The other heat exchanger can be connected to some heating source for warming up refrigerant temperature in the defrost cycle. The gear pump circulates ethylene glycol inside the test coil loop at various flow rates. Two immersion heaters are plug into the reservoirs separately. Those heaters help maintain inlet refrigerant temperature to the test coil around 20 ℉. A flow meter is used to measure flow rate running in the test loop. Manually operated ball valves are used to switch between frost and defrost cycle. At the end of the frosting cycle, hot reservoir and the hot source heat exchanger are connected in line with the test section and the cold reservoir is cut out of the hydraulic system.

3.2.4.1 Compact temperature control unit design

The test coil loop is actually a separate cycle with specific equipment and sensors. It would benefit to construct a compact unit with all necessary parts in and make it portable. In that case this unit can either be used in current experiments or in other future projects later. For the specific purpose, a portable temperature control unit was designed and fitted on a two-shelf cart. The cart is on four wheels and it was installed in the air flow lab. The temperature control unit is used for cooling/heating refrigerant with temperature and flow rate measurement. Labview program is compatible to the controller so that the entire unit can be automatically controlled in remote. Figure 3.22 gives the configuration of the temperature control unit built in the air flow lab.
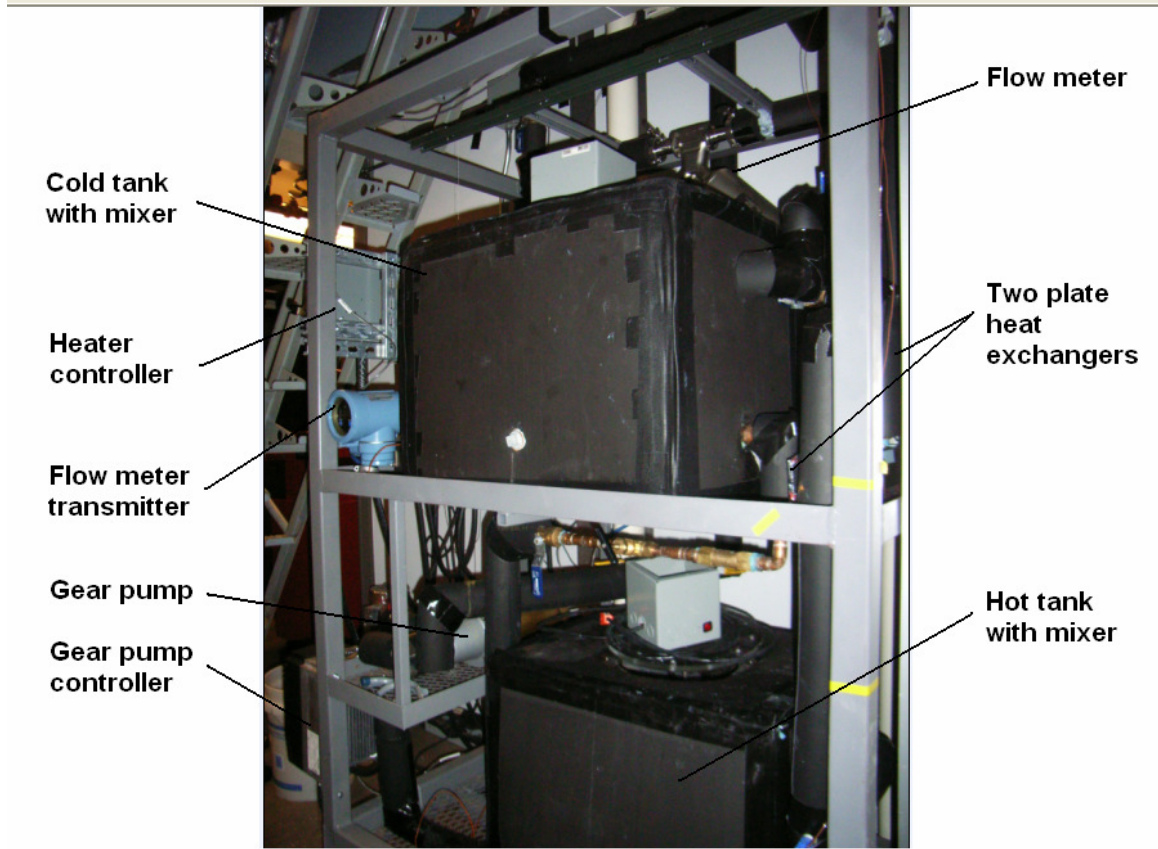
Figure 3.22 Compact temperature control unit in the two-shelf portable cart

The two-shelf cart has dimensions of 50 in (L) x 70 in (H) x 30 in (D). Cold and hot tanks are set separately on the top and bottom shelves. A ball valve is used to switch between the two tanks. A metering valve and another ball valve are connected at the fluid outlet of each tank. The metering valve is used to adjust system fluid flow rate and ball valve helps turn the loop on or off. To avoid cavitation, the gear pump, together with the motor and controller, are located at the bottom part of the cart. A relief valve is set inline before the gear pump to prevent air going into. Four disconnect valves enable the cart disconnecting with the system and make the cart portable. The equipment and sensors selected in the cart are all able to handle various conditions to help increase the flexibility of the portable unit and realize a widely used purpose.

3.2.4.2 Equipment and sensors

3.2.4.2.1 Gear pump

Circulating pump plays an important role in the whole loop. It supplies a pressure rise to overcome head loss in the refrigerant system. An appropriate pump needed to be selected based on system performance. Two types of pumps were taken into consideration. One is traditional centrifugal pump, and the other one is gear pump.

Centrifugal pump is the most common pump used in pumping system. A rotating impeller increases the fluid pressure. It is suitable for the case with large discharge and small head loss. Figure 3.22 gives the performance curve of a centrifugal pump selected for this project. With a variable frequency driver (VFD), the pump can work under different RPM. According to affinity laws, for a fixed impeller diameter, the head and flow rate are related to the new and old speeds, which are:

$$Q_{pn} = Q_{po} \frac{RPM_n}{RPM_o} \qquad\qquad [3.10]$$

$$H_{pn} = H_{po} (\frac{RPM_n}{RPM_o})^2 \qquad\qquad [3.11]$$

With these correlations, the performance curves of a centrifugal pump under different speeds can be estimated as shown in figure 3.23. Based on fluid system requirements on flow rate and pressure loss, a VBA model was created to determine the exact speed range.
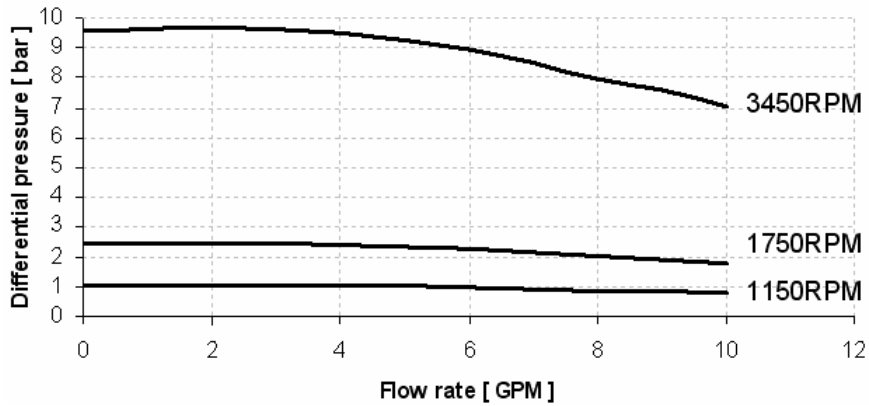
Figure 3.23 Performance curve of centrifugal pump with varied speed

Compared to centrifugal pump, the gear pump is more often used for hydraulic fluid power applications. Due to the rigid design of the gears and the housing, gear pump is able to deal with high pressure when the fluid has a large viscosity. Figure 3.24 shows the performance curve of a gear pump.
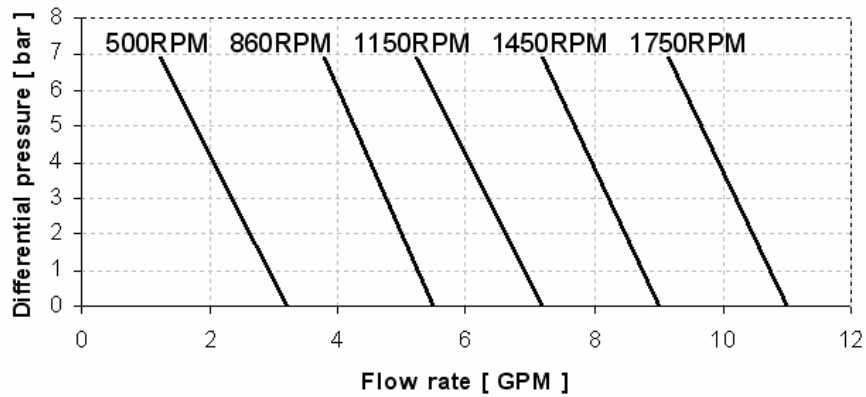
Figure 3.24 Performance curve of gear pump

It is indicated that within a small flow rate difference, the pressure rise changes in a wide range and almost linear to the flow rate. In this case, regardless of the pressure drop of the system, the flow rate supplied to the test specimen depends only on the RPM set to the pump. The large pressure differential also allows fluid in both low and high viscosity. This character is important for the temperature control unit, as it was designed

61

to be portable and flexible used in most projects. Different refrigerant, diverse coil configuration all may give quite different system curve. It benefits a lot when the pressure change is significant within a narrow flow rate range.

Low required net positive suction head (NPSHR) is another advantage of gear pump. Each system has its own available net positive suction head (NPSHA):

$$NPSHA = \frac{P_s g_c}{\rho g} + \frac{\overline{V_s}^2}{2g} - \frac{\rho_v g_c}{\rho g}$$
[3.12]

Where

$P_s g_c \big/ \rho g$ = static head at the pump inlet, ft or m, absolute

$\overline{V_s}^2 \big/ \rho g$ = velocity head at the pump inlet, ft or m

$P_v g_c \big/ \rho g$ = static vapor pressure head of the liquid at the pumping temperature, ft or m, absolute

To avoid noise and "cavitation" problems, NPSHA must be higher than NPSHR. With a lower NPSHR, the pumping fluid does not need to keep a high velocity all the time. The pump position is also more flexible.

"Cavitation" has a significant effect to the centrifugal pump. The vapor bubbles formed in "cavitation" process move towards the oncoming impeller and collapse the leading edge of the impeller vane. Pump vibration occurs as a result and damages pump bearing, wear rings and seals. Most of the centrifugal pumps are unable to withstand sustained "cavitation". Gear pump will also face this problem. However, the damage to gear pumps is not so severe as in centrifugal pump.

Besides, the preselected gear pump has a magnetic drive. This specific driver looses connection to the shaft once the current is too high. In that case, overload problem is efficiently avoided.

The comparison between centrifugal pump and gear pump is listed in table 3.3.

Table 3.3   Comparison for pump selection

Comparison	Centrifugal pump	Gear pump
Maximum speed (RPM)	3500	1750
Head @ maximum RPM (bar)	7.0 ~ 9.6	0 ~ 6.9
NPSHR (ft)	9.22 ~ 10.7	5.767
"Cavitation" damage	Severe	Average
Driver	Mechanical shaft	A magnetic engaged shaft which prevents overload

A gear pump was preferred after comparing to the centrifugal pump. According to preliminary calculation, maximum pressure drop is around 3 bar at 8 GPM. The gear pump chosen from Micropump has a model number GN-G35.JVS.E with the maximum flow rate at 11.4 GPM. The differential pressure head is up to 6.9 bar. The pump is close coupled to a 1hp, 56C motor with base. An inverter drive (VSISP21-1B), rated 1hp, 230 volt, 3 phase input and output is used to accept digital signal, in a way that the pump could be controlled automatically by using Labview program.

3.2.4.2.2   *Plate frame heat exchanger*

As mentioned in previous section, two plate heat exchangers helped exchanging heat between the test evaporator loop and chiller/heating loop. Since the test coil is simulated as an outdoor evaporator, the temperature of ethylene glycol increases, depending on the coil cooling capacity. In order to maintain a constant refrigerant inlet temperature, at 20 ºF, ethylene glycol has a certain amount of heat transfer with the dynalene HC 40 from the low temperature chiller.

Based on temperature requirements, the heat transfer rate was estimated to bring ethylene temperature slightly below 20 ℉. The overcooled part would be retrieved from the electrical heater set in the cold tank. If this overcooling takes the refrigerant temperature far from the required condition (20 ℉), more heat is needed from the heater in the following process. This is obviously a waste of energy and really unnecessary.

The capacity of the plate heat exchanger was determined from testing coil model. The plate heat exchanger was required to make up for the heat absorption in the testing coil and the heat gain from environment. Since both fin-and-tube and microchannel heat exchangers needed to be tested, the specimen with a highest capacity was chosen in my capacity calculation. From open literature review, it is easy to know that microchannel coil performances better than fin-and-tube heat exchanger. The capacity of dry coil is higher than the specimens in wet and frost condition. In this plate heat exchanger selection section, a dry microchannel specimen was used in calculation.

A 1 ft x 1 ft MCHX model was created. Detailed configuration data and model method is shown in Chapter 4. Figure 3.19 gives the cooling capacity of the MCHX with different flow rate. Based on the maximum flow rate of the gear pump and the head loss from pumping design, 10 GPM was the largest flow rate that could be circulated in the system. Fluid outlet temperature from the MCHX was also obtained from the coil model and showed in figure 3.25.
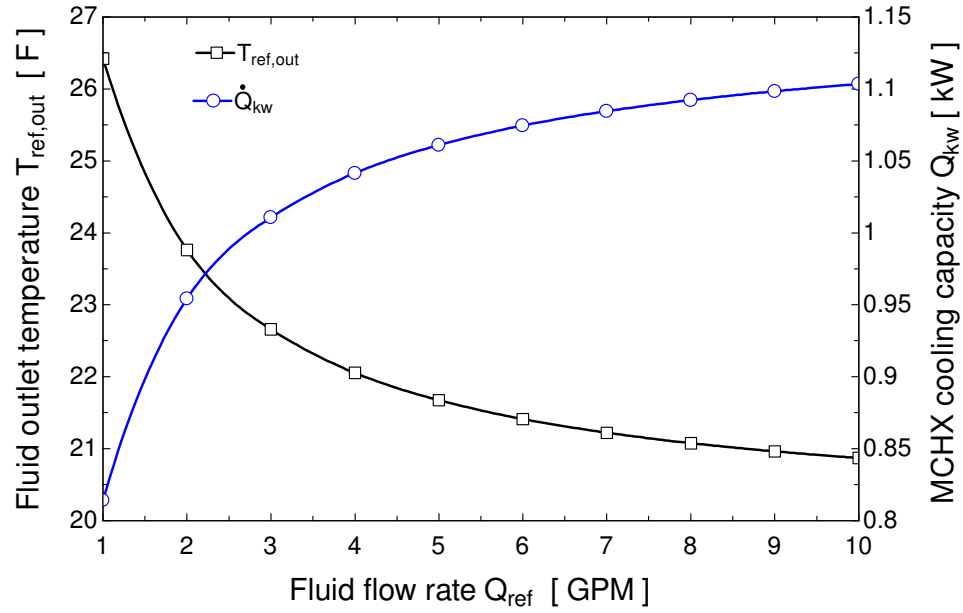
Figure 3.25 Cooling capacity and refrigerant outlet temperature in the MCHX specimen
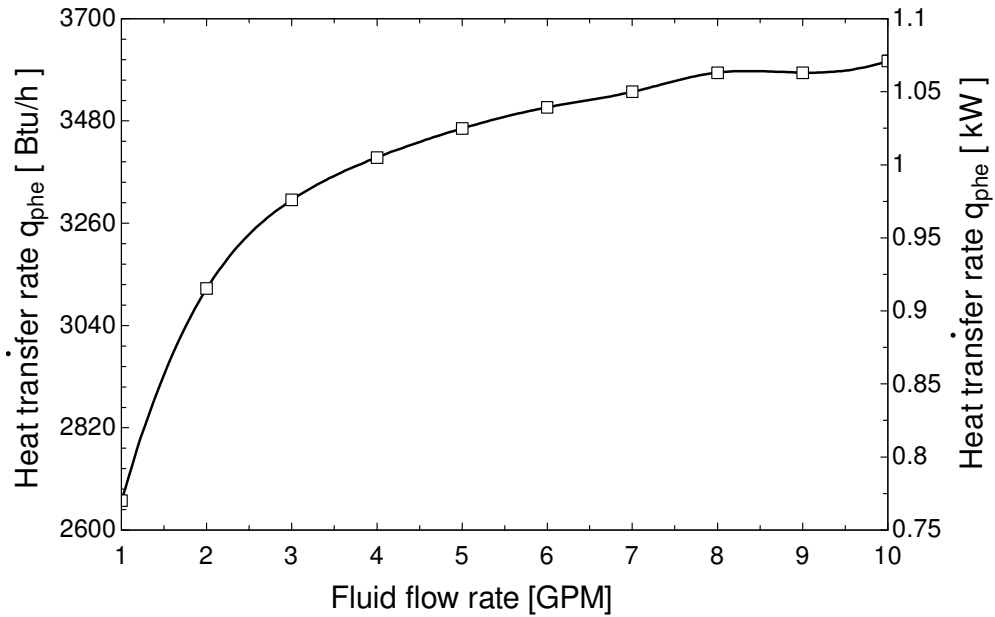
Figure 3.26 Heat transfer with different flow rates

Figure 3.26 gives the minimum heat transfer requirement for different flow rate. 3609 Btu/h (1.068 kW) is the maximum heat transfer needed during frosting process. This result did not consider any heat gain during the loop and assume the outlet

temperature from the heat exchanger ($T_{ea,out}$) was equal to the inlet temperature before

the testing coil ($T_{ref,in}$) as shown in figure 3.27.

MCHX TEST LOOP
(with Eythelene Glycol)
Q_dot: 1 ~ 10 GPM
T_ea_out

CHILLER LOOP
(with Dynalene HC 40)
Q_dot: 3 ~ 5 GPM
T_hc_in = -25F

Cold
Tank

Plate Heat
Exchanger

Q_dot_phe
=cm(T_hc_out-T_hc_in)

Q_dot_heater
=cm(T_ref_in-T_ea_out)

Low
Temperature
Chiller

Q_dot_phe
=cm(T_ea_in-T_ea_out)

T_ea_in

T_ref_in = 20F   T_ref_out

T_hc_out

Testing Coil
Q_dot_mc=2600~3600 Btu/h
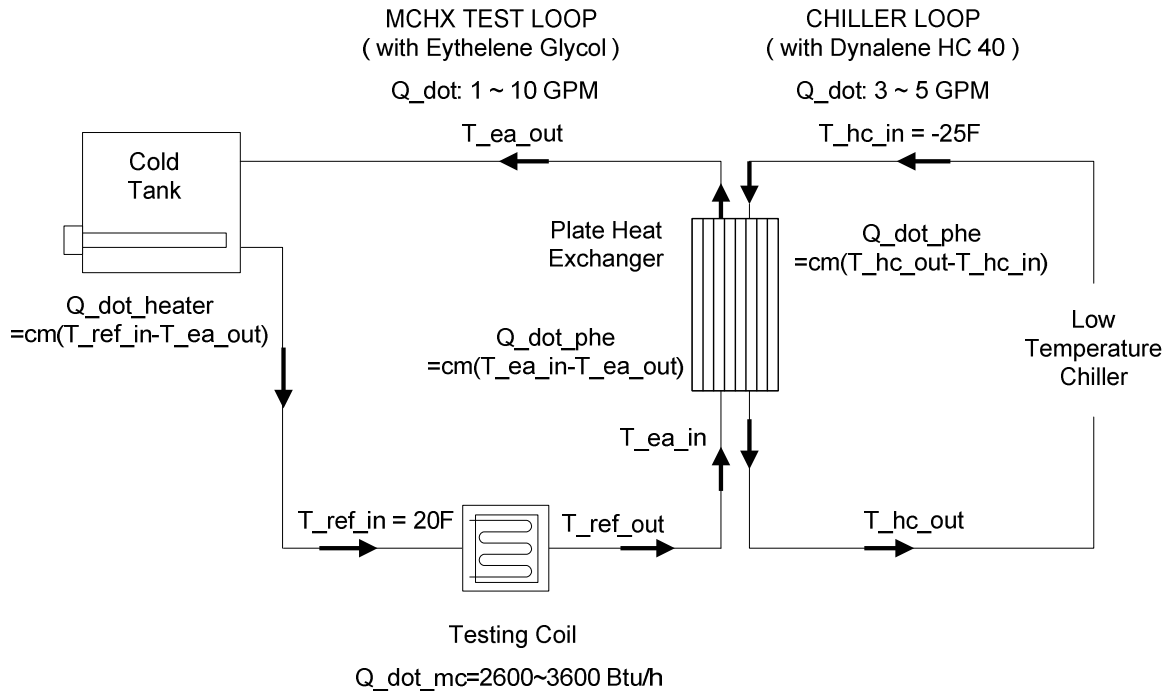
Figure 3.27   Schematic of typical operating conditions of the chiller loop and testing

loop during the frosting experiments

However, in real situation:

a) It is inevitable to prevent heat gain in the loop, which is about 100 ft long.
Temperature might increase a little bit after the test coil, which gives a larger total
temperature difference.

b) To avoid temperature fluctuation, an electrical heater is plugged into the tank.
The heater is automatically controlled based on actual temperature of the fluid goes into
the tank and the testing coil. This heater can be controlled automatically to heat ethylene
glycol up to 20 ºF.

Considering actual heat gain and temperature fluctuation problem, the required maximum heat transfer of the heat exchanger is preferred to be higher than 3609 Btu/h (1.068 kW). The heater helps maintain required temperature to the test evaporator. The plate heat exchanger recommended from Alfa Laval can supply 5305 Btu/h (1.554 kW) at 8 GPM. In this project, during frost cycle, another plate heat exchanger connected to the hot tank was used. Defrost process could be controlled using the 2 kW immerse heater in the hot tank. Considering the flexibility of the cart, a hot side heat exchanger is preselected.

The plate heat exchanger from Alfa Laval has a model number CB14-28H. The hot side heat exchanger was selected in the same model.

3.2.4.2.3 _Electrical heaters in the temperature control unit tanks_

Two screw-type electrical heaters are immersed separately in the hot and cold tanks. These heaters are necessary for maintaining refrigerant temperature and minimizing temperature fluctuations.

Two 2kW immersion heaters were provided from Chromalox. Model number is MTO-220A, single phase, 208V, 20W/in². These immersion heaters are designed for light weight oil application with 2 inches steel screw plug. It takes the advantage that once changing the refrigerant to flammable and light weight fluid, the heater is still suitable.

A SCR Power pack controller is used together with the immersion heater. Model number is MMAX1-3-01-1-1-1. It is a proportional control with 75 Amp at 122 ºF (50 ºC) ambient temperature, 50/60 Hz. The linear voltage is between 120 ~ 480 Vac. The model is electronically protected with temperature warning and shutdown system. Digital

signals 4 ~ 20 mA, 1 ~ 5 Vdc, 0 ~ 5 Vdc and 0 ~ 10 Vdc are accepted so that it is able to communicate with Labview program.

3.2.4.2.4 *Flow meter in the temperature control unit*

A coriolis mass flow meter was selected from Micro Motion, Inc. The sensor is ELITE series with a model number CMF100M339NQBAEZZZ. The transmitter connected is 2700R12ABAEZZZ. CMF100 is able to measure flow rate rangeing from 1.0 lbm/min to 160 lbm/min. Although the maximum flow rate in the system would be around 10 GPM, that is 78lbm/min, a lower flow rate range model is not preferred due to the large pressure drop. Based on silicone properties, figure 3.28 shows the pressure drop comparison among three sensors with different flow rate. CMF100 gives an obviously extremely low pressure with wider measuring range. That is the main reason of choosing CMF100 as flow rate instrumentation. In ethylene glycol system, although the fluid is more viscous and leads to a higher pressure drop, CMF 100 still performs better than the other two types. Pressure drop in ethylene glycol system was estimated from current data sheet.
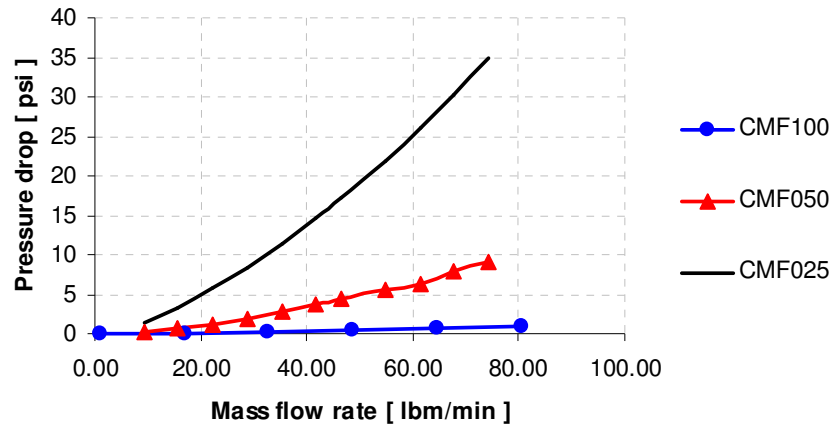
Figure 3.28 Pressure drop comparison among three flow meter models

Table 3.4 shows the pressure drop and accuracy change under different flow rates based on silicon oil. The accuracy is pretty high when the mass flow rate is lower than 30

lbm/min. After that, the accuracy reaches a constant value, ±0.10%. The flow rate effect

on accuracy was considered in the uncertainty analysis.

Table 3.4 Accuracy with different flow rates

Flow Rate [lbm/min]	Mass Flow Accuracy [±% of Rate]	Pressure Drop [psi]	Velocity [ft/sec]
160.00	0.10	2.949	10.87
144.10	0.10	2.455	9.79
128.20	0.10	1.998	8.71
112.30	0.10	1.581	7.63
96.40	0.10	1.205	6.55
80.50	0.10	0.875	5.47
64.60	0.10	0.595	4.39
48.70	0.10	0.368	3.31
32.80	0.10	0.198	2.23
16.90	0.15	0.077	1.15
1.00	2.50	0.002	0.07

3.2.4.2.5   Tanks for Ethylene Glycol-Water mixture in the temperature control unit

Two rectangular, 24 inch (L) x 17 inch (W) x 19 inch (H) steel tanks were designed for

storage the mixture of ethylene-glycol and water in the test loop. Eight openings with

different sizes were designed for specific uses. The mixer in the tank helps keeping fluid

temperature uniform. Detailed information is shown in figure 3.29. The tanks are used to

set the ethylene-glycol and water mixture temperature and they reduce the temperature

fluctuations of the mixture delivered to the test evaporator. The temperature of the

mixture in the tanks is set by the control and it is kept constant during the frosting

experiments. These two tanks are used in different cycles. One tank is used for the cold

mixture used during the frosting period while the other is used for the hot mixture

delivered to the test evaporator during the defrost cycles.
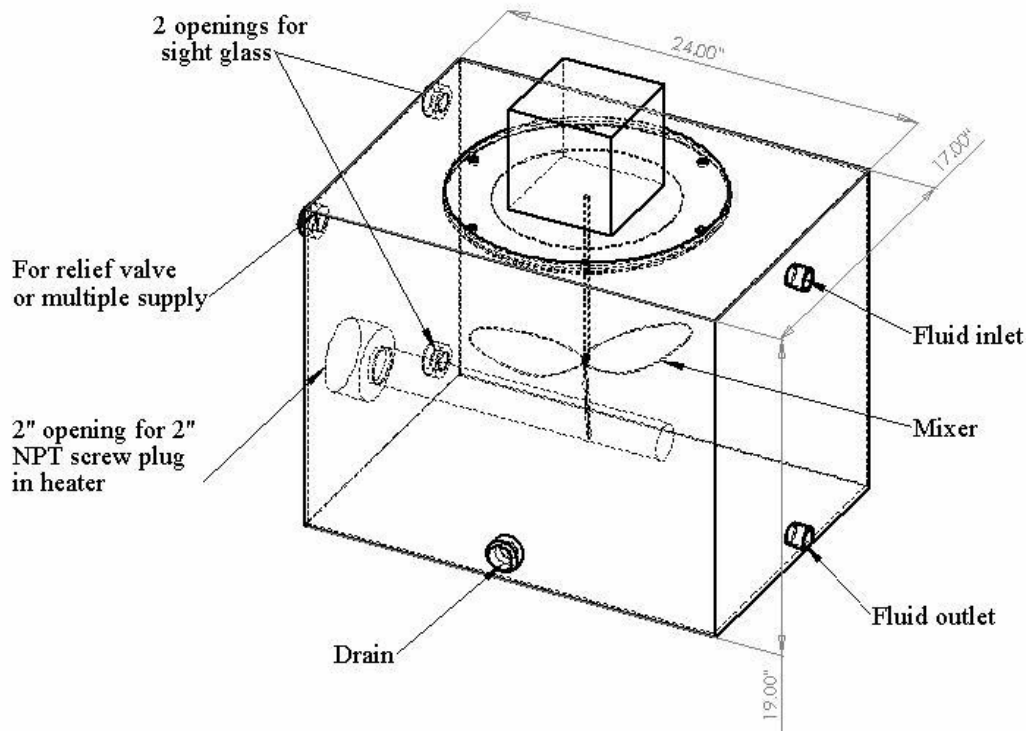
Figure 3.29 Tank configuration

3.2.4.3 Ethylene Glycol and Water Mixture loop analysis

Based on selected equipment, total pressure drop in the MCHX test loop was estimated

with different pipe diameters. Similar to the chiller loop, equation [3.8], [3.9] were used

for major and minor pressure drop. The head loss across the plate heat exchanger and

flow meter were obtained from manufactures' specification data sheet. For testing

evaporator part, a fin-and-tube coil model was used for pressure drop calculation. The

coil model was similar to the model discussed in the refrigeration coil section. The head

loss across the coil was simplified treated as a sum of major and minor pressure drop.

Figure 3.30 gives the pressure drop with various flow rates by using different pipe

diameters. The maximum pressure drop must be lower than 6.9 bar, which is the largest

pressure rise from the gear pump. 0.5 inch pipe gives a much higher head loss once the

flow rate exceeded 4 gpm. Although changing diameter from 0.75 inch to 1 inch would give an obviously decrease in pressure drop, the mass flow rate is almost doubled. Since pipes are suspended under the ceiling, the total weight should not be much high due to the load-bearing capacity of the anchor and all threads. Including both pressure and weight concern, the pipe diameter was determined to be 0.75 inch, which gave a 3 bar pressure loss at 8 GPM.
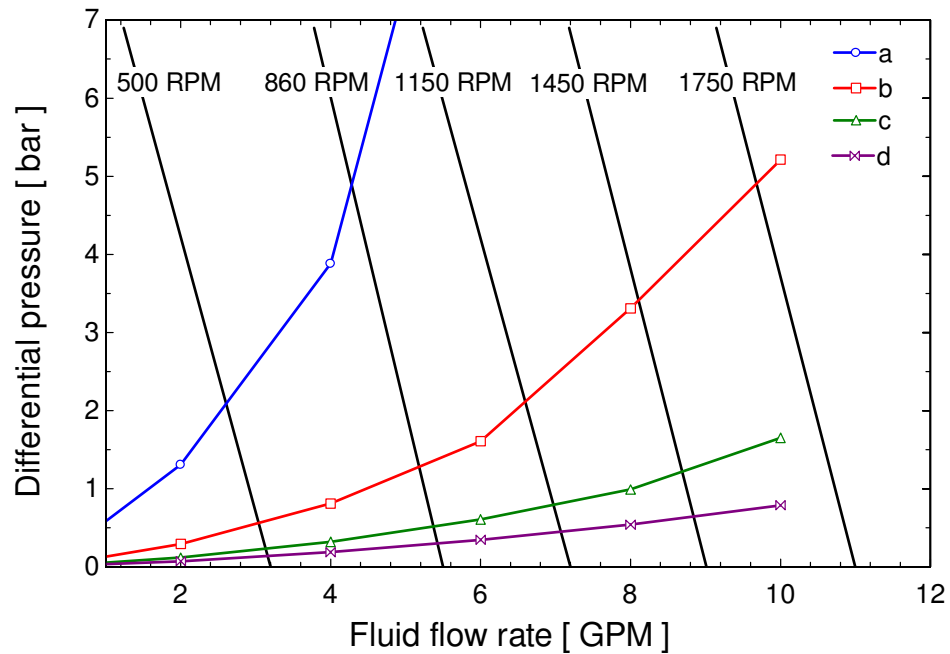
Figure 3.30 Pressure drop with various flow rates at different diameters

a: D=0.5 inch; b: D=0.75 inch; c: D=1 inch; d: D=1.25 inch

3.3 FROST WEIGHING SYSTEM DESIGN

3.3.1 General methodology

To investigate frost accumulation, both frost thickness and weight need to be measured in the experiment. The frost thickness is measured from the pictures taken by the videoscope. From literature review, several different methods were used by previous researchers. When considering condensate measurements it was found that this method is

not enough accurate and feasible for my measurements. The frost I would like to measure is during the entire frosting period and especially at the beginning of the frost period, when frost nucleation takes place. Weighting the condensate would provide the amount of frost accumulated on the heat exchanger. The onset of frost nucleation and the frost growth rate could not be measured with this method. Thus, I decide to opt for measuring the frost weight by weighting the entire heat exchanger as it frosts up during the experiments. By taking the difference in weight, the mass of frost on the heat exchanger surface is directly measured.

For measuring equipment, both load cell and scale were taken into consideration. Setting the test coil on top of one or two load cells which are installed in the wind tunnel helps provide a stable measure environment. The specimen would not effect by the incoming flow. However, the accuracy of the load cell is usually around ±0.02% of the full scale. The weight of test coil with water is estimated around 18kg, which means the capacity of the load cell should no less than 20kg. In that case, the error will achieve 2g. In order to minimize the error, we also thought another possible measuring method by using one or two 1kg load cell installed with the test coil on top. Figure 3.31 shows the sketch of the apparatus.

The test coil is suspended under a scale. The thread connected to the test coil is able to adjust to make sure the weight on the load cell is zero before frost accumulated. Thus, the value got from the load cell is the weight of the frost. Although this combination of scale and load cell does prevent the movement of test coil with the flow, and to some extent, decrease the accuracy, both accuracy of the scale and load cell are

taken into consideration and made the uncertainty complicated. In practical, manual adjustment of the thread to maintain load cell "zero" is not that convenient and feasible.
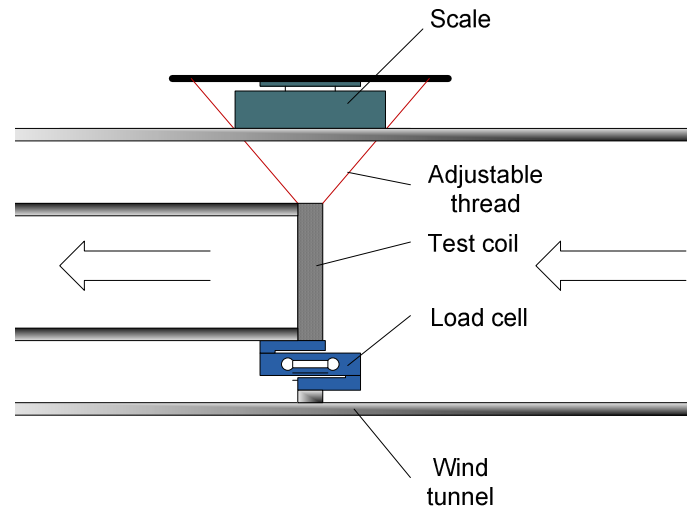
Figure 3.31 Weighing system by using load cell

Figure 3.32 gives an overview of the scale weighing method improved based on previous work. Considering accuracy and stability, it is the method that we finally adopted for this frost experiment. A precision scale is used instead of the load cell. The scale is set on top of the wind tunnel with two 32'' long beams aside. The testing coil is suspended with four wires going through the two long beams. Suspending angles are adjusted until the testing coil reaches a stable equilibrium, and the angle is around 45º to 60º. With four wires and appropriate suspending angles, the testing coil was restricted to vertical movement only. A plastic flexible thin film is applied between the specimen and the thermal guard duct. It is true that linear bearing can achieve vertical movement easier, but the high friction will affect the accuracy of the total weight. Video probe is plug in and set close to the specimen for frost formation observation. Thickness can be estimated from the pictures captured by the videoprobe system.

(a)

(b)

Precision
scale

Test
specimen

6

5

4

Two beams attached
to the scale

Four metal wires tied
to the test plate
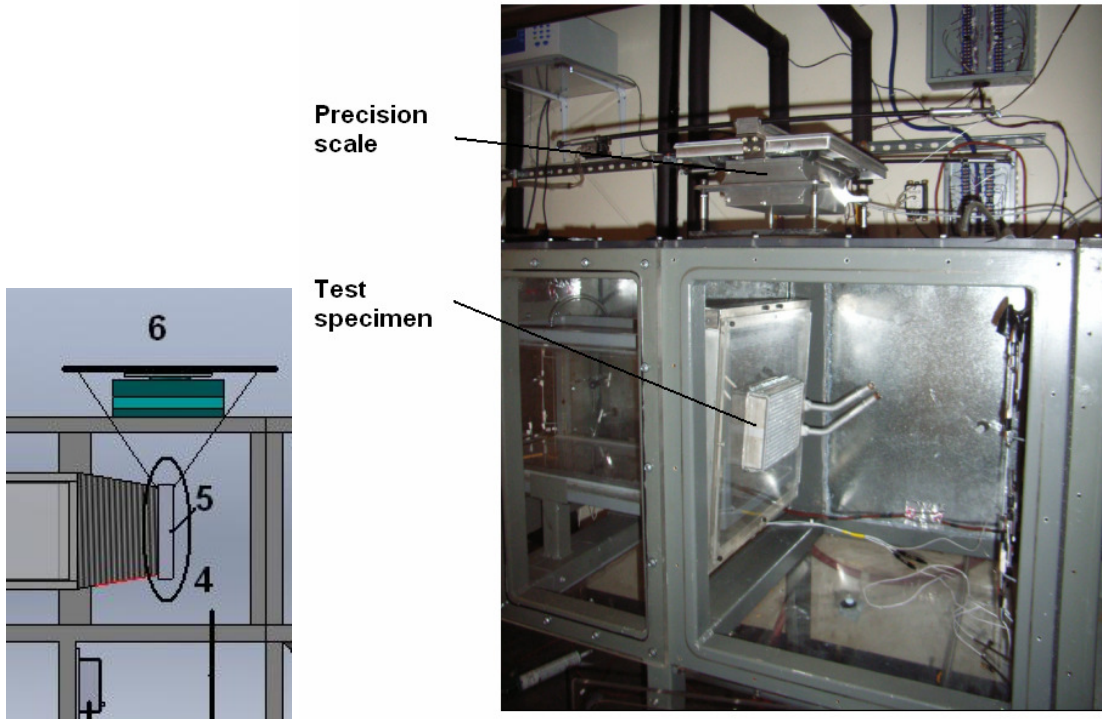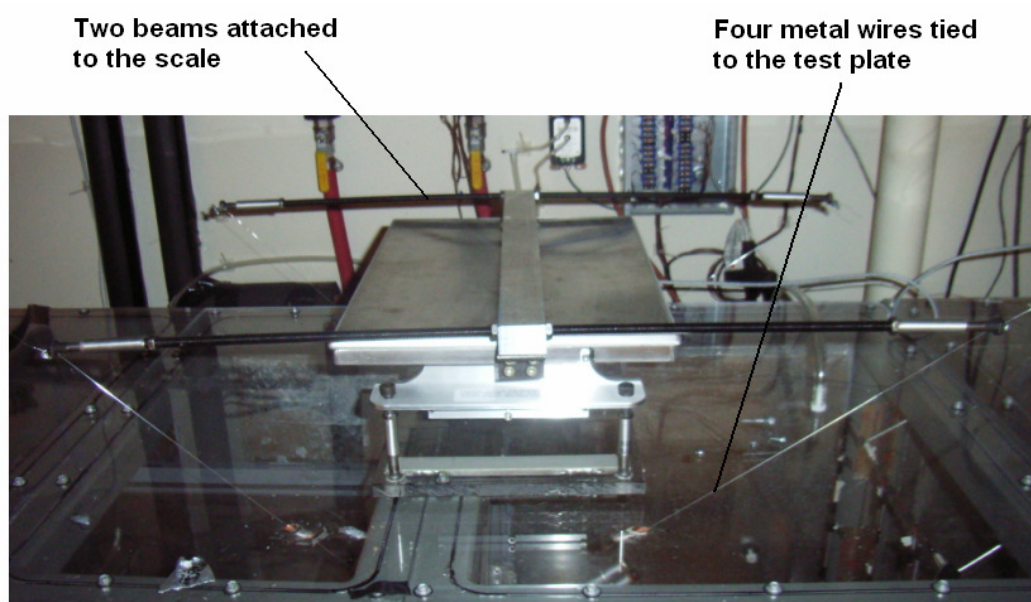
(c)

Figure 3.32   Weighing system set up

3.3.2   Equipment and instrumentation

3.3.2.1   Precision scale

The precision scale used in the lab is a 50 x 0.00015 lb (22 x 0.2 g) electronic scale from Arlyn Scales, Inc. The dimensions are 12'' (L) x 16'' (W) x 7'' (H). In current experiments, the scale was set on top of the wind tunnel. However, the vibration of the wind tunnel might have an effect on the measuring accuracy. A scale stand is recommended for further upgrades.

3.3.2.2   Videoscope

The videoscope includes a CCD camera and a fiber optic probe with diameter of 0.2 in (5.0 mm) and working length of 4.9 ft (1.5 m). The model is VP300 videoprobe system from GE Inspection Technology. It is set close to the specimen to observe frost thickness.

CHAPTER IV

UNCERTAINTY ANALYSIS

Based on the equipment and instrumentation selected in the previous section, the uncertainty on the frost and heat transfer measurements was determined. Since the heat transfer coefficient of the test evaporator is strongly dependent on the actual measured quantities, such as the outlet air temperature, leaving refrigerant temperature, and flow rate, it is necessary to find the effect of each parameter on the accuracy of my methodology. These quantities also need to be limited in a range so that I can reach an acceptable uncertainty on the heat transfer coefficient and on the frost growth rate. The approach I took in the uncertainty analysis was as follows:

1. First model the heat exchangers and estimates the outlet conditions based on the input temperatures and flow rates.

2. Then, use the previous results as input of the uncertainty analysis.

During first part, I used heat transfer correlations available in the literature and validated my model with existing work in the literature. During the second part, I recalculated the heat transfer coefficients by inputting inlet and outlet conditions. From this step, I could find equipment effect to the final results. The sensitivity of parameters can also be checked by varying the inlet and outlet variables.

4.1 MAIN INSTRUMENTATION AND EQUIPMENT ACCURACY

The main instrumentation and equipment selected for the project are detailed explained in previous chapters. Table 4.1 summarizes an overall specifications of the main instrumentation and equipment that are used in uncertainty propagation calculation in Enginnering Equation Solver (EES).

Table 4.1 Specifications of the main instrumentation and equipment

Item	Manufacturer	Model / Type	Nominal range	Accuracy
Sensors				
Mass flow meter	Micromotion	CFM 100 Elite	50 to 1000lbm/min (0.4 to 7.6 kg/s)	± 0.15% of flow rate
Elliptical air flow nozzle	Helander	-	150 to 500 cfm (0.07 to 0.24 m³/s)	± 2.2% of flow rate
Temperature	Omega	RTD	-328 to 500 ºF (-200 to 260 ºC)	± 0.2 ºF (0.1 ºC)
Pressure	Setra	Model 264	0 to 0.5 in WC (0 to 0.124 kPa)	± 0.25% of full scale
Dew point meter	TTI Instruments	GE Optica	32 to 122 ºF (0 to 50 ºC)	± 0.27 ºF (0.15 ºC)
Equipment				
Precision scale	Arlyn Scales	-	0 ~ 50 lb (0 ~ 22 g)	± 0.00015 lb (0.2 g)
Videoscope	GE	VP300	0 to 180 ºF (-18 ~ 82 ºC)	± 0.002 in (0.05 mm)

4.2 MICROCHANNEL AND FIN-AND-TUBE COILS SPECIMEN

Table 4.2 and 4.3 give the parameters for the two specimens tested under dry, wet and frost conditions. The uncertainty analysis is based on these two specific coils.

4.3 MICROCHANNEL AND FIN-AND-TUBE COIL MODEL

Two coil models are created in the following parts, one for MCHX and one for fin-and-tube. Both of them are simulated under dry, wet and frost condition:

Table 4.2 Configuration of microchannel heat exchanger specimen

Microchannle HX	
Coil height (inch)	12
Coil width (inch)	12
Coil depth (inch)	0.708
Tube material	Aluminum
Fin material	Aluminum
FPI	17
Tube spacing (inch)	0.5
Tube thickness (inch)	0.05
Louver pitch (inch)	0.06
Louver length (inch)	0.37
Louver angle (deg)	27
Circuits/Passes	1
Number of ports	23
Port dimension (inchxinch)	0.02 x 0.03

Table 4.3 Configuration of fin-and-tube heat exchanger specimen

Fin-and-tube HX	
Coil height (inch)	12
Coil width (inch)	12
Coil depth (inch)	0.866
Tube material	Copper
Fin material	Aluminum
FPI	18
Fin thickness (inch)	0.0039
Tube ID (inch)	0.381
Tube OD (inch)	0.405
Row pitch (inch)	0.866
Tube pitch (inch)	1
Circuits/Passes	12
Number of rows	1

4.3.1 Louvered fin microchannel coil model

The 1 x 1 ft MCHX is single pass with louvered fin. The geometry details can be found in

table 4.2.

4.3.1.1 *Simple microchannel coil model under dry condition*

The heat and mass transfer model, which is the subject of many studies was based on

energy, mass and momentum equations. A simple coil model was created for uncertainty analysis in Engineering Equation Solver (EES) by using ε – NTU method. The test microchannel coil can be treated as a single pass heat exchanger.

$$\dot{Q} = \varepsilon C_{min} (T_{a,in} - T_{ref,in})$$

[4.1]

Where

$$\varepsilon = \frac{1}{C_r} (1 - \exp(-C_r (1 - \exp(-NTU)))) \text{ if } C_{min} = C_{ref}$$

$$\varepsilon = 1 - \exp(-\frac{1}{C_r} (1 - \exp(-C_r NTU))) \text{ if } C_{min} = C_a \text{ for single phase}$$

$$NTU = UA / C_{min}$$

[4.2]

For a dry surface, the energy balance equation can be expressed as follows.

Energy balance in air side:

$$\dot{Q} = C_a (T_{a,in} - T_{a,out})$$

[4.3]

Energy balance in refrigerant side:

$$\dot{Q} = C_{ref} (T_{ref,out} - T_{ref,in})$$

[4.4]

Selecting appropriate heat transfer correlations is important for model accuracy. Several published air-side and refrigerant-side heat transfer correlations for microchannel heat exchangers were compared before selecting final correlations for this model.

4.3.1.1.1   *Air side heat transfer coefficient*

From literature review, several heat transfer coefficients are available for louvered fin microchannel model. Kim and Bullard developed the Coburn j-factor correlations for microchannel coil with root-mean-square (RMS) errors of ±14.5%, which gives a most

accurate model among the study found in the literature. The louvered fin geometry is shown in figure 4.1. Air side heat transfer coefficient is calculated by using equations [4.5], [4.6].
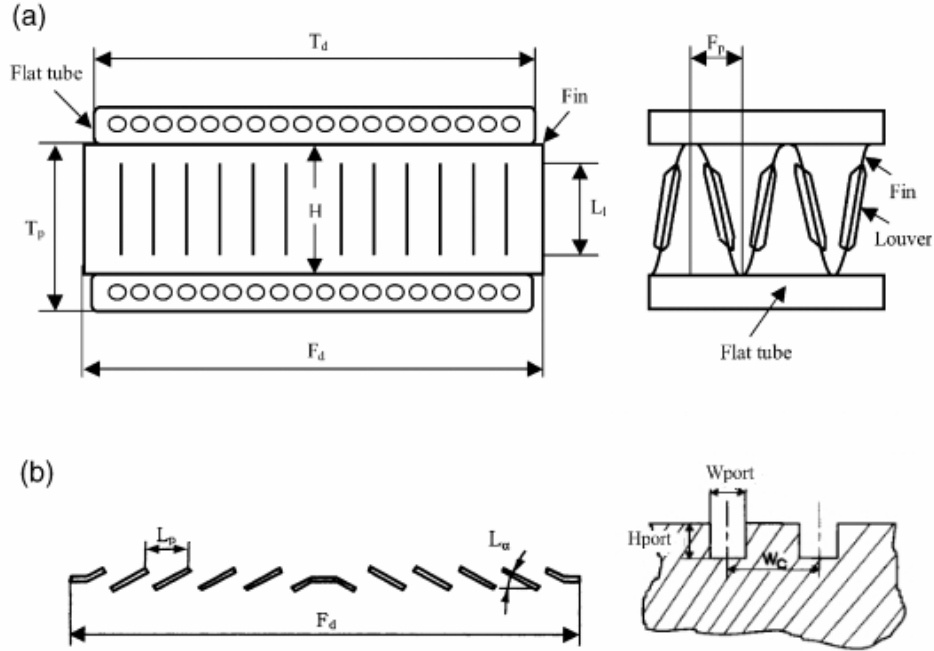
Figure 4.1 Geometry of the microchannel coil model

$$j = \mathrm{Re}_a^{-0.487} \left(\frac{L_\alpha}{90}\right)^{0.257} \left(\frac{F_p}{L_p}\right)^{-0.13} \left(\frac{H}{L_p}\right)^{(-0.29)} \left(\frac{F_d}{L_p}\right)^{-0.235} \left(\frac{L_l}{L_p}\right)^{0.68} \left(\frac{T_p}{L_p}\right)^{-0.279} \left(\frac{\delta_f}{L_p}\right)^{-0.05} \quad [4.5]$$

$$j = \frac{h_{out}}{\rho_a V_a c_a} \mathrm{Pr}^{2/3} \quad\quad [4.6]$$

Where

F_d : flow depth

H : fin height

L_l : louver length

L_p : louver pitch

L_α : louver angle

80

T_p : tube pitch

F_p : fin pitch

δ_f : fin thickness

4.3.1.1.2 Refrigerant side heat transfer coefficient

Microchannel coil consists of flat tubes with several small ports in it. The large number of ports significantly decreases the Reynolds number and the critical point of laminar and turbulent flow. Peng et al. (1996) reported that the laminar flow would start transforming to turbulent flow when Reynolds number was in a range between 200 and 700. That is the critical point for Reynolds number in microchannel tube. Peng also gave the Nusselt number relationship in the laminar flow:

$$Nu_{ref} = 0.1165(\frac{D_{in}}{W_c})^{0.81}(\frac{H_{port}}{W_{port}})^{-0.79} \text{Re}^{0.62} \text{Pr}^{1/3} \qquad [4.7]$$

Where

H_{port} : height of microchannel

W_{port} : width of microchannel

W_c : center-to-center distance of microchannel

And

$$Nu_{ref} = h_{in}D_{in} / k_{ref} \qquad [4.8]$$

Nevertheless, Peng's correlation was reported to have a 30% deviation. This error needs to be considered in the system uncertainty calculation on the heat transfer coefficients.

4.3.1.1.3 Total heat transfer coefficient

The total heat transfer coefficient is calculated according to the following equation:

$$\frac{1}{UA} = \frac{1}{h_{in}A_{in}} + \frac{\Delta x}{kA_{in}} + \frac{1}{h_{out}A\eta_{surf}} \qquad [4.9]$$

In the original coil model, the total heat transfer coefficient (U) was calculated by using air side and refrigerant side heat transfer coefficient. Based on this value, the total heat transfer could be found by equation [4.1]. The outlet condition of both sides was determined by equation [4.3] and [4.4]. The uncertainty model was created based on the original model. In uncertainty calculation, U was no longer calculated from equation [4.9], but from equation [4.2] by calculating effectiveness in equation [4.1]. The outlet condition was selected from previous simulation results and input as known value. Since air side coefficient is predominant in the total heat transfer, the uncertainty of air side heat transfer coefficient was also considered in my uncertainty analysis.

4.3.1.2 Simple microchannel coil model under wet conditions

When the air temperature is below than the dew point, condensate occurs on the surface of the heat exchanger. Equation [4.4] can not be used any more because there are not only heat transfer, but also mass transfer between air and the heat exchanger. In this case, instead of dry bulb temperature, wet bulb temperature is used to find the specific heat of moisture air:

$$c_{pf,a} = \frac{h_{a,in} - h_{a,out}}{T_{wb,in} - T_{wb,out}} \qquad [4.10]$$

$$C_{min} = \min(c_{pf,a}m_a, c_{p,ref}m_{ref})$$

$$C_{max} = \max(c_{pf,a}m_a, c_{p,ref}m_{ref})$$

Equation [4.1] also needs a modification with consideration of wet bulb temperature:

$$\dot{Q} = \varepsilon C_{min} (T_{wb,in} - T_{ref,in})$$ [4.11]

4.3.1.2.1 Air side heat transfer coefficient

Since there are both sensible and latent heat transfer, air side heat transfer coefficient is different from dry condition. The correlation is still selected from Kim and Bullard's (2001) model:

$$j = Re_a^{-0.512} (\frac{L_\alpha}{90})^{0.25} (\frac{F_p}{L_p})^{-0.171} (\frac{H}{L_p})^{(-0.29)} (\frac{F_d}{L_p})^{-0.248} (\frac{L_l}{L_p})^{0.68} (\frac{T_p}{L_p})^{-0.275} (\frac{\delta_f}{L_p})^{-0.05}$$ [4.12]

The above equation is suitable for Re_a between 80 and 300, and $F_p / L_p < 1$. Compared to experimental data, Kim and Bullard concluded this correlation brought in an error of ±16.9% on j factor. Based on designed geometry and air flow rate, the Reynolds number of air side is around 250, $F_p / L_p = 0.98$.

4.3.1.2.2 Refrigerant side heat transfer coefficient

Compared to the air side, refrigerant side heat transfer coefficient is not that much predominant. Mass transfer occurs between the air and the surface of heat exchanger, the refrigerant side is not affected much. Thus, the same correlation for refrigerant side heat transfer coefficient can be used in both dry and wet situation.

4.3.1.2.3 Total heat transfer coefficient

The total heat transfer coefficient, *U,* is calculated as same as in dry condition by using equation [4.9]. The thermal resistance of air side increases due to the condensate trapped

in the fins and on the surface. Total heat transfer coefficient becomes smaller with a weakened heat transfer rate. As a result, the coil capacity is reduced.

4.3.1.3 *Simple microchannel coil model under frost condition*

Similar to the wet condition, when air temperature is below the freezing point, frost becomes to form. As air temperature keeps going down during the cooling process, frost accumulates on the surface as a thermal insulation. Including both mass and heat transfer, this frosting process can apply the same method as wet condition. Air side and refrigerant side correlations are also suitable.

4.3.1.3.1 *Frost conductivity*

Lee and Kim (1997) developed a one-dimensional model for frost formation on a cold flat surface. They assumed the heat transfer between frost and the surface was one dimensional process and the thermal conductivity of frost was only depends on the density:

$$k_f = 0.132 + 3.13 \times 10^{-4} \Pr + 1.6 \times 10^{-7} \Pr^2$$

$$(50 kg/m^3 \leq \rho_r \leq 400 kg/m^3) \qquad [4.13]$$

4.3.1.3.2 *Total heat transfer coefficient in frost conditions*

Frost accumulates on the surface of heat exchanger as an insulator. Compared to dry and wet condition, frost thermal resistance should take into consideration in the heat transfer process. The total heat transfer coefficient in frost conditions is estimated as follows:

$$\frac{1}{UA} = \frac{1}{h_{in} A_{in}} + \frac{\Delta x}{k A_{in}} + \frac{\delta_f}{k_f A} + \frac{1}{h_{out} A \eta_{surf}} \qquad [4.14]$$

The weight and thickness of frost were collected from Lee and Ro (2002) to calculate frost density. In order to apply equation [4.13], the density needed to be limited in the required range.

4.3.2 Plain fin-and-tube coil model

The 1 x 1 ft fin-and-tube coil that tested in the experiment was a single row, single path with plain fin geometry. Specific geometric parameters can be found in table 4.2.

4.3.2.1 Simple plain fin-and-tube coil model under dry condition

The dry coil model of fin-and-tube heat exchanger is very similar to that of microchannel coil. The ε – NTU method can be found from [4.1] to [4.4]. Differences between microchannel and fin-and-tube model come from the following heat transfer coefficients.

4.3.2.1.1 Air side heat transfer coefficients for fin-and-tube coil

There are a number of researches on traditional fin-and-tube heat exchangers. Various correlations are developed based on diverse geometry and configuration. These correlations are restricted in differently applicable geometry ranges. Thus, it is important to check the configuration and geometry meet the correlation requirement.

By using Coburn *j* factor, we can estimate outside heat transfer coefficient from:

$$St \Pr^{2/3} = (\frac{\overline{h_{out}}}{G_c c_p})(\frac{\mu c_p}{k})^{2/3} = j \qquad [4.15]$$

For *j*-factor, having checked the application range in geometry and flow pattern, Wang's correlations were selected in this model (Wang et al.,1999):

For single row (R=1):

$$j = 0.108 \, \mathrm{Re}_{D_c}^{-0.29} \left(\frac{P_t}{P_l}\right)^{P1} \left(\frac{F_p}{D_c}\right)^{-1.084} \left(\frac{F_p}{D_h}\right)^{-0.786} \left(\frac{F_p}{P_t}\right)^{P2}$$ [4.16]

Where

$$P1 = 1.9 - 0.23 \log_e(\mathrm{Re}_{D_c})$$

$$P2 = -0.236 + 0.126 \log_e(\mathrm{Re}_{D_c})$$

For R≥2:

$$j = 0.086 \, \mathrm{Re}_{D_C}^{P3} \, N^{P4} \left(\frac{F_p}{D_c}\right)^{P5} \left(\frac{F_p}{D_h}\right)^{P6} \left(\frac{F_p}{P_t}\right)^{-0.93}$$ [4.17]

Where

$$P3 = -0.361 - \frac{0.042N}{\log_e(\mathrm{Re}_{D_c})} + 0.158 \log_e\left(N\left(\frac{F_p}{D_c}\right)^{0.41}\right)$$

$$P4 = -1.224 - \frac{0.076\left(\frac{P_l}{D_h}\right)^{1.42}}{\log_e(\mathrm{Re}_{D_c})}$$

$$P5 = -0.083 - \frac{0.058N}{\log_e(\mathrm{Re}_{D_c})}$$

$$P6 = -5.735 + 1.211 \log_e\left(\frac{\mathrm{Re}_{D_c}}{N}\right)$$

$$D_h = \frac{4 A_c L}{A_0}$$

4.3.2.1.2 *Refrigerant side heat transfer coefficient in fin-and-tube coil*

Both turbulent and laminar flow pattern may occur depending on specific coil configuration.

Dittus-Boelter equation can be used in turbulent flow:

$$\frac{\bar{h}_{in} D_{in}}{k_{ref}} = 0.023 (\mathrm{Re}_D)^{0.8} (\mathrm{Pr}_{ref})^n$$ [4.18]

Where

$$n = 0.4, t_{wall} > t_{bulk}$$

$$n = 0.3, t_{wall} < t_{bulk}$$

In laminar flow, h_{in} can be calculated by combing [4.8] with Shah and London's correlation:

$$Nu_{ref} = \begin{cases} 1.953(\text{Re}_{ref} \text{ Pr}_{ref} \dfrac{D_{in}}{L})^{1/3} & (\text{Re}_{ref} \text{ Pr}_{ref} \dfrac{D_{in}}{L}) \geq 33.3 \\ 4.364 + 0.07222 \text{ Re}_{ref} \text{ Pr}_{ref} \dfrac{D_{in}}{L} & (\text{Re}_{ref} \text{ Pr}_{ref} \dfrac{D_{in}}{L}) < 33.3 \end{cases} \qquad [4.19]$$

4.3.2.1.3 *Total heat transfer coefficien in fin-and-tube coilt*

For fin-and-tube configuration, heat transfer coefficient is calculated as follows:

$$\frac{1}{UA} = \frac{1}{h_{in} A_{in}} + \frac{\ln \dfrac{D_{out}}{D_{in}}}{2\pi k_{tube} L_{tube}} + \frac{1}{h_{out} A \eta_{surf}} \qquad [4.20]$$

4.3.2.2 *Simple plain fin-and-tube coil model under wet condition*

A fin-and-tube refrigeration coil model has been created according to the section 3.2.3.1.2. A similar ε-NTU method and same correlations for h_{in} and U are used here. The air side heat transfer coefficient depends mainly on the flow pattern and coil configuration. The Coburn j factor applied in both refrigeration coil model and this baseline model came from Wang et al.(1999), and it is calculated as follows:

$$j = 19.36 \text{ Re}_{D_C}^{J1} (\frac{P_{Pt}}{D_c})^{1.352} (\frac{P_L}{P_T})^{0.67954} (R)^{-1.291} \qquad [4.21]$$

Where the exponent:

$$J1 = 0.3745 - 1.554(\frac{F_p}{D_c})^{0.24}(\frac{P_l}{P_t})^{0.12} R^{-0.19}$$

4.3.2.3 *Simple plain fin-and-tube coil model under frost condition*

Frost model is modified based on wet coil model. Frost is considered as insulation and account in the total heat transfer coefficient:

$$\frac{1}{UA} = \frac{1}{h_{in} A_{in}} + \frac{\ln \dfrac{D_{out}}{D_{in}}}{2\pi k_{tube} L_{tube}} + \frac{\delta_f}{k_f A} + \frac{1}{h_{out} A \eta_{surf}}$$ [4.22]

4.4 UNCERTAINTY RESULTS AND DISCUSSION

Refrigerant temperature difference and refrigerant flow rate are the primary independent variables that need to be controlled during experiments. Air side temperature and air velocity also vary and affect the uncertainty on total heat transfer coefficient. Since the wind tunnel simulates an outdoor environment in winter conditions, the air flow rate is in the range of 200 to 400cfm according to ART standard 210. Although the air flow rate can not be changed based on uncertainty result, the sensitivity of air flow rate and temperature differences can be highlighted in the following analysis.

Uncertainty analysis is calculated based on the result from the coil model. The effect of air and refrigerant side temperature differences, flow rate were investigated. Only one variable was varied at a time while keeping all other variables fixed. In order to have convergence of the EES numerical program, the range of temperatures input and guessed flow rates during the sensitivity analysis could not be too far away from the simulated results estimated by the coil model. Air and refrigerant sides temperatures could be found from equation [4.3] and [4.4]. Since the uncertainty came from

thermocouples during the temperature measurement, both air and refrigerant side effect needed to be considered. Thus,

$$\dot{Q}_a = C_a(T_{a,in} - T_{a,out})$$

$$\dot{Q}_{ref} = C_a(T_{a,in} - T_{a,out})$$

$$\dot{Q} = (\dot{Q}_a + \dot{Q}_{ref})/2 \qquad\qquad [4.23]$$

With inlet and outlet conditions of both refrigerant and air, equation [4.22], [4.1], [4.2] and [4.9] can calculate U, h_{out} and give the uncertainty based on current equipment and instrumentation.

The uncertainty propagation was calculated by EES automatically. The method used is

$$U_Y = \sqrt{\sum_i (\frac{\partial Y}{\partial X_i})^2 U_x^2} \qquad\qquad [4.24]$$

Where

U_Y represents the uncertainty of the variable Y

U_X represents the precision accuracy of the measured variable X

Take the uncertainty on U for example. When the air flow rate was 600 cfm and the refrigerant flow rate was 4 GPM, outlet conditions were calculated in the coil model. Then in the uncertainty model, the total heat transfer coefficient is the function of all measured parameters:

$$U = \frac{c_{p,a}m_a(T_{a,in} - T_{a,out}) + c_{p,ref}m_{ref}(T_{ref,out} - T_{ref,in})}{2A_{out}\dfrac{(T_{a,in} - T_{ref,out}) - (T_{a,out} - T_{ref,in})}{\ln\dfrac{T_{a,in} - T_{ref,out}}{T_{a,out} - T_{ref,in}}}} \qquad\qquad [4.25]$$

The derivatives of all the parameters can be found from equation [4.25]. Take the refrigerant flow rate as an example:

$$\frac{\partial U}{\partial m_{ref}} = \frac{c_{p,ref}(T_{ref,out} - T_{ref,in})}{2A_{out}\dfrac{(T_{a,in} - T_{ref,out}) - (T_{a,out} - T_{ref,in})}{\ln\dfrac{T_{a,in} - T_{ref,out}}{T_{a,out} - T_{ref,in}}}} = 0.009714$$

Based on the instrument accuracy, the derivatives of all variables were found as follows:

m_{ref} = 2183±2.183 [lbm/h]	$\partial U / \partial m_{ref}$ = 0.009714	0.01 %
Q_s = 600±13.2 [cfm]	$\partial U / \partial Q_s$ = 0.03532	5.68 %
$T_{a,in}$ = 35±0.2 [F]	$\partial U / \partial T_{a,in}$ = -0.01722	0.00 %
$T_{a,out}$ = 25.33±0.2 [F]	$\partial U / \partial T_{a,out}$ = -5.696	33.91 %
$T_{ref,in}$ = 20±0.2 [F]	$\partial U / \partial T_{ref,in}$ = -1.732	3.13 %
$T_{ref,out}$ = 24.05±0.2 [F]	$\partial U / \partial T_{ref,out}$ = 7.402	57.27 %

According to equation [4.25], the uncertainty on U under 600 cfm and 4 gpm flow rate was:

$$U_U = \sqrt{(\frac{\partial U}{\partial m_{ref}})^2 U_{m_{ref}}^2 + (\frac{\partial U}{\partial Q_s})^2 U_{Q_s}^2 + (\frac{\partial U}{\partial T_{a,in}})^2 U_{T_{a,in}}^2 + (\frac{\partial U}{\partial T_{a,out}})^2 U_{T_{a,out}}^2}$$

$$\overline{+ (\frac{\partial U}{\partial T_{ref,in}})^2 U_{T_{ref,in}}^2 + (\frac{\partial U}{\partial T_{ref,out}})^2 U_{T_{ref,out}}^2}$$

$$= 42.4 \pm 1.956 \text{ [Btu/h-ft}^2\text{-F]}$$

Which means the uncertainty was ±4.6%.

4.4.1 Uncertainty of louvered fin microchannel heat exchanger

4.4.1.1 Dry condition (microchannel)

4.4.1.1.1 Uncertainty with different fluid flow rate and temperature (dry condition)

The effects of refrigerant flow rate on uncertainties of U and h_{out} are shown in figure 4.2.

Both U and h_{out} showed similar uncertainty trends if the flow rate increases. Large refrigerant flow rate and refrigerant side temperature difference would benefit the uncertainty on the two coefficients. The figures show the uncertainty decreases with an increasing flow rate. Then the curve gradually become flat and does not decrease any more. The optimum flow rate is around 3 to 5gpm. From the temperature perspective, if the refrigerant temperature difference varies from 1.5 ºF to 2 ºF, the system uncertainty decreases by almost 4 percent. With a 2.5 ºF temperature difference, the uncertainty was estimated to within ±7%.

Table 4.4 lists three cases chosen under dry condition for uncertainty analysis. The air side heat transfer coefficient analysis is also shown in figure 4.2.

Table 4.4 Case data (changing refrigerant flow rate under dry condition)

Case number	ΔT_{ref} ºF	ΔT_{air} ºF	Q_{ref} GPM	Q_{air} cfm
Case 1	1.5	4.0	1~5	400
Case 2	2	5.4	1~5	400
Case 3	2.5	6.7	1~5	400

(a)   (b)
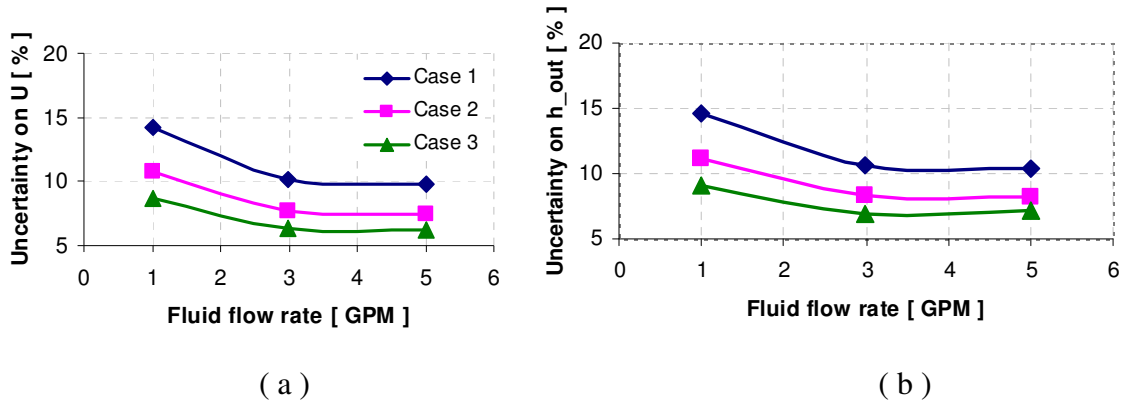
Figure 4.2 The effect of refrigerant temperature change on the total heat transfer coefficient (U) and air side heat transfer coefficient (h_{out}). Case number is indicated in table 4.4 above

The uncertainty showed in the figure is only based on equipment accuracy. But as mentioned before, equation [4.7] brings in an error within 30%. The effect of the correlation error should also be taken into consideration. According to EES results, the uncertainty on h_{out} increases only slightly with the 30% error from h_{in}. This is because the air side resistance is dominant in the heat transfer process. It is almost 35 to 106 times higher than the refrigerant side.

4.4.1.1.2 *Uncertainty with different air flow rate and temperature (dry condition)*

Air side effect is estimated as shown in figure 4.3. The cases data are listed in table 4.5

Table 4.5 lists three cases chosen in uncertainty analysis.

Table 4.5 Case data (changing air flow rate under dry condition)

| Case number	ΔT_{ref}	ΔT_{air}	Q_{ref}	Q_{air}
	°F	°F	GPM	cfm
Case a	1.8	6.5	4	200~600
Case b	2.2	8.0	4	200~600
Case c	2.7	9.7	4	200~600

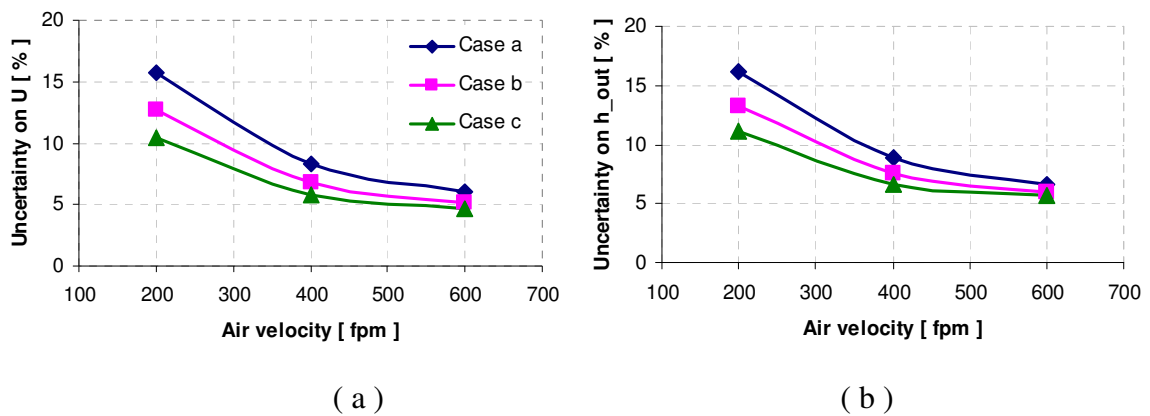(a)   (b)

Figure 4.3 The effect of air temperature change on the total heat transfer coefficient (*U*) and air side heat transfer coefficient (h_{out}). Case number is indicated in table 4.5.

Temperature effect is similar to the previous result, thus, larger air temperature difference results in lower uncertainties. This depends on the accuracy of thermocouples and RTDs. The effect of air temperature difference is not that obvious as refrigerant side. When air temperature difference increases from 6.5 ºF to 9.7 ºF, at 400cfm air flow rate, the uncertainty of U and h_{out} is lowered by nearly 4 percent. The uncertainty of h_{out} is almost ±1 % higher than U. This is because compared to h_{out}, h_{in} is much larger. Thus outside resistance is dominant in the total resistance. The error come from the refrigerant side resistance is so small that can be neglected. The error added to the outside resistance is almost all from U. As a result, both U and h_{out} have similar uncertainties. The average uncertainty for U is ±8% and ±9% for h_{out}.

4.4.1.2 Wet condition (microchannel)

4.4.1.2.1 Uncertainty with different fluid flow rate and temperature (wet condition)

Table 4.6 shows the temperature and flow rate set in the three sample cases. Uncertainty results are plotted in figure 4.4.

Table 4.6 Case data (changing refrigerant flow rate under wet condition)

Case number	ΔT_{ref}	ΔT_{air}	Q_{ref}	Q_{air}
	ºF	ºF	GPM	cfm
Case 1	1.6	4.3	1~5	400
Case 2	2.5	5.8	1~5	400
Case 3	3.0	6.6	1~5	400

(a)

(b)
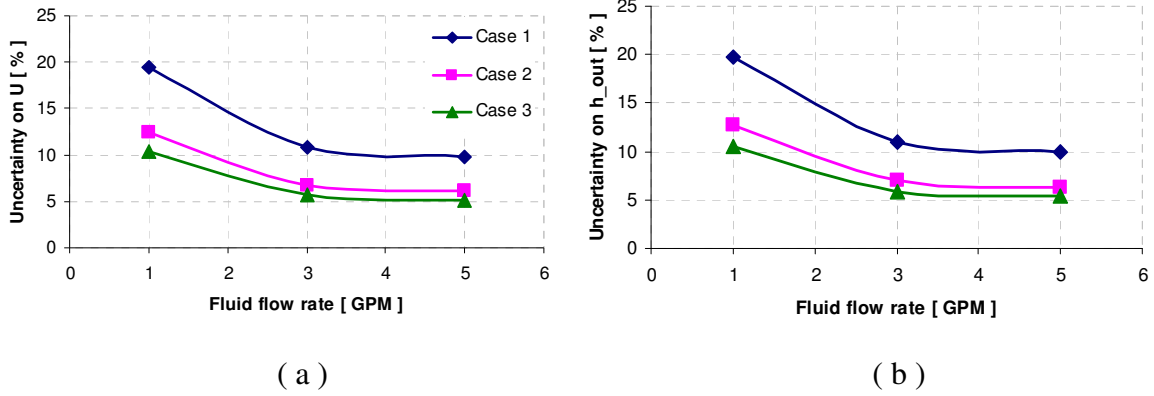
Figure 4.4 The effect of refrigerant temperature change on the total heat transfer

coefficient (*U*) and air side heat transfer coefficient (h_{out}). Case number is indicated in

table 4.6.

Compared to dry condition, the overall uncertainty increases. One explanation for

this is that with condensate occurred on the surface, the heat transfer ability of

microchannel coil is impaired. The temperature differences become smaller and more

difficult to be measured accurately with thermocouples and RTDs in the set up. For 3 to 4

gpm, the uncertainty decreases a lot with larger flow rate. At 0.9 F fluid temperature

difference, the uncertainties of both *U* and h_{out} are able to be taken down by 5 percent.

The average uncertainties for *U* and h_{out} are ±9.6% and ±9.8%. With condensate, the

outside resistance becomes even larger, decreasing the uncertainty differences between *U*

and h_{out} .

4.4.1.2.2   Uncertainty with different air flow rate and temperature (wet condition)

Table 4.7 showed the uncertainty with different air flow rate and air temperature

differences, with the uncertainty results in figure 4.5.

Table 4.7 Case data (changing air flow rate under wet condition)

| Case number	ΔT_{ref} ºF	ΔT_{air} ºF	Q_{ref} GPM	Q_{air} cfm
Case a	1.5	5.0	4	200~600
Case b	2.2	6.5	4	200~600
Case c	2.9	8.0	4	200~600

(a)   (b)

Figure 4.5 The effect of air temperature change on the total heat transfer coefficient (U) and air side heat transfer coefficient (h_{out}). Case number is indicated in table 4.7.

Similar to previous refrigerant effect, both the uncertainties on U and h_{out} increase when compare to dry condition. The average uncertainty for U is ±9.2% and h_{out} is almost the same, ±9.4%. In the case that the input temperature differences do not lead to a much higher heat transfer, the uncertainty keep decreasing with the air flow rate. When the air flow rate changes from 200 cfm to 600 cfm, the uncertainties on the two coefficients drop around 5 to 10%.

4.4.1.3 Frost condition (microchannel)

4.4.1.3.1 Uncertainty with different fluid flow rate and temperature (frost condition)

Table 4.7 and figure 4.6 show the frost situation.

Table 4.8 Case data (changing refrigerant flow rate under frost condition)

Case number	ΔT_{ref} ºF	ΔT_{air} ºF	Q_{ref} GPM	Q_{air} cfm	m_{frost} lbm	δ_{frost} in
Case a	1.0	3.5	1~5	400	0.2	0.04
Case b	1.5	4.3	1~5	400	0.2	0.04
Case c	2.2	5.3	1~5	400	0.2	0.04

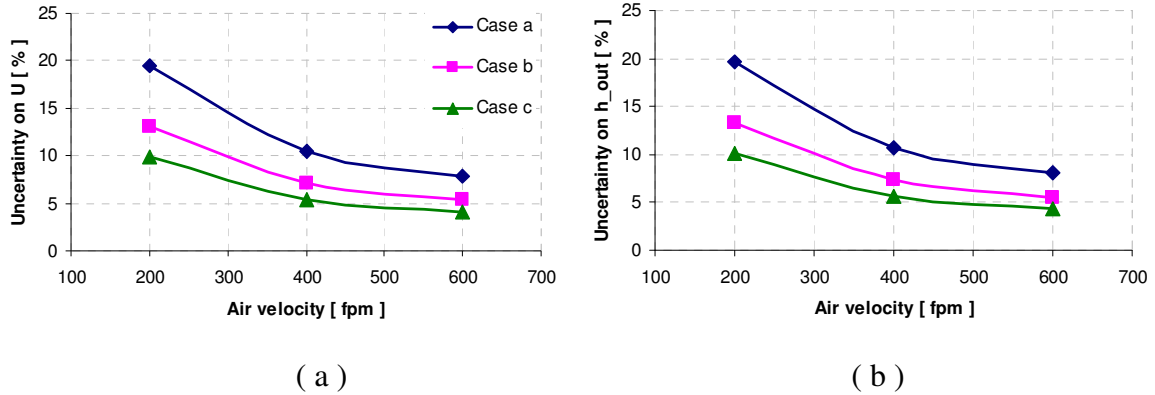(a)   (b)
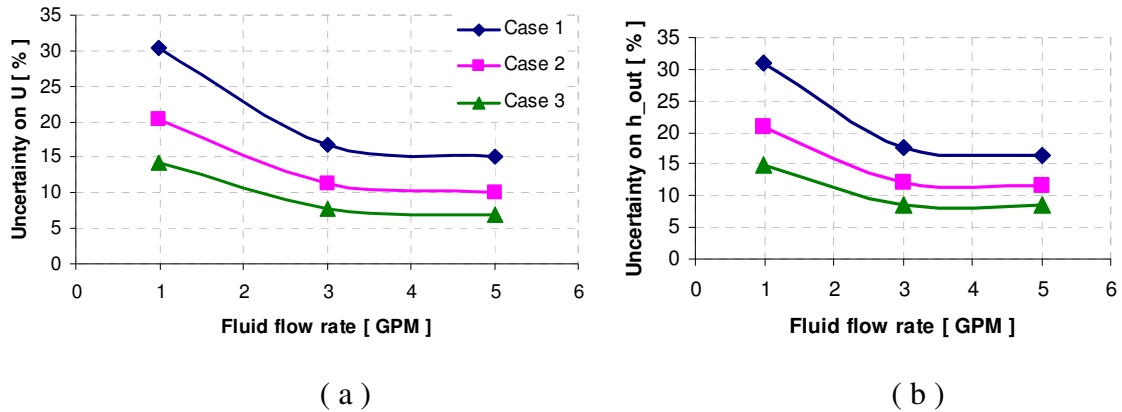
Figure 4.6 The effect of fluid temperature change on the total heat transfer coefficient

(*U*) and air side heat transfer coefficient (h_{out}). Case number is indicated in table 4.8

The average uncertainty on *U* is around ±14.8%. In a reasonable refrigerant

temperature range, the uncertainty of *U* decreases with flow rate, especially when the

flow rate is lower than 3 gpm. Compared to *U*, h_{out} has a little higher uncertainty,

±15.8%. The uncertainty is almost constant when the flow rate is larger than 3 gpm.

4.4.1.3.2   Uncertainty with different air flow rates and temperatures (frost condition)

Table 4.9 and figure 4.7 show the uncertainty under frost condition, with different air

flow rate and air temperatures.

Compared to wet condition, the uncertainties on *U* and h_{out} increase 4 to 5

percent. The average uncertainty on *U* is around ±13.6% and ±14.8% on h_{out}. When the

air flow rate varies from 200 cfm to 600 cfm, the uncertainties drop around 10 to 15%.

Till 600 cfm, both the uncertainties on U and h_{out} have the trend to keep decreasing, but

not that obvious as low flow rate. A constant value should be reached around 600 cfm.

Table 4.9 Case data (changing air flow rate under frost condition)

| Case number	ΔT_{ref} ºF	ΔT_{air} ºF	Q_{ref} GPM	Q_{air} cfm	m_{frost} lbm	δ_{frost} in
Case a	1.0	4.0	4	200~600	0.2	0.04
Case b	1.5	5.0	4	200~600	0.2	0.04
Case c	2.0	6.0	4	200~600	0.2	0.04

(a)   (b)
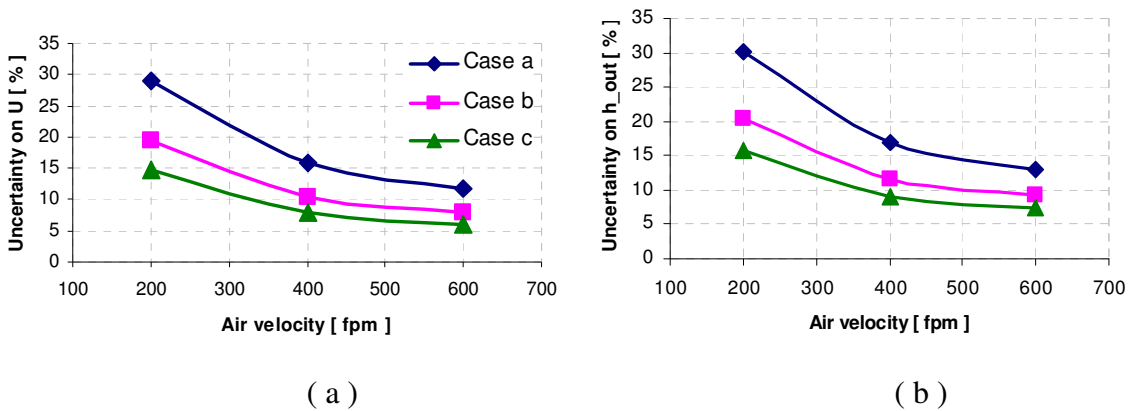
Figure 4.7 The effect of air temperature change on the total heat transfer coefficient (U)

and air side heat transfer coefficient (h_{out}). Case number is indicated in table 4.9.

4.4.1.4 Conclusion for the uncertainty analysis on U and h_{out} for louvered fin microchannel heat exchanger

Based on microchannel coil model, the effect of refrigerant side and air side temperature

differences, flow rates are discussed in previous sections. For both sides, the uncertainty

is sensitive to the temperature differences. A 0.5 to 1 ºF temperature change may result in

5 to 10% uncertainty decrease. Refrigerant temperature differences are even more

sensitive. In reasonable temperature range, higher flow rate leads to a lower uncertainty.

But when the flow rate is exceeding a certain value, the uncertainty is almost constant

and does not change with flow rate any more. Thus, it is not necessary to keep the flow rate always as high as possible. Not only because high flow rate may not affect total uncertainties a lot, also large flow rate represents a smaller temperature difference, which is not suitable for temperature measurement. Larger pressure drops may also occur with high flow rate in the system, which makes the system more difficult to control.

Considering the above reasons, recommended fluid flow rate range is 3 to 5 gpm. The temperature difference of refrigerant side should be 2.5 to 3 ºF for dry and wet condition, and 1.5 to 2 ºF for frost condition. When crossing the test heat exchanger, the air dry bulb and wet bulb temperature are expected to decrease by 5 and 8 ºF respectively.

At these operating conditions the uncertainty on the overall heat transfer coefficient and outside convective heat transfer coefficient are estimated to be in the range from ±10 to ±15%.

4.4.2 Uncertainty of plain fin-and-tube heat exchanger

4.4.2.1 Dry condition (fin-and-tube)

4.4.2.1.1 Uncertainty with different fluid flow rate and temperature (dry condition)

Figure 4.8 gives the uncertainty of heat transfer coefficients with various refrigerant temperature differences and flow rate listed in table 4.10. In the coil model, the cooling capacity of fin-and-tube heat exchanger is almost half of the microchannel coil. Thus, compared to microchannel coil, the fin-and-tube heat exchanger model is more sensitive to the refrigerant temperature difference. Input temperature differences can not be varied in a wide range, or the inappropriate capacity leads to a low air-side resistance, increasing the uncertainty on h_{out}. The uncertainty results are shown in figure 4.8 (a) and (b).

Table 4.10 Case data (changing refrigerant flow rate under dry condition)

| Case number	ΔT_{ref} ºF	ΔT_{air} ºF	Q_{ref} GPM	Q_{air} cfm
Case 1	0.5	1.34	1~5	400
Case 2	0.7	1.88	1~5	400
Case 3	0.9	2.42	1~5	400

(a)

(b)

(c)
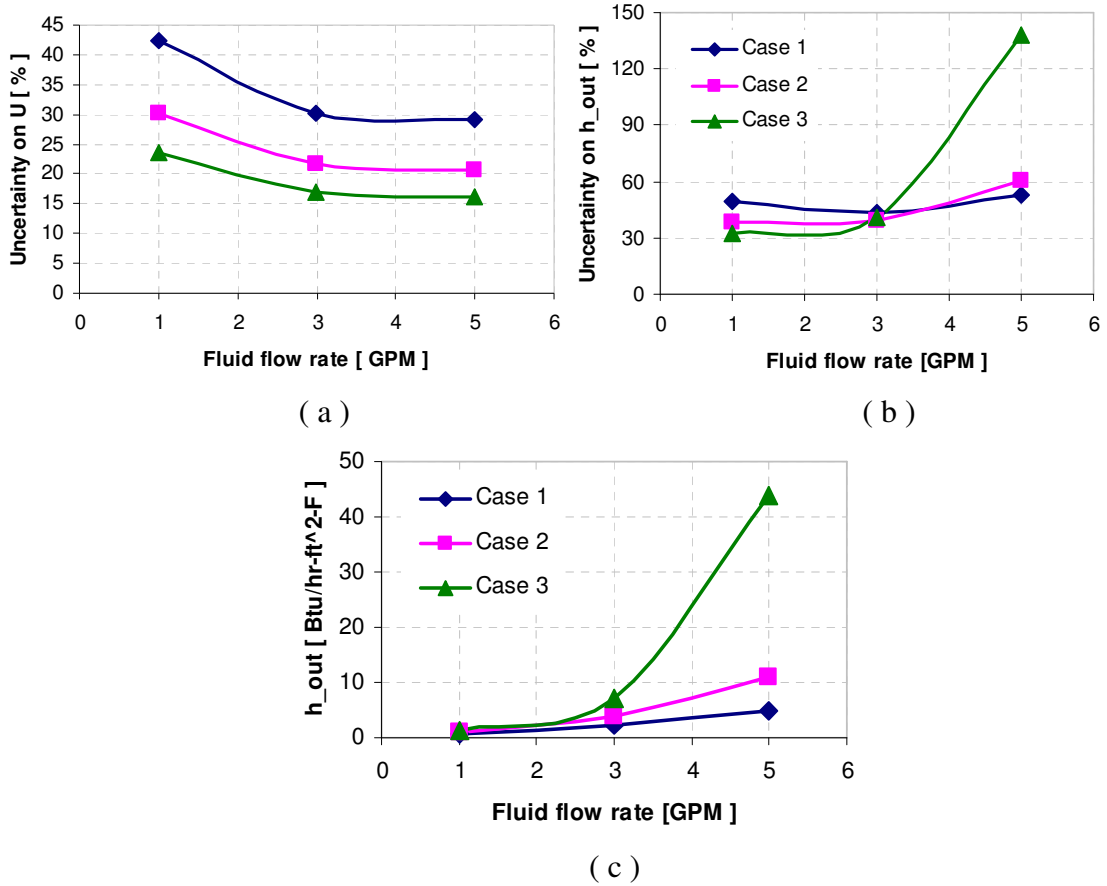
Figure 4.8 The effect of refrigerant temperature change on the total heat transfer

coefficient (*U*) and air side heat transfer coefficient (h_{out}). Case number is indicated in

table 4.10.

When trying with 1 ºF refrigerant temperature difference with 3 to 5 GPM, the

uncertainty for *U* is able to achieve 15%, and 30% for convective heat transfer

coefficient. Air side temperature increases around 2.5 ºF. Different from the

microchannel coil, the refrigerant side resistance can not be neglected in the total

resistance, because of a small h_{in}. As the flow rate increases, h_{out} becomes larger with a smaller air side resistance. One the outside resistance is close to or lower than the refrigerant side resistance, the uncertainty on h_{out} starts to increase, as shown in figure 4.8 (c).

This is because the errors from U are all conducted to air side resistance, however, the errors from the refrigerant side should not be ignored. Thus, the uncertainty starts to increase because it includes the error for the inside resistance. Based on this phenomenon, appropriate initial guesses are important for the uncertainty and ranges are limited. Once exceed the appropriate range, an unrealistic h_{out} occurs, leading to uncertainty increasing.

4.4.2.1.2 Uncertainty with different air flow rates and temperatures (dry condition)

Figure 4.11 is the sensitivity of air side temperature differences and flow rates.

Table 4.11 Case data (changing air flow rate under dry condition)

| Case number	ΔT_{ref} ºF	ΔT_{air} ºF	Q_{ref} GPM	Q_{air} cfm
Case a	0.56	2	4	200~600
Case b	0.67	2.4	4	200~600
Case c	0.75	2.7	4	200~600

(a) (b)

100
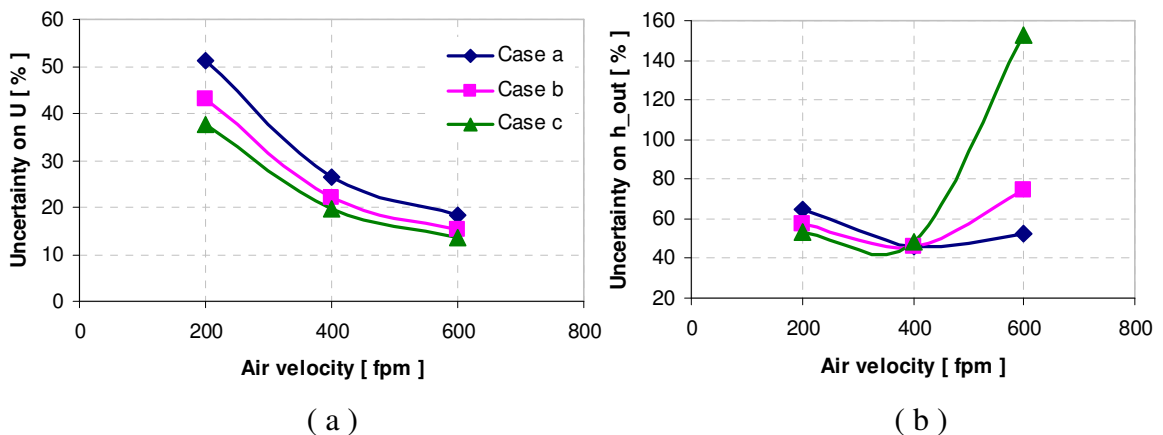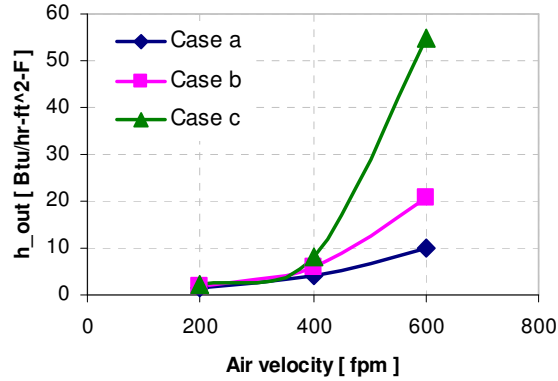
(c)

Figure 4.9 The effect of air temperature change on the total heat transfer coefficient (*U*)

and air side heat transfer coefficient (h_{out}). Case number is indicated in table 4.11.

As refrigerant side mentioned in previous section, inappropriate guesses lead to a

small outside resistance, and bring up the uncertainty of air side heat transfer coefficient.

The uncertainty on both *U* and h_{out} are large, around ±20% on *U* and ±40% on h_{out} . This

is because the small temperature differences. Larger values will definitely decrease the

uncertainty. But since the dry model is very sensitive, the program can not be converged

when changing the variables in a wider range.

4.4.2.2   Wet condition (fin-and-tube)

4.4.2.2.1   Uncertainty with different fluid flow rate and temperature (wet condition)

Compared to the dry condition, wet coil model is not that much sensitive to the

temperature range. From table 4.12, we can see larger temperature differences are

selected to both air and refrigerant sides. These bring the uncertainty of *U* down to ±20 ~

±25%, and h_{out} is around ±25 to ±30%. It is true that the uncertainty on *U* is higher than

the cases in dry condition. However, the uncertainty on h_{out} is decreased when the coil

surface is wet. The reason is with condensation, outside resistance is higher than dry

101

condition. With a larger number, the affect of the error coming from the inside resistance is not that much as dry coil. This can be seen from figure 4.10 (b). The uncertainty on h_{out} does not increase a lot as the one in figure 4.8 (b).

Table 4.12 Case data (changing refrigerant flow rate under wet condition)

Case number	ΔT_{ref} ºF	ΔT_{air} ºF	Q_{ref} GPM	Q_{air} cfm
Case 1	0.5	2.77	1~5	400
Case 2	1	3.54	1~5	400
Case 3	1.5	4.32	1~5	400

(a)

(b)

(c)
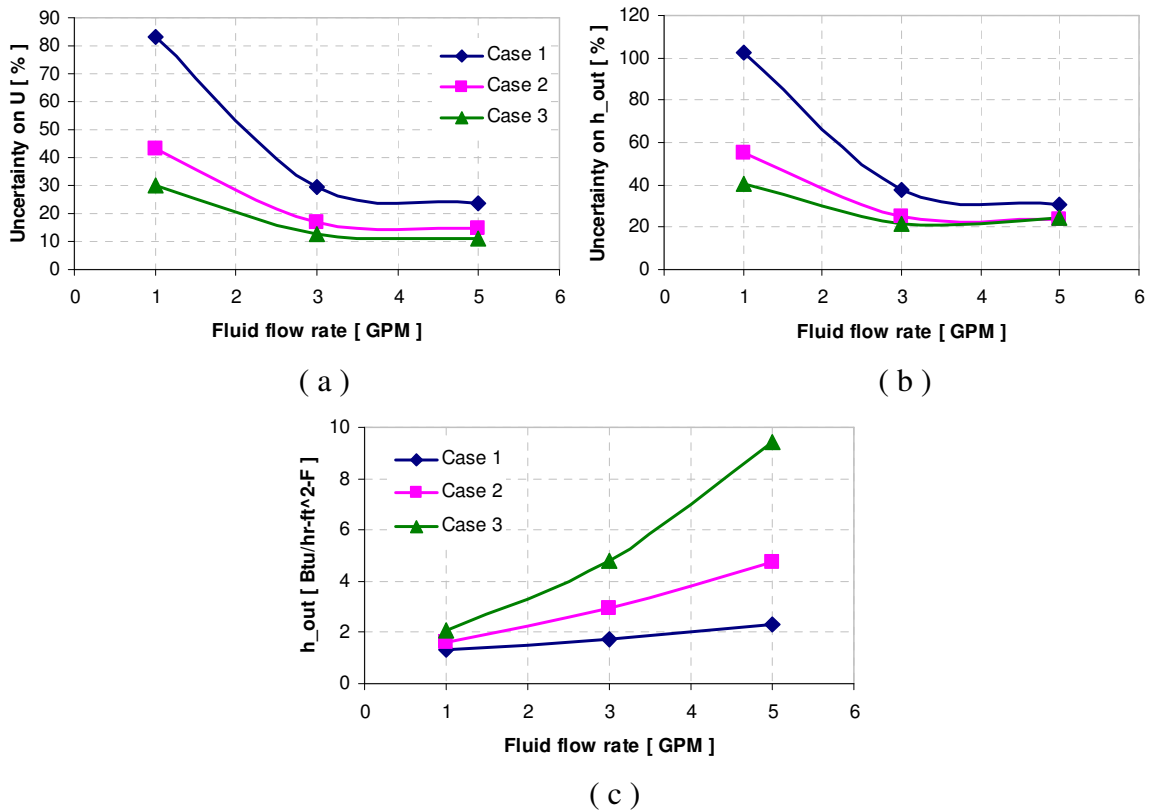
Figure 4.10 The effect of refrigerant temperature change on the total heat transfer coefficient (*U*) and air side heat transfer coefficient (h_{out}). Case number is indicated in table 4.12.

When I set the refrigerant side temperature difference to be 1.5 ºF with 4 GPM flow rate, h_{out} exceed the normal range as shown in figure 4.10 (c). That is why the uncertainty starts increasing in case 3.

4.4.2.2.2 Uncertainty with different air flow rate and temperature (wet condition)

The sensitivity of air flow rate and air temperature differences on uncertainty of U and h_{out} are shown in figure 4.11. At 600 cfm, when the air temperature differences at 3.3 ºF, the air side resistance is almost the same as refrigerant side. At 3.7 ºF, the air side resistance is lower than refrigerant side, while at 4.3 ºF, it is almost half of inside resista-- nce. Thus, the uncertainty of h_{out} starts to increase in the range of 400 to 600 cfm, and increases faster once the refrigerant side resistance becomes predominant.

Under wet condition, the average uncertainty on U is ±21%, while approximately ±28% on h_{out} .

Table 4.13 Case data (changing air flow rate under wet condition)

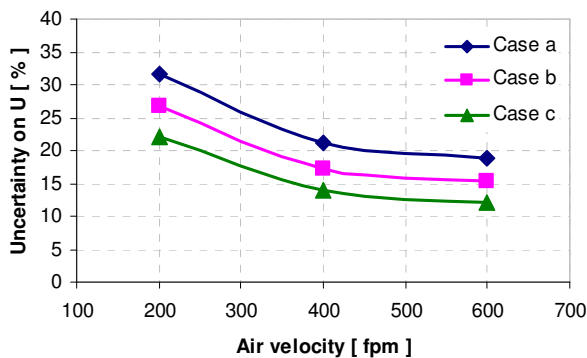| Case number	ΔT_{ref} ºF	ΔT_{air} ºF	Q_{ref} GPM	Q_{air} cfm
Case a	0.63	3.3	4	200~600
Case b	0.83	3.7	4	200~600
Case c	1.12	4.3	4	200~600
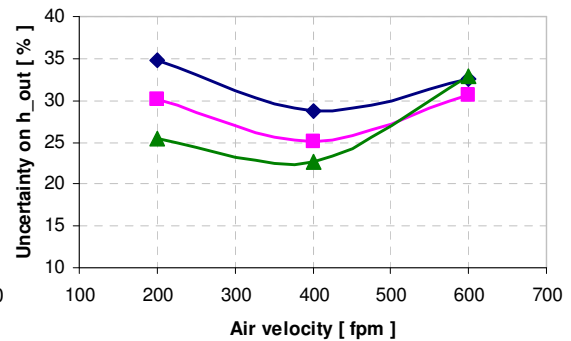
(a)   (b)
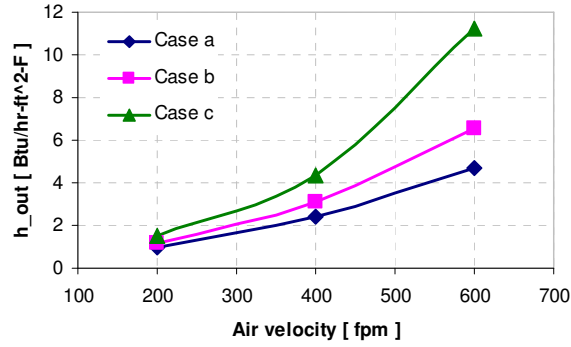
(c)

Figure 4.11 The effect of air temperature change on the total heat transfer coefficient (*U*) and air side heat transfer coefficient (h_{out}). Case number is indicated in table 4.13.

4.4.2.3 Frost condition (fin-and-tube)

4.4.2.3.1Uncertainty with different refrigerant flow rate and temperature(frost condition)

Table 4.14 shows the cases selected under frost condition with different refrigerant flow rate and temperatures. When the refrigerant temperature difference varies from 0.5 ºF to 1.0 ºF, the uncertainty on *U* decreases 20 to 30%, almost two times of the change from case 2 to 3. The average uncertainty is ±26%. Same trend happens on h_{out}. Varying temperature differences from 0.5 ºF to 1.0 ºF significantly decreases the uncertainty when the flow rate is lower than 3 gpm. The average uncertainty on h_{out} is ±40%.

Table 4.14 Case data (changing refrigerant flow rate under frost condition)

Case number	ΔT_{ref} ºF	ΔT_{air} ºF	Q_{ref} GPM	Q_{air} cfm	m_{frost} lbm	δ_{frost} in
Case 1	0.5	2.77	1~5	400	0.2	0.04
Case 2	1.0	3.54	1~5	400	0.2	0.04
Case 3	1.5	4.32	1~5	400	0.2	0.04

104

(a)

(b)

(c)
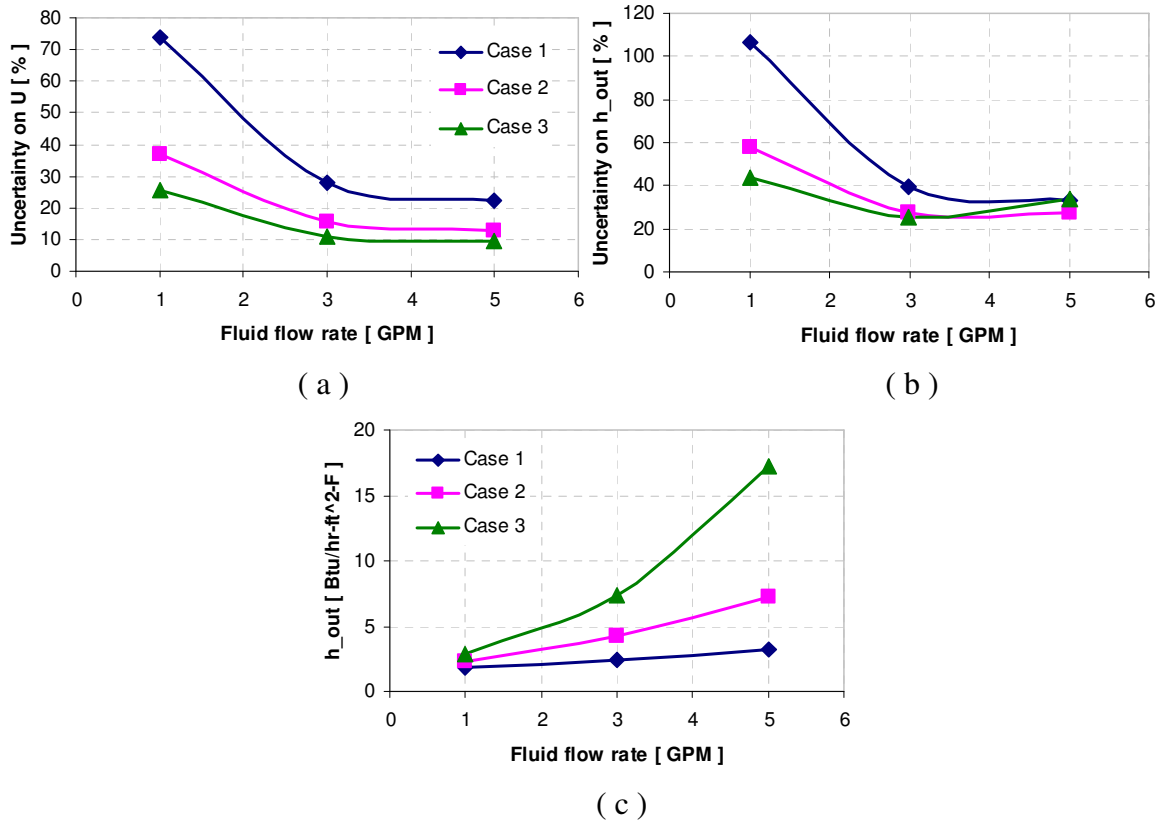
Figure 4.12 The effect of refrigerant temperature change on the total heat transfer

coefficient (*U*) and air side heat transfer coefficient (h_{out}). Case number is indicated in

Table 4.14.

4.4.2.3.2   Uncertainty with different air flow rate and temperature (frost condition)

The air side effects are shown in table 4.15 and figure 4.13.

The uncertainties are ±20% on *U* and ±36% on h_{out}. The uncertainty increases

when compared to the wet condition due to the smaller temperature differences, which is

caused by the lower cooling capacity.

Table 4.15 Case data (changing air flow rate under frost condition)

| Case number	DT_ref	DT_a	Q_ref	Q_s	m_frost	delta_frost
Case a	0.53	3.1	4	200~600	0.2	0.04
Case b	0.83	3.7	4	200~600	0.2	0.04
Case c	1.22	4.5	4	200~600	0.2	0.04
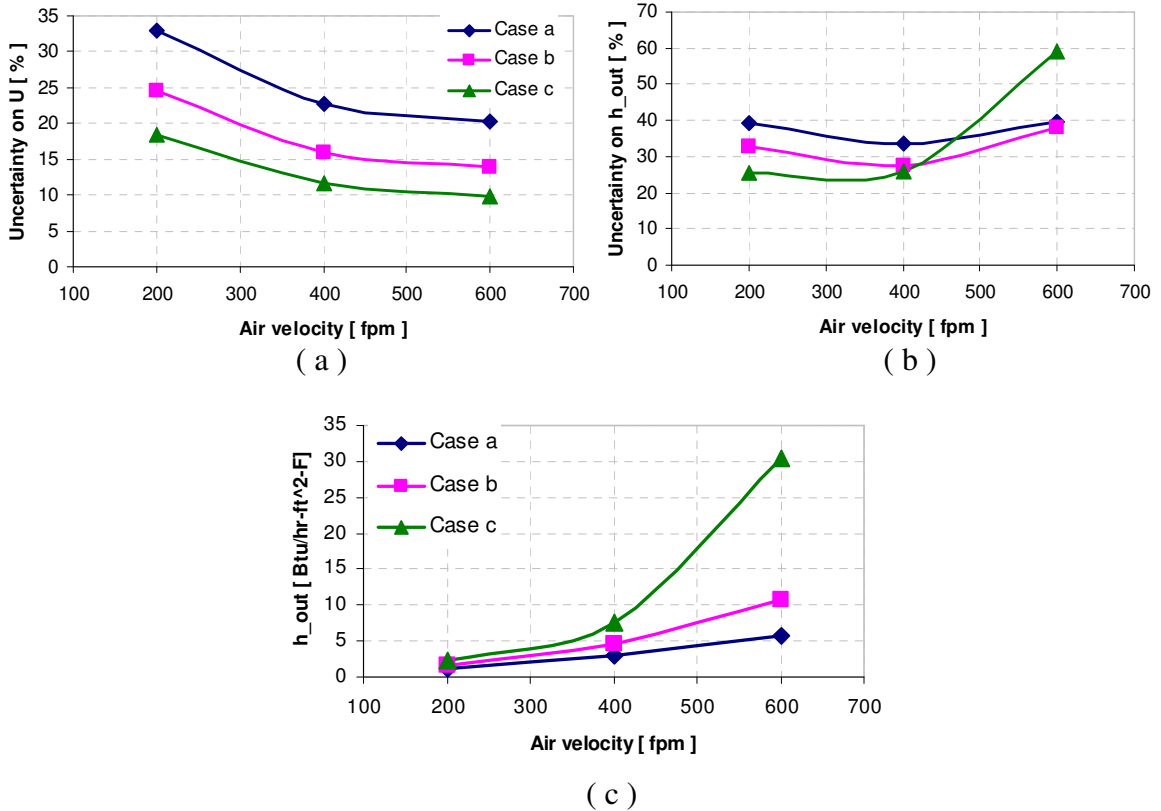
Figure 4.13 The effect of air temperature change on the total heat transfer coefficient (*U*) and air side heat transfer coefficient (h_{out}). Case number is indicated in table 4.15.

4.4.2.4 Conclusion for the uncertainty analysis on U and h_{out} for plain fin-and-tube heat exchanger

Compared to microchannel coil, the fin-and-tube heat exchanger has a much lower capacity. The model is more sensitive to the temperature and flow rate guesses. Since refrigerant side heat transfer coefficient h_{in} is very low, the inside resistance affects the uncertainty results. With inappropriate initial input, a larger h_{out} may be obtained as a result. This unrealistic value represents a smaller air side resistance. Once air side resistance is close or lower than the refrigerant side, the air side is not predominant value any more. The error to the refrigerant side needs to be taken into consideration.

Nevertheless, during the uncertainty analysis on h_{out}, all the errors from U are conducted to the air side since when I input h_{in}, I assume the uncertainty is 0%. As a result, the uncertainty on h_{out} increases when the flow rate exceed a certain range.

Generally, from the above analysis, the recommended flow rate for air side is 400 to 600 cfm, and 3 to 5 gpm for the refrigerant side. The uncertainties on both U and h_{out} are more sensitive to the refrigerant temperature differences, when compared to the air side.

CHAPTER V

CALIBRATION AND PRELIMINARY RESULTS

The compact temperature control unit, re-heating coil, refrigeration coil and the fan are all controlled automatically using Labview program, which was developed by Sankaranarayanan K. Padhmanabhan, Ph.D student at Oklahoma State University. The procedures of running labview program and the chiller are described in the Appendix D, E and F.

5.1 PRELIMINARY EXPERIMENTAL RESULTS

5.1.1 Preliminary experiments to calibrate the facility

Figure 5.1 below shows a schematic of the wind tunnel in the air flow laboratory and key state points of the air stream in the loop.

The objectives of the preliminary experiments are as follows:

1) Verify that 35/33 ℉ dry-bulb and wet-bulb temperature can be reached in steady state stable operating conditions of the facility;

2) Test that Labview program and control scheme work correctly;

3) Validate that the cooling coil provides enough cooling and dehumidifying capacity.
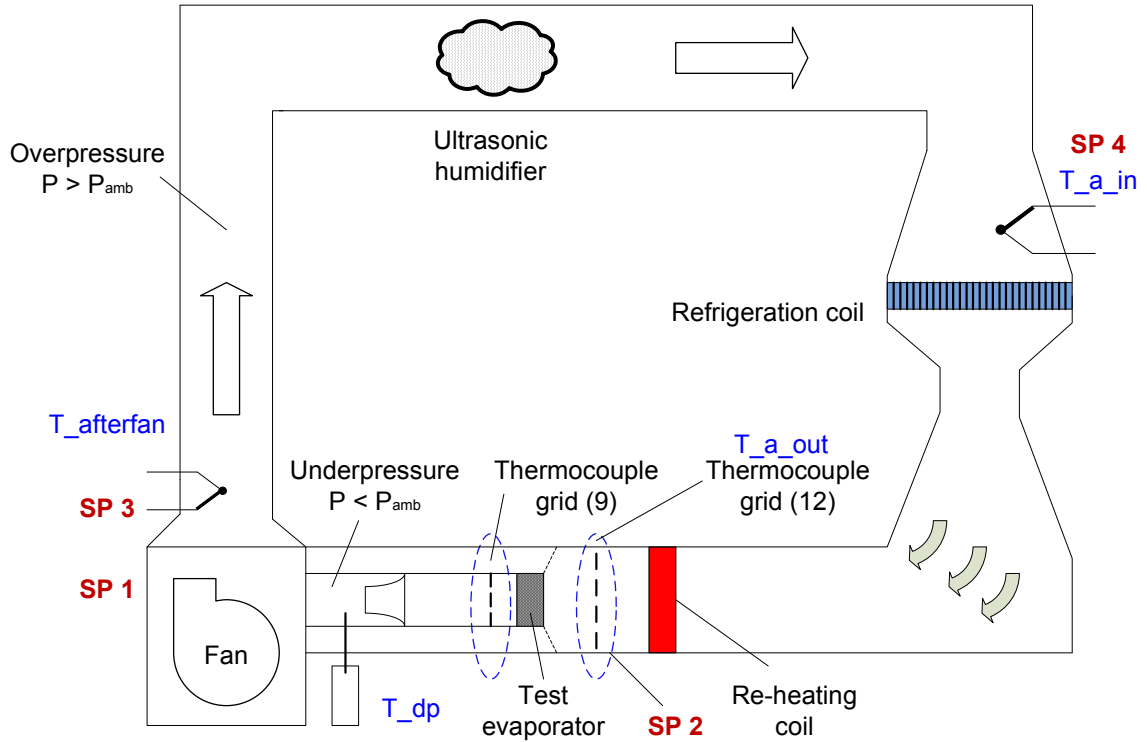
Figure 5.1 Sketch of the air wind tunnel loop and key state points

The preliminary experiments were conducted without humidity control and both the re-heating coil and the humidifier were off. This was the first step necessary to calibrate the chiller and air flow in the wind tunnel. The cooling and dehumidifing processes are shown in figure 5.2. The thermocouple grid with 12 measuring points measured the outlet air temperature from the cooling coil (state point 2). Two extra thermocouples were inserted into the duct to measure air temperature after the fan (state point 3) and inlet air condition (state point 4) before the cooling coil. The fan is the place where the conditioned air mixed with the ambient condition. After the fan, the section of tunnel is over pressuring. Thus air might escape but not enter in. So I assume the air partially enter the wind tunnel at the inlet of the fan, which is the lowest depression point of the air loop. Considering the heat gain in the loop, one thermocouple was temporarily

inserted for air temperature before the cooling coil. With reference to figure 5.2 below, due to small infiltration, the ambient air (state point 1) enters into the duct and it mixes with the conditioned air (state point 2), resulting in both temperature and humidity increase. Based on the previous assumption that infiltration only happens before the fan, the two state points 3 and 4 should have the same humidity level because no other water vapor was added to the air system. One chilled mirror installed before the flow nozzle was used for determining dew point temperature before the fan. In the cooling coil, the air is cooled and dehumidified. The preliminary results give us a better idea of the process in the cooling coil, thus process 4 to 2 as shown in the figure 5.2.
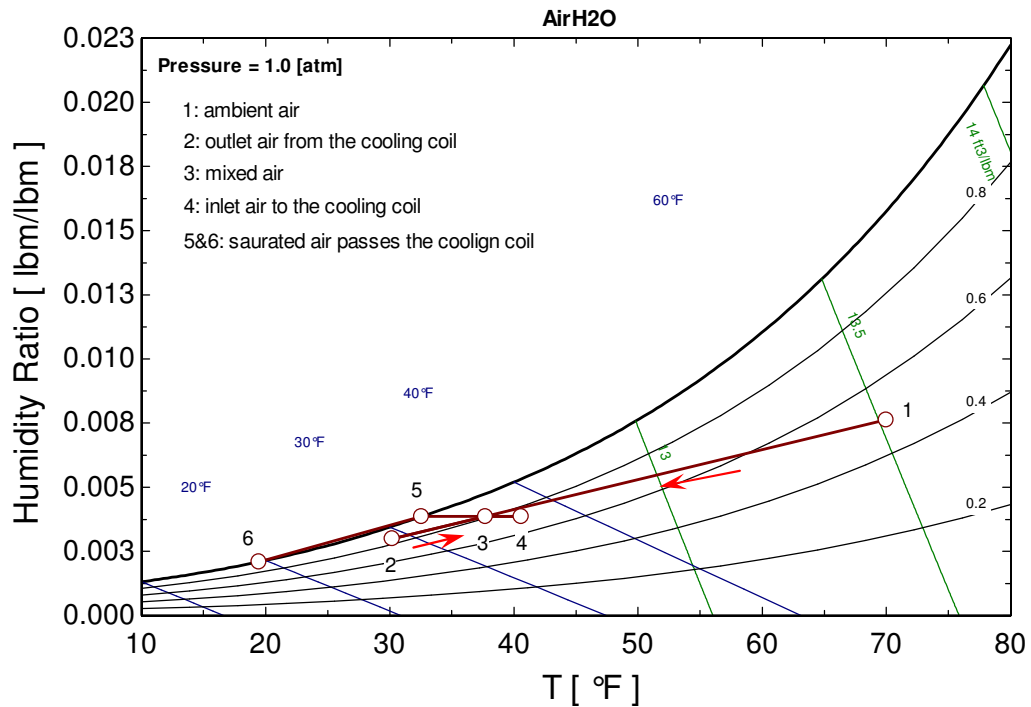

Figure 5.2 Psychrometric chart of cooling and dehumidification process of the air in the air flow wind tunnel

5.1.2 Preliminary experimental results analysis

Figure 5.3 gives the preliminary experimental results about the temperature data at the critical state points in the air flow wind tunnel. The measurements indicate a pull-down period of about 2 hours from ambient condition to 30°F. After about 3 hours of continuous running, the air stream is considered to be reached steady state low temperature frosting conditions.
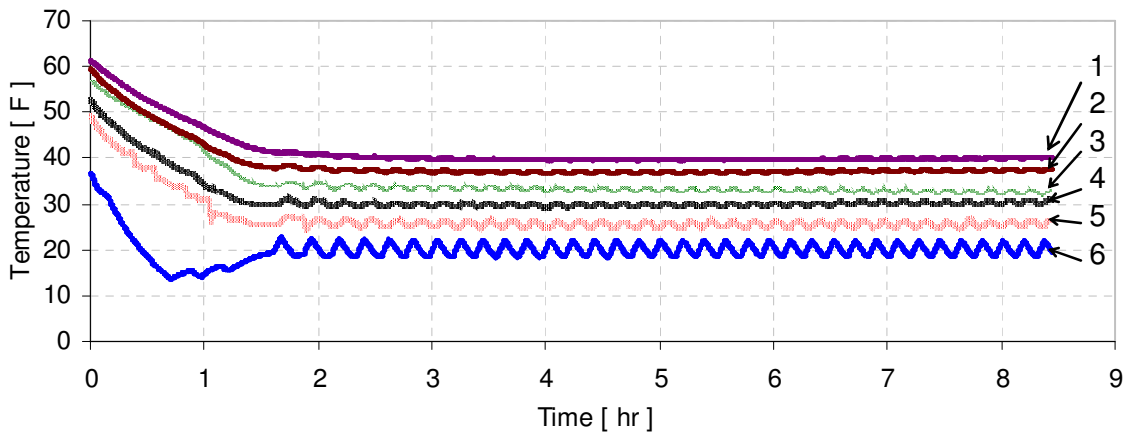
1	Inlet air temperature to the refrigeration cooling coil	2	Air temperature after the fan
3	Return temperature of fluid to the chiller	4	Outlet air temperature from the cooling coil
5	Dew point before the fan	6	Leaving temperature of the fluid from the chiller

Figure 5.3   Preliminary experimental results

Since the re-heating coil was off, the air temperature before the test section is controlled by adjusting the set point of the chiller. In this preliminary experiment, the set point of the chiller was 19 ºF (-7.2 ºC), with an upper and lower limit of 3 ºF. The data were recorded for about 8 hours of continuous running and the facility was able to operate for 2 to 3 days without requiring any defrost of the refrigeration coil or any interruption of the chiller. At steady state conditions, the air and chiller refrigerant temperatures at the inlet and outlet of the refrigeration coil are summarized in table 5.1.

Table 5.1 Preliminary results

1	$T_{a,in} \approx 40.6\ ^{\circ}F\ (4.8\ ^{\circ}C)$	2	$T_{afterfan} \approx 37.7\ ^{\circ}F\ (3.2\ ^{\circ}C)$
3	$T_{ref,out} \approx 33.7\ ^{\circ}F\ (0.9\ ^{\circ}C)$	4	$T_{a,out} \approx 30.2\ ^{\circ}F\ (-1.0\ ^{\circ}C)$
5	$T_{dp} \approx 27.0\ ^{\circ}F\ (-2.8\ ^{\circ}C)$	6	$T_{ref,in} \approx 19.7\ ^{\circ}F\ (-6.8\ ^{\circ}C)$

It should be noted that the microchannel coil test section was not installed during this experiment. The only cooling effect is provided by the refrigeration coil while the heating effects are due to air infiltration and heat conduction through out the air duct of the wind tunnel.

5.1.2.1 *Cooling coil model validation*

The cooling coil model was described in previous chapters. The model was created for wet condition by using ε-NTU method. Figure 5.4 gave the calculated outlet air and refrigerant temperatures, together with the cooling capacity.
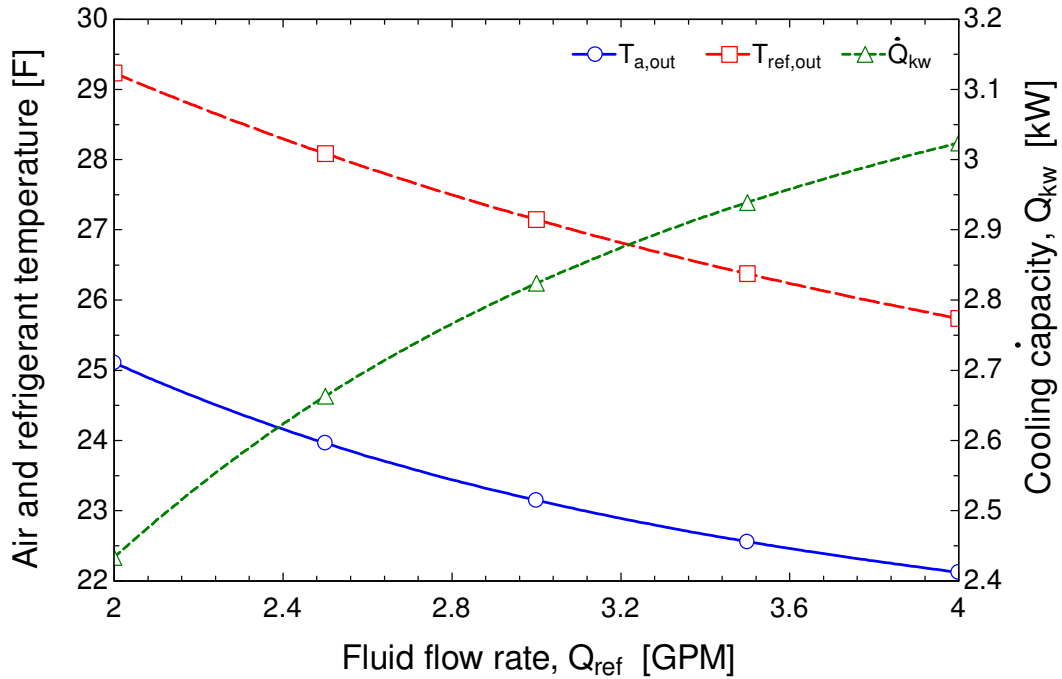

Figure 5.4 Coil model results

Since the refrigerant flow rate from the chiller was not measured during the preliminary experiment, in the microchannel model the fluid flow rate was varied from 2 to 4 GPM. Compared to experimental data, the error of model was within 30% of error on 7 ºF for the outlet air temperature and 6 ºF for the refrigerant temperature. There are three possible reasons:

1. Uncertainty from the experimental correlations selected for the model. When calculated air-side heat transfer coefficients, the correlation selected has a certain uncertainty associated with them in the range of ±15%.

2. Underestimate the air side pressure loss. In the design part, the correlations in the model were suitable for an air side Re between 200 to 20,000, which means the air flow rate should be at least 450 cfm. This is possible according to the fan curve. However, there were two soft connections in the air loop and caused a much larger pressure drop. The actual air flow rate that the fan can reach was only 380 cfm, decreasing the Re lower than 200 and made the model out of range a little bit.

3. Air bypass effect. Not all the air went through the cooling coil and took the cooling process. When the conditioned air mixed with the bypass, outlet temperature raised. That is also another possibility to explain why the model temperature was lower than the experimental data.

5.1.2.2 *Cooling process in the refrigeration coil*

The outlet air condition from the refrigeration coil can be determined from the chilled mirror and the thermocouple grid before the fan, which is state point 2 as shown in figure 5.5. The state point was not in the saturated line, which means the bypass effect could not be neglected. In the refrigeration coil, part of the air was cooled down to the saturated

status. This is process 4 to 6 as shown in the figure 5.5. On the other hand, a certain amount of air bypassed the refrigeration coil, maintaining inlet air temperature, humidity, and then had a mix with the conditioned air. The mixer point was the outlet air condition obtained from the chilled mirror and the thermocouple grid.
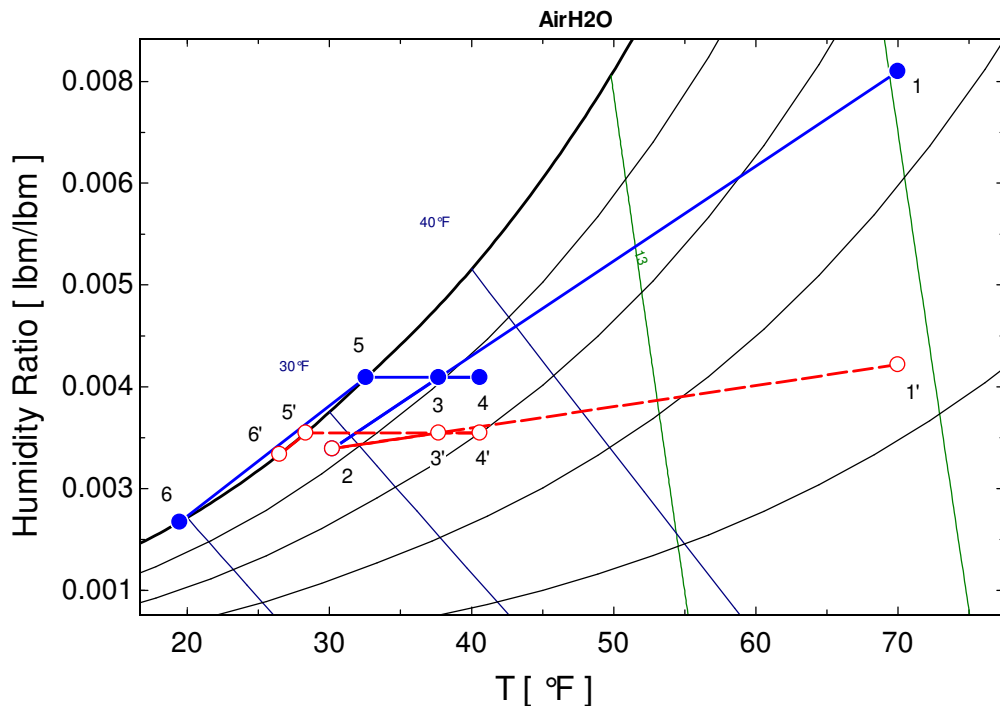
1	ambient air condition	2	outlet air condition from the cooling coil
3	air condition after the fan	4	inlet air condition to the cooling coil
5	saturation point	6	the condition of the air pass the coil
	RH = 49%		' -- RH = 26%

Figure 5.5 Cooling process analysis in the refrigeration coil

The bypass coefficient differed with ambient air conditions. As the room temperature and environment humidity changes with weather, time, it is hard to make an accurate prediction of state point 1. A rough estimation was made in the following analysis. The room temperature was assumed at 70 °F (21 °C), the relative humidity changed from 25% to 50%.
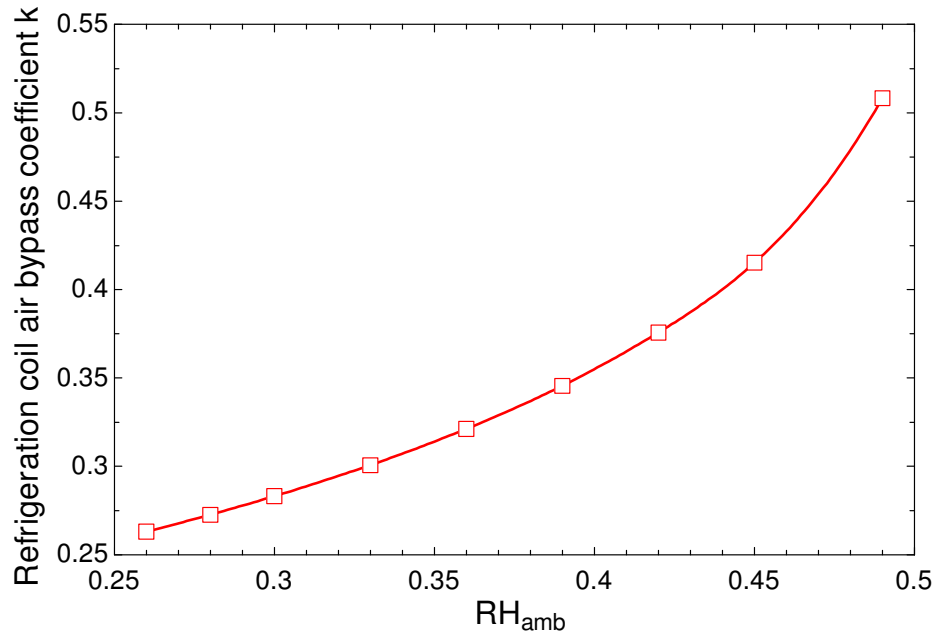
Figure 5.6   Analysis of the refrigeration coil air bypass coefficient

Figure 5.5 gives the processes under different environment relative humidity, and figure 5.6 shows how the bypass coefficient with different ambient condition. Under a certain room temperature, the bypass coefficient increases with higher relative humidity. Based on above assumption, the coefficient of the refrigeration coil changed from 0.25 to 0.5. The value was affected by both room temperature and relative humidity.

5.2   CALIBRATION

5.2.1   Thermocouple and RTD calibration

All the thermocouples and RTDs used in the experiment need to be calibrated separately. Immerse them in a constant bath temperature libratory device. With the bath temperature varied from -20 to 20 ºF, and compare with the result from Labview program. Every time increase the temperature 5 degree and remain the temperature sensors in the libratory device for one hour for the unit reaching a constant status. The process was repeated at different times before reaching a final calibrated equation.

5.2.2 Temperature distribution

The preliminary experiment gave the temperature distribution of two thermocouple grids. The grid configuration and the temperatures are shown in figures 5.7, 5.8.

The 3 x 3 (1ft x 1ft) grid was placed after the test section, before the flow nozzle, while the 4 x 4 (2ft x 2ft) grid was installed right after the re-heating coil. Observed from the data shown in Labview program, we can predict the 3 x 3 thermocouple grid had a more uniform temperature distribution. In the preliminary experiment, two channels that connected to point 26, 27 were changed to the two extra thermocouples mentioned above, measuring temperatures after the fan and before the cooling coil. From figure 5.8, the 3 x 3 grid had a maximum temperature difference of 0.26 ºF, while the 3 x 3 grid, the 4 x 4 grid gave a 3.76 ºF difference.
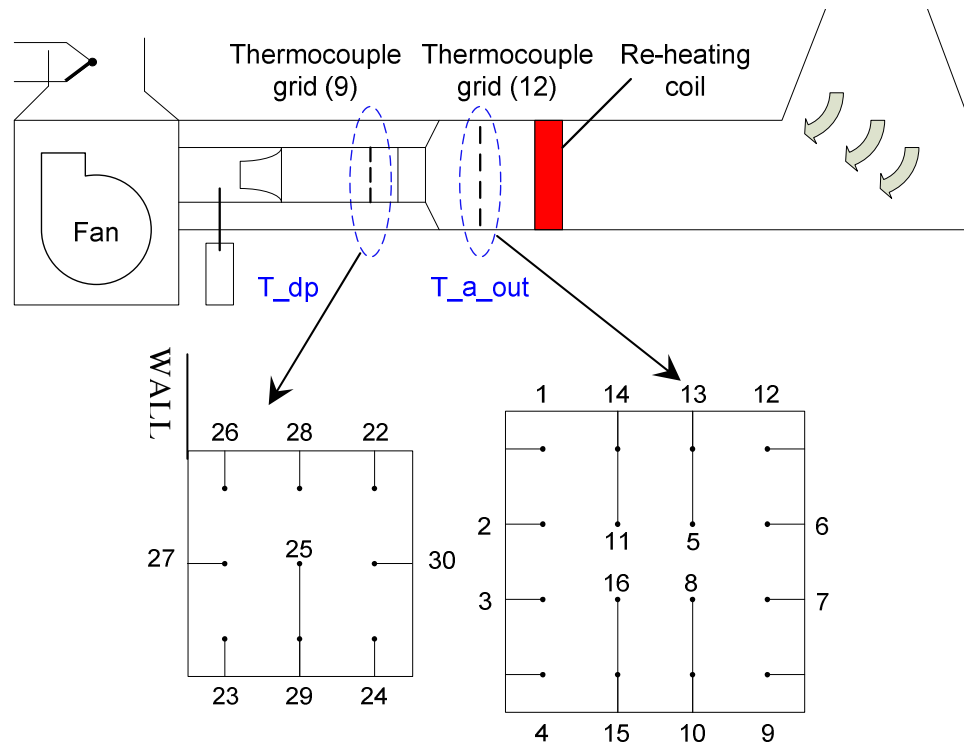

Figure 5.7 Thermocouple configuration

	30.10 (-1.06)	30.36 (-0.91)
	29.88 (-1.18)	30.00 (-1.12)
30.13 (-1.04)	30.26 (-1.00)	30.23 (-0.98)

32.46 (0.26)	31.10 (-0.50)	30.25 (-0.97)	30.08 (-1.07)
32.15 (0.09)	29.90 (-1.17)	29.24 (-1.53)	28.87 (-1.74)
32.12 (0.07)	28.86 (-1.74)	28.70 (-1.83)	29.11 (-1.61)
32.01 (0.01)	29.12 (-1.60)	28.98 (-1.68)	30.43 (-0.87)

Figure 5.8 Temperature distribution

Unit: ºF (ºC)

According to current design, three ways are recommended to impair non-uniform problem:

1. Change the fan with the one that can supply a higher flow rate. One of the possible reasons is the low flow rate resulting in stratification of the air stream before the thermocouple grid. Increasing total air flow rate should benefit temperature distribution. The cooling coil was designed with enough capacity to deal with high flow rate. The thermal guard duct also can perform better in high flow. According to Spencer's work, in the thermal guard duct, higher air flow leads to a smaller temperature change between the flow nozzle and the section right after the MCHX. However, in current apparatus, there was no damper system before the test section, which means, when the total air flow increases a lot, it would be hard to control the flow rate passing through the MCHX in an exact range of 200 to 400 cfm.

2. Decrease air loop pressure drop. The soft connection between the main supply and return loop led to a large pressure drop of about 1.5 inch wc in the wind tunnel. The solid line in figure 5.9 shows the soft connection on the second floor of the air flow lab. This high pressure drop seriously limited the system flow rate. Parallel branches design

117

should decrease total pressure drop by dividing the air flow in multiple ducts. Currently only one connection with a large diameter was installed to reduce the pressure drop in the air flow. Although this solve the problem and I was able to achieve about 360 cfm, it is recommended to use multiple duct in parallel in this section of the wind tunnel to reduce further pressure losses.
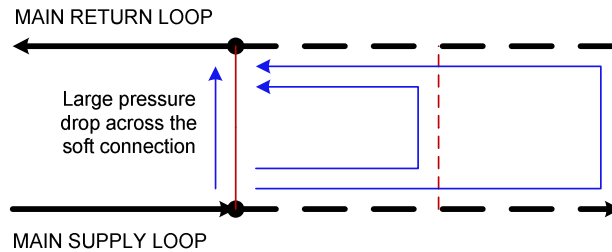
MAIN RETURN LOOP

Large pressure
drop across the
soft connection

MAIN SUPPLY LOOP

Figure 5.9 Parallel braches decreasing total pressure drop

3.   Decrease cross section area before the re-heating coil and build a thermal guard duct section before the test evaporator as indicated in the figure 5.10 below.

The re-heating coil should help improving temperature distribution in the air stream. It works as a straighter and a honeycomb mixer. The pressure drop across the heating coil decreases the air velocity and accelerates air mixing before the thermocouple grid. However, from the preliminary data, non-uniform temperature distribution is still recorded at the inlet thermocouple grid. That means a significant non-uniformity in the temperature distribution of the inlet air stream to the test evaporator occurs. As mentioned above, possible explanations of this non-uniform temperature distribution are the low velocity of the air and possible stratifications effect. Heat conduction effect via the duct wall in this section of the wind tunnel could also be another reation. Thus, two pieces of blue board can be used to block part of the space before the re-heating coil. Figure 5.10 demonstrates the way to decrease front area of the re-heating coil. Another

two pieces of blue board decrease the area after the re-heating coil. A smaller grid, which

is also fit in a 1ft x 1ft duct is installed just before the test evaporator as indicated in the
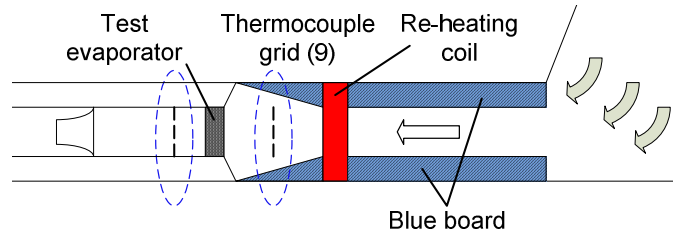
figure below.

Figure 5.10 Decrease section areas before the re-heating coil

    4.   Changing the material that supports the thermocouple grid and installation

method. The grid support was of Aluminum and it is attached to the frame of the duct. It

is possible that heat conduction effect through the grid support and thermocouple

insulation alters the thermocouple readings. Thus, the support of the grid was modified

from Aluminum to plastic to prevent heat conduction to the thermocouple tips. Using

thread at four corners and fixing the grid inside the duct, instead of mounting a metal

frame directly on the tunnel seems also a better way to reduce heat conduction effects and

improve the reliability of the thermocouple readings.

    The modifications proposed in the bullets 2, 3 and 4 above are easy to implement

in the air flow wind tunnel while the bullets 1 requires major modifications and expensive

equipment (i.e. purchase of a new fan). After the thermocouple grid support was well

insulated by using plastic and a thermal guard duct was installed at the inlet of the test

evaporator, the new temperature distribution of the air stream at the inlet of the test

evaporator should be better.

5.2.3 Frost accumulation on the refrigeration coil

Once the chiller runs at extremely low temperature, i.e. -28 ℉, for more than 20 hours, frost starts to accumulate in the refrigeration coil. With more frost growth on it, the air pass is blocked and cooling capacity hurts a lot. The air temperature increases significantly from 32 ℉ (0 ℃) to 48 ℉ (9 ℃) when running the system at -20 ℉ for more than 20 hours. This also affects the air distribution after the refrigeration coil. As the chiller temperature decreases, frost problem in the refrigeration coil is more severe. In order to run the facility 2 to 3 days without severe frost growth, an acceptable lowest chiller temperature needs to be found.

Another problem coming with the low chiller temperature is the flow rate. By decreasing the set point of the chiller, more flow will be bypassed to the evaporator, reducing the total flow rate coming out from the chiller. This is another reason that causes air temperature rising in the wind tunnel. Start from 20 ℉, adjusting the cooling valve manually to decrease the chiller temperature gradually and try to find a lowest practical temperature. With the balance between this temperature and the flow rate, frost in the refrigeration coil should not be that severe, and the output flow rate can meet capacity requirement for both refrigeration coil and plate heat exchanger at the same time.

5.2.4 Weighting mechanism

As shown in figure 3.32, a digital scale measures the weight of the test evaporator together with its frame and the fluid inside it, which flows at a certain flow rate. The scale is mounted above the wind tunnel and outside the tunnel. Thus, the scale is always at room temperature of about 77°F. This minimizes the thermal drift of electronics inside the digital scale. Because of the air circulates across the evaporator inside the tunnel, the readings from the digital scale do not represent the real weight of the test evaporator, but

rather a general value that include frame, fluid weight, pipe connection resistance, fin drag resistance, and hysteresis effects. A correction equation between the readings from the scale and the real weights needs to be found during the calibration of the weight mechanism device. In order to find this correction equation, 1g (0.035 o.z.), 7g (0.125 o.z.), 14g (0.25 o.z.), 28g (0.5 o.z.) and 56g (2 o.z.) weights were mounted gradually on the test heat exchanger and their weight was checked with the electronic scale while the tunnel was in operation. From the literature review, the frost nucleation process is reported as the key point for frost accumulation. So the calibration was focused on the weight up to 100g, artificially simulating the beginning part of frost formation. The weights were checked before calibration by using a high precision scale with an accuracy of ±0.0001g. However, the digital scale mounted on the wind tunnel has a precision within ±0.2g. Considering the linearity and hysteresis of the digital scale, the calibrated weights were added and removed to the test evaporator incrementally several times. Figures 5.11 and 5.12 show the correlations between the reading from the digital scale above the wind tunnel and the true weights applied to the test evaporator with the air flow rates at 250 cfm and 150 cfm in the tunnel. When the flow rate decreases from 250 cfm to 150 cfm, the correlations changed slightly when the weights were more than 4g, and the readings were within 15% error. When it was less than 4g, the readings changed from 30% to 125%. It is recommended to calculate the correction equation for the frost weight under different conditions if the air flow rate would change in a wider range.
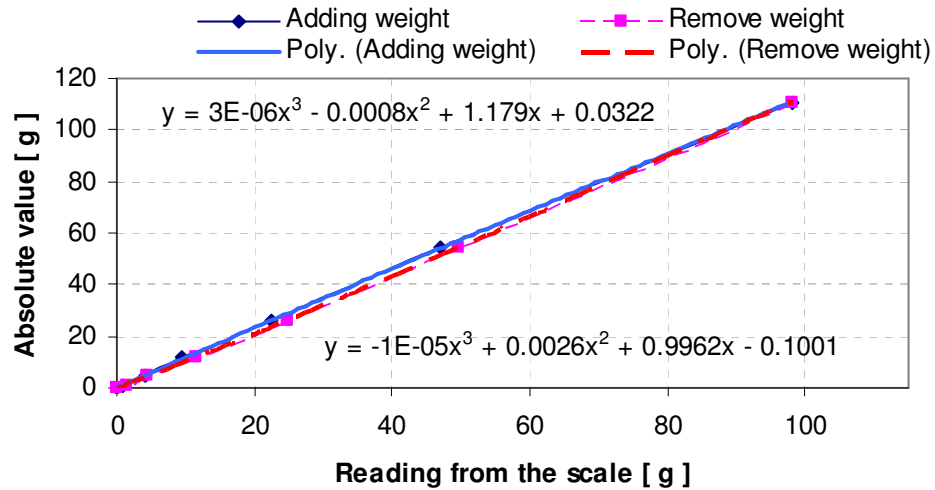
Figure 5.11 Calibration for weighting mechanism (250 cfm)

Figure 5.12 Calibration for weighting mechanism (150 cfm)

5.3 IMPROVED EXPERIMENT AND RESULTS AFTER CALIBRATION

Based on preliminary experiments, the current facility faced a serious uneven air temperature distribution at the inlet of the test evaporator.

In the previous chapter, the temperature differences between the thermocouples in the 4 x 4 (2ft x 2ft) was around 3.76 ºF. Four possible methods were proposed in

section5.3.2. To avoid major modification and expensive substitute equipment, the last three modifications were implement in the air flow wind tunnel.

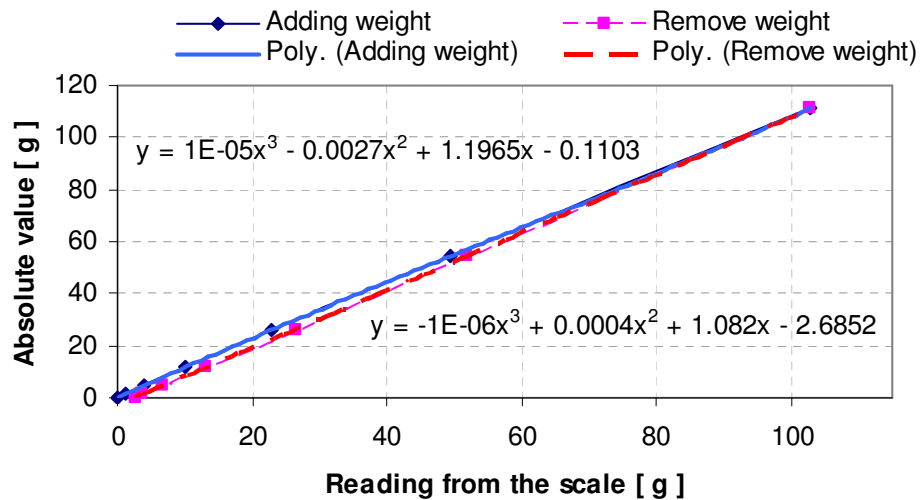A new 3 x 3 (1ft x 1ft) grid was made by using PVC instead of Aluminum. The grid was installed in a new designed thermal guard duct as shown in figure 5.13.
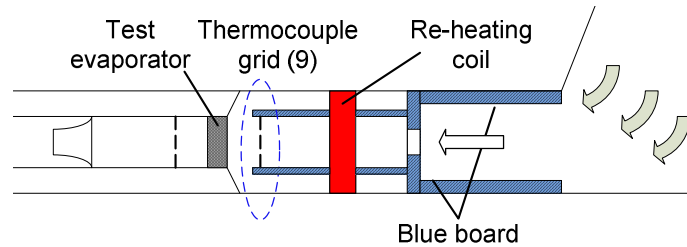
Figure 5.13   Improved thermocouple grid and thermal guard duct

One branch was added on the third level between the main air supply and retain loops as shown in figure 5.14. These soft connections were sealed well to decrease air leakage.
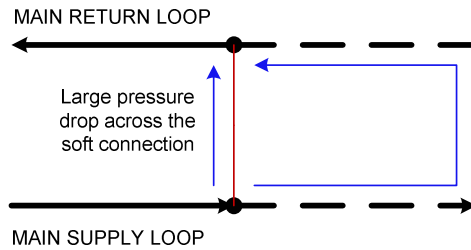
Figure 5.14   Parallel branch decreasing total pressure drop

Figure 5.15 gives the improved experimental results with the same conditions as described in section 5.2.2. The re-heating coil was off, and the set point of the chiller was 19 ºF (-7.2 ºC).

1	Inlet air temperature to the refrigeration cooling coil	2	Air temperature after the fan
3	Return temperature of fluid to the chiller	4	Outlet air temperature from the cooling coil
5	Dew point before the fan	6	Leaving temperature of the fluid from the chiller

Figure 5.15   Improved experimental results

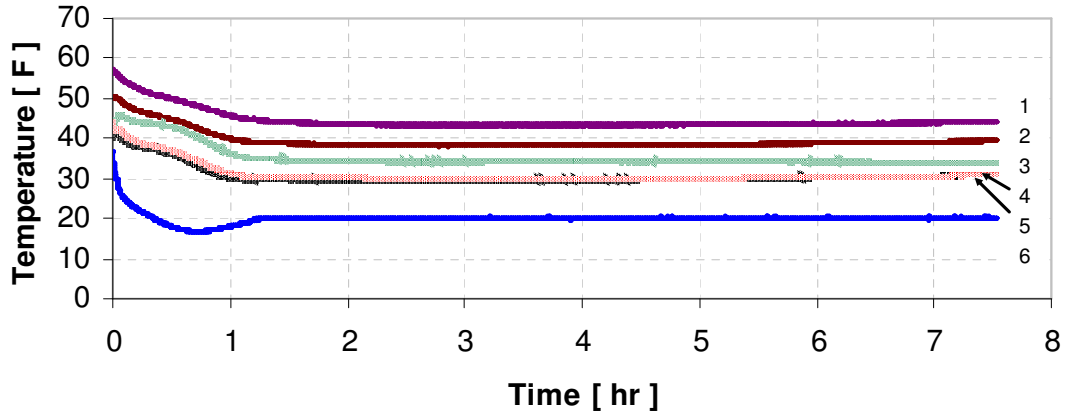Compared to figure 5.3, the valves in the loop to the plate frame heat exchanger were fully opened, thus, more flow goes to the plate frame heat exchanger and the refrigerant leaving temperature from the chiller is more stable and better controlled. At steady state conditions, the air and chiller refrigerant temperatures at the inlet and outlet of the refrigeration coil are summarized in table 5.2.

Table 5.2   Preliminary results

1	$T_{a,in} \approx 45.6$ ºF (6.4 ºC)	2	$T_{afterfan} \approx 38.6$ ºF (3.7 ºC)
3	$T_{ref,out} \approx 34.2$ ºF (1.2 ºC)	4	$T_{a,out} \approx 29.9$ ºF (-1.2 ºC)
5	$T_{dp} \approx 30.2$ ºF (-1.0 ºC)	6	$T_{ref,in} \approx 20.1$ ºF (-6.6 ºC)

The new temperature distribution of the air stream at the inlet of the test evaporator was recorded as shown in figure 5.16 below.

30.04 (-1.09)	29.53 (-1.37)	30.16 (-1.02)
30.44 (-0.87)	29.40 (-1.44)	30.11 (-1.05)
29.78 (-1.23)	29.04 (-1.64)	30.58 (-0.79)

Figure 5.16   New temperature distribution at the inlet of the test evaporator coil

Unit: ºF (ºC)

Compared to previous result, the temperature variation in the air stream before the test evaporator is within 1.5 ºF from the average value measured in the thermocouple grid, which means the modification on the thermocouple grid, thermal guard duct and bypass duct do help improving uniformity of the air flow.

Another issue was the frosting of the refrigeration coil in the wind tunnel. At 19 ºF inlet refrigerant temperature, the refrigeration does not have much frost on the surface and has enough capacity to cool down the air in the wind tunnel. In the test evaporator side, the inlet Ethylene Glycol temperature to the test section is around 23 ºF. Since the required refrigerant temperature for the test evaporator is 20 ºF, the chiller temperature should go further lower in the following tests. At about 8 to 10 ºF refrigerant inlet temperature, the frost build up on the refrigeration coil surface is quite significant and the refrigeration coil is able to operate continuously for only about 8 hours before defrost is required.

In order to check the nozzle and the uniformity of the air flow in the duct, the velocity distribution was also investigated. The measurements were taken place at two positions as shown in figure 5.17. The first measurement happened right after the

thermocouple grid, at the outlet of the re-heating coil. The other one was set at the inlet of the test evaporator.
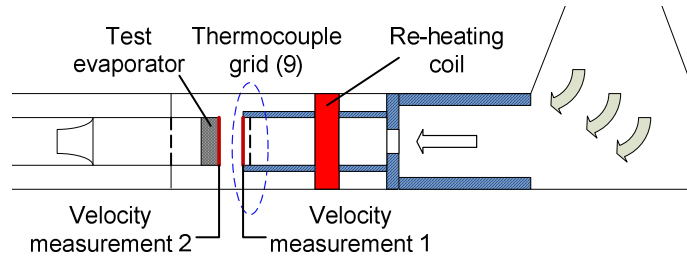
Figure 5.17 Measurement position for velocity distribution

Considering the measuring range of the air velocity transducer, which is 2.5m/s at maximum, the air flow rate through the nozzle was adjusted to 175 cfm. The results of the velocity distribution at two measurement positions are shown in figure 5.18.

217 (1.1)	492 (2.5)	472 (2.4)
98 (0.5)	354 (1.8)	295 (1.5)
138 (0.7)	276 (1.4)	256 (1.3)

177 (0.9)	236 (1.2)	348 (1.7)
177 (0.9)	197 (1.0)	295 (1.5)
177 (0.9)	197 (1.0)	256 (1.3)

a) Velocity measurement 1   b) Velocity measurement 2

Figure 5.18   Velocity distribution: ft/min (m/s)

Since there is no seal between the thermal guard duct and the wind tunnel, the air flow rate through the nozzle are not equal to the total air flow rate in the duct. Thus, the velocity at position 1 was higher than the result in position 2 because part of the air does not enter the inner duct.

According to the Labview program, the flow rate through the nozzle is 175 cfm, which means the average air velocity should be around 175 fpm in the 1ft x 1ft thermal guard duct. Figure 5.18 b) shows the velocity at the inlet to the 1ft x 1ft test evaporator.

From the velocity distribution, the average velocity is 228 fpm (1.16 m/s), which is 30% higher than the value measured by the flow nozzle. There are several possible reasons:

a) The air velocity transducer is an omni-directional instrument. As the flow is not that straight, the reading from the velocity transducer does not represent the real air velocity going into the inner duct;

b) The accuracy of the flow nozzle is ±2.2%, while the accuracy of the velocity transducer is ±3%.

c) The accuracy of the measurement would be better with more measuring points.

5.4 BIAS UNCERTAINTY

According to figure 5.16, although the temperature distributions were better than before, it is not ideally uniform. Due to the non-uniform distributions, besides precision uncertainty, bias uncertainty also needs to be considered. The bias uncertainty was computed according to the approach provided by Johnson et al. 1998 and summarized as below:

$$B_{Tdistribution} = \frac{T_{max} - T_{min}}{n} \qquad [5.1]$$

$$B_T = \sqrt{B_{Tdistribution}^2 + B_{Tuniform}^2} \qquad [5.2]$$

Where

T_{max} is the maximum temperature measured in the grid at the inlet of the test section

T_{min} is the minimum temperature measured in the grid at the inlet of the test section

$B_{Tdistribution}$ is the bias uncertainty resulting from a non-uniform temperature distribution

$B_{Tuniform}$ is the bias uncertainty present even with a uniform temperature distribution and it is estimated from equation 5.1 with T_{max} and T_{min} set as the acceptable limits for temperature uniformity condition.

B_T is the total bias uncertainty

n is the total number of measuring points in the grid.

In practice it is not feasible to achieve zero temperature difference between T_{max} and T_{min}. In the experiments, I decide that the condition of uniform temperature distribution is met if the temperature difference $(T_{max} - T_{min})$ is less than 0.5 ºF. In such case, $B_{Tuniform}$ results about 0.056 ºF while $B_{Tdistribution}$ from the data of figure 5.16 results much higher, that is, 0.17 ºF. Thus, the total bias uncertainty is estimated to be about 0.18 ºF, while the precision uncertainty was ± 0.2 ºF as described in previous chapter. Since the bias uncertainty is quite similar to the instrument uncertainty, by using either the total bias uncertainty or the instrument uncertainty as input values to my uncertainty model, the resulting uncertainties on U and h_{out} are very similar in both cases and around 1% lower if the total bias uncertainty is used. From this analysis it is concluded that the temperature mal-distribution measured with the grid at the inlet of the test section inside the wind tunnel is within satisfactory limits because even though it is not ideally uniform, its total bias uncertainty is still lower than the instrument uncertainty.

5.5 ENERGY BALABCE

The energy balance was checked by three methods. The total heat transfer was calculated in the air side, refrigerant side and from the frost accumulation. Since the test evaporator was tested under wet and frost condition, in the air side, the heat transfer is:

$$\dot{Q}_a = \dot{m}_a (h_{a,in} - h_{a,out})$$

[5.3]

The inlet and outlet enthalpies were estimated from inlet and outlet air dry-bulb temperatures and humidity ration, which were read from thermocouple grids and the dew point meters. The air flow rate was measured by the flow nozzle after the test evaporator. This method has a high requirement on the sealing and insulation around the wind tunnel. Any infiltration and heat transfer effect the humidity and temperature situation and results in large error.

In the refrigerant side, inlet and outlet fluid temperatures were measured by RTDs. The refrigerant flow rate was determined from the Coriolis flow meter. The heat transfer in the refrigerant side is:

$$\dot{Q}_{ref} = \dot{m}_{ref} (T_{ref,out} - T_{ref,in})$$

[5.4]

During frost formation, the latent heat of the air can be calculated from the frost side. The total heat loss in the air is:

$$\dot{Q}_f = \dot{m}_a \, c_P (T_{a,in} - T_{a,out}) + \dot{m}_f \, h_{SL}$$

[5.5]

Where h_{SL} represents the latent heat of submission, which is 2833 J/g. The frost flow rate was estimated from the precision scale.

Table 5.3 shows the air and refrigerant side conditions used for energy balance calculation. Three cases were selected from the experiment. The chilled mirror after the test evaporator always shows a higher humidity level, which is believed to be incorrect. The chilled mirror was also checked when the test evaporator was off. Humidity level still increase in the test section. Thus, I believe that there might be an air infiltration to the chill mirror probe downstream the test section and heat transfer occurs in the wind

tunnel. The facility should be better sealed and insulated in this section of the tunnel.

After insulated and sealed carefully, the two humidity sensor next to the test evaporator

still failed to give a consistent result, which means with current sealing and insulation,

there is an inevitable error. Since the error effects the calculation of the total heat transfer

in the air side, equation [5.3] will not be used for energy balance check. Table 5.4 gives

the result of the average heat transfer in the previous three cases. The results were in

25%.

Table 5.3   Air and refrigerant side conditions for energy balance

$T_{a,in}$	$\omega_{a,in}$	$T_{a,out}$	$\omega_{a,out}$	$\dot{m}_a$	$T_{ref,in}$	$T_{ref,out}$	$\dot{m}_{ref}$	$\dot{m}_f$
[F]	[lbm/lbm]	[F]	[lbm/lbm]	[lbm/min]	[F]	[F]	[lbm/min]	[lbm/min]
35.2	0.00357	32.8	-	21.52	19.6	20.2	43.65	0.0013
34.9	0.00357	32.6	-	21.6	19.7	20.2	43.65	0.001
34.8	0.00354	32.3	-	21.6	19.9	20.5	43.65	0.0009

Table 5.4   Energy balance

	Total heat transfer rate [W]	Energy balance
$\dot{Q}_{ref} = \dot{m}_{ref}(T_{ref,out} - T_{ref,in})$	248.1	
$\dot{Q}_f = \dot{m}_a c_P (T_{a,in} - T_{a,out}) + \dot{m}_f h_{SL}$	330.6	25%

CHAPTER VI

CONCLUSIONS AND RECOMMENDATIONS

6.1 CONCLUSIONS

An experimental methodology was developed to investigate the frost and defrost thermal

hydraulic performances of louvered folded fin microchannel heat exchangers under initial

cycle, defrost cycle and subsequent re-frost cycles. On the air side, the air flow rate was

supplied by a variable speed fan with automatic control. The required 35/33 ºF dry-/ wet-

bulb temperature is achieved by using a humidifier, a refrigeration coil, a re-heat coil and

a low temperature chiller, in which dynalene HC40 was used as heat transfer process

refrigerant. From preliminary experiment, without turning on the humidifier, the dry-bulb

temperature of the air can be reached by adjusting the set points of the chiller. In the

refrigerant side, the required 20 ºF refrigerant inlet temperature is obtained by using an

immersed electric heater. In the test coil loop, ethylene glycol was selected to be the

coolant. Preliminary experiment showed the test loop can run with any flow rate below 8

gpm by manually control the gear pump.

Compared to previous result, after calibration, the temperature variation in the air

stream before the test evaporator is within 1.5 ºF from the average value measured in the

thermocouple grid, which means the modification on the thermocouple grid, thermal

guard duct and bypass duct do help improving uniformity of the air flow.

Another issue was the frosting of the refrigeration coil in the wind tunnel. At 19 ºF inlet refrigerant temperature, the refrigeration does not have much frost on the surface and has enough capacity to cool down the air in the wind tunnel. In the test evaporator side, the inlet Ethylene Glycol temperature to the test section is around 23 ºF. Since the required refrigerant temperature for the test evaporator is 20 ºF, the chiller temperature should go further lower in the following tests. At about 8 to 10 ºF refrigerant inlet temperature, the frost build up on the refrigeration coil surface is quite significant and the refrigeration coil is able to operate continuously for only about 8 hours before defrost is required.

Additional experiment was provided by Ehsan Moallem, Ph.D. student at Oklahoma State University. In this experiment, the test evaporator was exposed to frosting conditions of 35/33 ºF dry-/wet-bulb temperature during the preliminary experiments. The ethylene glycol temperature entering the test evaporator was about 25 ºF and the flow rate was about 3.2 gpm. The temperature of dynalene HC coming from the chiller was 11 ºF. Approximately 30 grams of frost were built up on the surface of the test evaporator in 1 to 2 hours. The type of evaporator used in the preliminary experiments was fin-and-tube heat exchanger with 12 tubes circuited in parallel as described in section 4.2. This evaporator will be used as baseline heat exchanger the frost performance of microchannel heat exchangers will be compared to. Further experiments of frost growth on small scale heat exchangers are on-going in this facility but they are outside of the scope of this thesis. The preliminary data presented in this thesis show the functionality of the experimental facility for frost growth. The repeatability of the

measurements was also very good and the uncertainty of the test was found as described next.

6.1.2 Conclusions on the uncertainty of the heat transfer coefficient measurements

In the uncertainty analysis, the uncertainties on heat transfer coefficient (U) and air side heat transfer coefficient (h_{out}) are calculated for both 1 ft x 1 ft microchannel and finned tube heat exchangers. With the accuracy of current instrumentation, the uncertainty on U for microchannel heat exchanger is around ±7% in dry condition, ±10% for wet condition and ±15% for frost condition. The uncertainty on h_{out} is around ±2% higher than U. The recommended flow rate is 3 to 5 gpm for the refrigerant, and 400 to 600 cfm for the air. Refrigerant temperature differences should between 1.5 °F to 3 °F based on different conditions. Relevant air temperature decreases are expected to be in 5 °F to 8 °F.

Compared to microchannel heat exchanger, the fin-and-tube coil has a much higher uncertainty due to the smaller capacity. This low capacity gives smaller temperature differences for both refrigerant and air sides. Similar to the microchannel coil, recommended refrigerant flow rate is 3 to 5 gpm. For the air side, the flow rate should between 300 to 500 cfm.

Considering temperature differences in the thermocouple grid, bias uncertainty was also calculated. The bias uncertainty is 0.17 °F, while the precision uncertainty is ± 0.17 °F. Thus, the uncertainties on U and h_{out} based on both bias and precision uncertainties are pretty similar.

6.2 RECOMMENDATIONS FOR FUTURE WORK

1. Humidity control test. Current tests are only based on dry-bulb temperature control. In the next step, the humidifier should be on, the heating coil will also be connected in the loop. Humidity control needs to be carefully tested. If the system is lack of capacity to reach the desired humidity level, another humidifier needs to be installed before the refrigeration coil.

2. Lowest practical chiller temperature. From the manufacture date, the chiller temperature can go down to -28 ℉. Nevertheless, once the set point of the chiller is lowered to -28 ℉, the cooling valve is opened all the time and bypasses a large part of the refrigerant back to the evaporator. Thus, the leaving fluid flow rate from the chiller decreases a lot and can neither cool down the air temperature through the refrigeration coil, nor reduce ethylene glycol temperature in the compact temperature control unit, to the desired points. A practical lowest chiller temperature should be existed with the relevant flow rate to maintain the capacity of both refrigeration coil and plate frame heat exchanger. Start from 19 ℉, adjusting the cooling valve manually to decrease the temperature gradually and try to find the practical point.

3. Defrost cycle of the test evaporator. The defrost cycle needs to run with the hot tank.

4. Soft connection and insulation. In the current apparatus, the test evaporator frame is set close to the thermal guard duct without any connection between them. Although the system flow rate is extremely low and concentrated in the central part of the duct, it is recommended to put plastic film between test evaporator and the inner duct. By comparing the inlet temperature of ethylene glycol to the test evaporator with outlet

Dynalene temperature from the chiller, there was a 4 ºF difference, which means the heat gain from the environment increases the refrigerant temperature. It would be benefit if the pipelines are well insulated. With better insulated, the temperature of ethylene is more close to the chiller temperature and the chiller can be set at a higher temperature, which means an easier control between the set point and flow rate.

REFERENCES

Guo, X., Wang, C., Wang, W., & Chen, C. (2006). Numerical simulation and experimental verification on dynamic performance of air source heat pump under frosting conditions. *Hsi-An Chiao Tung Ta Hsueh/Journal of Xi'an Jiaotong University, 40*(5), 544-548.

Jhee, S., Lee, K.-S., & Kim, W.-S. (2002). Effect of surface treatments on the frosting/defrosting behavior of a fin-tube heat exchanger. *International Journal of Refrigeration, 25*(8), 1047-1053.

Johnson AB, Simonson CJ, Besant RW: Uncertainty analysis in the testing of air-to-air heat/energy exchangers installed in buildings, in, San Francisco, CA, USA1998, ASHRAE, 1998, pp. 1639-1650.

Kim, J.-H., & Groll, E. A. (2003). *Performance comparisons of a unitary split system using microchannel and fin-tube outdoor coils*, Kansas City, MO, United States.

Kim, M.-H., & Bullard, C. W. (2001). Development of a microchannel evaporator model for a CO2 air-conditioning system. *Energy, 26*(10), 931-948.

Kondepudi, S. N., & O'Neal, D. L. (1989). Effect of frost growth on the performance of louvered finned tube heat exchangers. *International Journal of Refrigeration, 12*(3), 151-158.

Lee, Y. B., & Ro, S. T. (2001). An experimental study of frost formation on a horizontal cylinder under cross flow. *International Journal of Refrigeration, 24*(6), 468-474.

Lee, Y. B., & Ro, S. T. (2002). Frost formation on a vertical plate in simultaneously developing flow. *Experimental Thermal and Fluid Science, 26*(8), 939-945.

Na, B., & Webb, R. L. (2004). Mass transfer on and within a frost layer. *International Journal of Heat and Mass Transfer, 47*(5), 899-911.

Ogawa, K., Tanaka, N., & Takeshita, M. (1993). *Performance improvement of plate fin-and-tube heat exchangers under frosting conditions*, Chicago, IL, USA.

Ohkubo, H. (2006). *Advance of study on frosting phenomenon*

Ostin, R., & Andersson, S. (1991). Frost growth parameters in a forced air stream. *International Journal of Heat and Mass Transfer, 34*(4-5), 1009-1017.

Padhmanabhan, S., Cremaschi,L., Fisher,D.E., &Knight,J. (2008). Comparison of frost and defrost performance between microchannel coil and fin-and-tube coil for pump systems. *International Refrigeration and Air Conditionong Conference at Purdue, July 14-17*, 2202-2207.

Peng, X., He, Z., Xing, Z., & Shu, P. (2003). Operating characteristics of an air-source heat pump under frosting/defrosting conditions. *Proceedings of the Institution of Mechanical Engineers, Part A: Journal of Power and Energy, 217*(6), 623-630.

Peng, X. F., & Peterson, G. P. (1996). Convective heat transfer and flow friction for water flow in microchannel structures. *International Journal of Heat and Mass Transfer, 39*(12), 2599-2608.

Seker, D., Karatas, H., & Egrican, N. (2004a). Frost formation on fin-and-tube heat exchangers. Part I - Modeling of frost formation on fin-and-tube heat exchangers. *International Journal of Refrigeration, 27*(4), 367-374.

Seker, D., Karatas, H., & Egrican, N. (2004b). Frost formation on fin-and-tube heat exchangers. Part II - Experimental investigation of frost formation on fin-and-tube heat exchangers. *International Journal of Refrigeration, 27*(4), 375-377.

Song, S., Bullard, C. W., & Hrnjak, P. S. (2002). *Frost deposition and refrigerant distribution in microchannel heat exchangers*, Honolulu, HI, United States.

Wang, C.-C., Chi, K.-Y., & Chang, C.-J. (2000). Heat transfer and friction characteristics of plain fin-and-tube heat exchangers, part II: Correlation. *International Journal of Heat and Mass Transfer, 43*(15), 2693-2700.

Wang, C.-C., Lin, Y.-T., & Lee, C.-J. (2000). Airside correlation for plain fin-and-tube heat exchangers in wet conditions. *International Journal of Heat and Mass Transfer, 43*(10), 1869-1872.

Watters, R. J., O'Neal, D. L., & Yang, J. (2001). *Effect of fin staging on frost/defrost performance of a two-row heat pump evaporator at standard test conditions*, Cincinnati, OH.

Xia, Y., Hrnjak, P. S., & Jacobi, A. M. (2005). *Air-side thermal-hydraulic performance of louvered-fin, flat-tube heat exchangers with sequential frost-growth cycles*, Orlando, FL, United States.

Xia, Y., Zhong, Y., Hrnjak, P. S., & Jacobi, A. M. (2006). Frost, defrost, and refrost and its impact on the air-side thermal-hydraulic performance of louvered-fin, flat-tube heat exchangers. *International Journal of Refrigeration, 29*(7), 1066-1079.

Yan, D., Xia, J., Liu, Y., Zhang, X. & Jiang, Y. (2005). Building environment design simulation and software DeST(9): simulation and analysis of cooling/heating plant (part 2).

Yan, W.-M., Li, H.-Y., & Tsay, Y.-L. (2005). Thermofluid characteristics of frosted finned-tube heat exchangers. *International Journal of Heat and Mass Transfer, 48*(15), 3073-3080.

Yan, W.-M., Li, H.-Y., Wu, Y.-J., Lin, J.-Y., & Chang, W.-R. (2003). Performance of finned tube heat exchangers operating under frosting conditions. *International Journal of Heat and Mass Transfer, 46*(5), 871-877.

APPENDICES

APPENDIX A: REFRIGERATION COIL MODEL

"Functions"

"description of EES function for effectiveness"

"epsilon:=HX('crossflow_one_unmixed',NTU,C_a,C_ref,'epsilon')"

Function EFF7(C_min,C_ref,C_a,epsilon,C_r,NTU,R)

If (R=1) Then

If (C_min=C_a) Then

epsilon:=(1/C_r)*(1-exp(-C_r*(1-exp(-NTU))))

Endif

If (C_min=C_ref) Then

epsilon:=1-exp(-(1-exp(NTU*C_r))/C_r)

Endif

Endif

If (R=2) Then

If (C_min=C_a) Then

k:=1-exp(-NTU/2)

epsilon:=(1/C_r)*(1-exp(-2*k*C_r)*(1+C_r*k^2)

Endif

If (C_min=C_ref) Then

k:=1-exp(-NTU*C_r/2)

epsilon:=1-exp(-2*k/C_r)*(1+k^2/C_r)

Endif

Endif

If (R=3) Then

If (C_min=C_a) Then

k:=1-exp(-NTU/3)

epsilon:=(1/C_r)*(1-exp(-3*k*C_r)*(1+C_r*k^2*(3-k)+3*C_r^2*k^4/2))

Endif

If (C_min=C_ref) Then

k:=1-exp(-NTU*C_r/3)

epsilon:=1-exp(-3*k/C_r)*(1+k^2*(3-k)/C_r+3*k^4/(2*C_r^2))

Endif

Endif

If (R=4) Then

If (C_min=C_a) Then

k:=1-exp(-NTU/4)

epsilon:=(1/C_r)*(1-exp(-4*k*C_r)*(1+C_r*k^2*(6-4*k+k^2)+4*C_r^2*k^4*(2-

k)+8*C_r^3*k^6/3))

Endif

If (C_min=C_ref) Then

k:=1-exp(-NTU*C_r/4)

epsilon:=1-exp(-4*k/C_r)*(1+k^2*(6-4*k+k^2)/C_r+4*k^4*(2-

k)/C_r^2+8*k^6/(3*C_r^3))

Endif

Endif

EFF7:=epsilon

End EFF7

"Function for refrigerant side heat transfer coefficient"

Procedure HFACTOR_in(D_in,k_ref,Re_ref,Pr_ref,L_ft:h_in)

"Shah and London: for laminar flow"

if (Re_ref<2000) Then

x:=Re_ref*Pr_ref*D_in/L_ft

if (x>33.3) Then

Nu_ref:=1.953*(Re_ref*Pr_ref*D_in/L_ft)^(1/3)

Else

Nu_ref:=4.364+0.0722*(Re_ref*Pr_ref*D_in/L_ft)

Endif

Else

"Mcquiston   2000<Re<10000?assume bulk temperature=wall temperature"

h_in:=1.86*(Re_ref*Pr_ref*D_in/L_ft)^(1/3)*k_ref/(D_in*convert(inch,ft))

Endif

h_in:= Nu_ref*k_ref/(D_in*convert(inch,ft))

End HFACTOR_in

"Function for air side heat transfer coefficient, Wang et al. [2000]"

Procedure HFACTOR_out(D_out,D_c,D_h,P_t,P_l,F_p,Re_a,Pr_a,R,c_p_a,G_c:h_out)

If (R=1) Then

P_1:=1.9-0.23*ln(Re_a)

P_2:=-0.236+0.126*ln(Re_a)

j:=0.108*Re_a^(-0.29)*(P_t/P_l)^P_1*(F_p/D_c)^(-1.084)*(F_p/D_h)^(-

0.786)*(F_p/P_t)^(P_2)

Else

P_3:=-0.361-0.042*R/ln(Re_a)+0.158*ln(R*(F_p/D_out)^0.41)

P_4:=-1.224-0.076*(P_l/D_h)^1.42/ln(Re_a)

P_5:=-0.083+0.058*R/ln(Re_a)

P_6:=-5.735+1.21*ln(Re_a/R)

j:=0.086*Re_a^P_3*R^P_4*(F_p/D_c)^P_5*(F_p/D_h)^P_6*(F_p/P_t)^(-0.93)

Endif

h_out:=j*(c_p_a*G_c)/Pr_a^(2/3)

End HFACTOR_out

Procedure HeaderLoss(N:k_header)

If (N=1) Then

k_header:=0

Else

k_header:=2*((N+N/2+N/4)*2.9+N/2*1.5)

Endif

End HeaderLoss

"Input file"

"Air and refrigerant side condition"

P_atm=1[atm]

Q_s=2000[cfm]   "Air flow rate, can be set as variables"

T_ref_in=-25[F]   "Refrigerant leaving temperature from the chiller"

Q_ref=4[GPM]   "Refrigerant flow rate, can be set as variables"

"Coil geometry"

k_material=k_('COPPER', T_ref_in)   "Tube material: Copper"

H_ft=48[inch]   "Coil height"

L_ft=48[inch]   "Coil length"

W_ft=7*R/4   "Coil depth"

D_in=0.375[inch]   "Tube inside diameter"

D_out=0.4[inch]   "Tube outside diameter"

delta_tube=(D_out-D_in)/2   "tube thickness"

delta_fin=0.0039[inch]   "fin thickness"

D_c=D_out   "Assume collar diameter is outside diameter"

FPI=12   "Fin density"

F_p=1/FPI   "Fin pitch"

N=1   "Circuits, can be set as variables"

R=1   "Row number, can be set as variables"

N_t=42   "Tube number in one row"

P_l=0.866   "Longitude pitch"

P_t=1   "Traverse pitch"

"Calculate heat transfer coefficients"

"1.Calculate Re number"

"a) Refrigerant side (inside the tube)"

"Refrigerant properties"

c_p_ref=0.67[Btu/(lbm-F)]   "Specific heat of Dynalene HC40"

rho_ref=83.65[lbm/ft^3]   "Density of Dynalene HC40"

mu_ref=9*convert(cp,lbm/(ft*h))   "Dynamic viscosity of Dynalene HC40"

k_ref=0.266[Btu/(h-ft-F)]   "Conductivity of Dynalene HC40"

Pr_ref=mu_ref*c_p_ref/k_ref

m_ref=Q_ref*convert(gpm,ft^3/h)*rho_ref

                             "Refrigerant mass flow rate"

v_ref=mu_ref/rho_ref   "Kinematic viscosity"

v_dot_ref=Q_ref*convert(gpm,ft^3/h)/(pi*D_in^2/4*convert(inch^2,ft^2)*N)

                             "Refrigerant velocity"

Re_ref=v_dot_ref*D_in*convert(inch,ft)/v_ref

T_ref_out=T_ref_in+deltaT_ref   "Refrigerant outlet temperature from the coil"

"b) Air side (outside the tube)"

k_a=Conductivity(AirH2O,T=35, B=33,P=P_atm)   "Conductivity of the air"

c_p_a=Cp(AirH2O,T=35, B=33,P=P_atm)   "Specific heat of the air"

mu_a=Viscosity(AirH2O,T=35, B=33,P=P_atm)   "Dynamic viscosity of the air"

v_a=mu_a/rho_a   "Kinematic viscosity of the air"

rho_a=Density(AirH2O,T=35, B=33,P=P_atm)   "Density of the air"

m_a=rho_a*Q_s*convert(cfm,ft^3/h)   "Mass flow rate of the air"

v_dot_a=Q_s*convert(cfm,ft^3/h)/((L_ft-FPI*L_ft*delta_fin)*(H_ft-

N_t*D_out)*convert(inch^2,ft^2))   "Air velocity"

Re_a=v_dot_a*D_c*convert(inch,ft)/v_a

Pr_a=mu_a*c_p_a/k_a

G_c=m_a/((L_ft-FPI*L_ft*delta_fin)*(H_ft-N_t*D_out)*convert(inch^2,ft^2))

                              "Mass flux evaluated at the minimum flow area"

D_h=4*W_ft*(L_ft-FPI*L_ft*delta_fin)*(H_ft-N_t*D_out)*convert(inch^2,ft^2)/A_out

"Outlet air conditions from the refrigeration coil"

omega_a_out=HumRat(AirH2O,t=T_a_out,r=1,P=P_atm)

T_a_wb_out=WetBulb(AirH2O,t=T_a_out,r=1,P=P_atm)

h_a_out=Enthalpy(AirH2O,t=T_a_out,r=1,P=P_atm)

"Inlet air conditions to the refrigeration coil"

T_a_in=50

h_a_in=Enthalpy(AirH2O,w=0.0035,T=T_a_in,P=P_atm)

T_a_wb_in=WetBulb(AirH2O,w=0.0035,T=T_a_in,P=P_atm)

"2.Transport coefficient inside and outside tubes"

"a) inside coefficient in laminar"

h_in_w=h_in*convert(Btu/hr-ft^2-F,w/m^2-C)

CALL HFACTOR_in(D_in,k_ref,Re_ref,Pr_ref,L_ft:h_in)

"b) outside coefficient in laminar"

j=19.36*Re_a^J_1*(F_p/D_c)^1.352*(P_l/P_t)^0.6795*R^(-1.291)

J_1=0.3745-1.554*(F_p/D_c)^0.24*(P_l/P_t)^0.12*R^(-0.19)

j=h_out/(c_p_a*G_c)*Pr_a^(2/3)

"3. Total heat transfer coefficient U and resistances"

"NTU Method"

Q_dot=epsilon*C_min*(T_a_wb_in-T_ref_in)   "Total heat transfer rate"

C_min=min(C_ref,C_a)

C_max=max(C_ref,C_a)

C_r=C_min/C_max

C_ref=m_ref*c_p_ref

C_a=m_a*c_pf_a

c_pf_a=(h_a_in-h_a_out)/(T_a_wb_in-T_a_wb_out)

epsilon=HX('crossflow_one_unmixed',NTU,C_a,C_ref,'epsilon')

NTU=U*A_out/C_min

R_in=1/(h_in*A_in/N)

R_material=(ln(D_out/D_in))/(2*pi*k_material*L_ft*N_t*R/N*convert(inch,ft))

R_out=1/(h_out*A_out*eta_surf/N)

"1/(U*A_out)=1/(h_in*A_in)+(ln(D_out/D_in))/(2*pi*k_material*L_ft*N_t/N*R*convert(inch,ft))+1/(h_out*A_out*eta_surf)"

eta_surf=0.9   "Surface efficiency"

A_in=N_t*R*L_ft*pi*D_in*convert(inch^2,ft^2)   "Inside surface area"

A_out=(N_t*R*(L_ft-delta_fin*L_ft*FPI)*pi*D_out+W_ft*H_ft*L_ft*FPI*2-

2*pi*D_out^2/4*L_ft*FPI*N_t*R)*CONVERT(INCH^2,FT^2)

                                                      "Total surface area"

"Energy balance"

Q_dot=C_ref*deltaT_ref   "Refrigerant side"

Q_dot=m_a*(h_a_in-h_a_out)   "Air side"

"Pressure drop across the refrigeration coil"

"Major Pressure Drop"

f= MoodyChart(Re_ref, 0.01)   "to be decided by using moody chart"

g_c_gravity=1

P_major=rho_ref*convert(lbm/ft^3,kg/m^3)*f*l_ft*convert(inch,m)*N_t/N*R*(v_dot_re

f*convert(ft/h,m/s))^2/(2*g_c_gravity*D_in*convert(inch,m))*convert(pa,psi)

"Minor Pressure Drop"

CALL HeaderLoss(N:k_header)

k_minor=1.5*(N_t/N-1)*R+k_header   "N-1 threaded 180deg return bends:1.5"

P_minor=k_minor*rho_ref*convert(lbm/ft^3,kg/m^3)*(v_dot_ref*convert(ft/h,m/s))^2/(

2*g_c_gravity)*convert(pa,psi)

P_tot=(P_major+P_minor)

APPENDIX B: TEST MICROCHANNEL COIL MODEL UNDER DRY, WET AND FROST CONDITIONS

"Input file"

"Air side conditions"

P_atm=1[atm]

Q_s=400[cfm]

v_dot_a=Q_s*convert(cfm,ft^3/h)/(((L_tube*FPI-1)*(R -

1))*(H_fin*F_p*convert(inch^2,ft^2)))

T_a_in=35[F]

T_a_wb_in=33[F]

T_a_db_in=30.25[F]

T_a_out=T_a_in-deltaT_a

RH_a_in=0.82

"Refrigerant side conditions"

T_ref_in=20[F]

T_ref_out=T_ref_in+deltaT_ref

Q_ref=8[GPM]

"Microchannel coil geometry"

k_material=k_('Aluminum', T_ref_in)

H_mc=1[ft]   "Coil height"

W_mc=1[ft]   "Coil width"

H_port=0.02[inch]   "Port height"

W_port=0.03[inch]   "Port wodth"

W_c=W_tube/N   "Center to center distance"

A_port=H_port*W_port   "Port area"

D_in=2*A_port/(H_port+W_port)   "Correspond inside diameter"

W_tube=0.7[inch]   "Tube width=Tube depth, assume Tube depth = Flow depth"

delta_tube=0.05[inch]   "Tube thickness"

L_tube=12[inch]   "Tube length"

SP_tube=0.5 [inch]   "Tube spacing=Tube pitch"

FPI=17   "Fin density"

L_fin=L_tube*FPI*SP_tube   "Fin length"

H_fin=sp_tube-delta_tube   "Fin height=Tube spacing - Tube thickness"

F_p=1/FPI   "Fin pitch"

delta_f=0.1*convert(mm,inch)   "Fin thickness"

L_p=0.06[inch]   "Louver pitch"

L_l=0.37[inch]   "Louver length"

L_alpha=27   "Louver angle"

N=23   "Number of ports"

R=W_mc*convert(ft,inch)/SP_tube+1   "Number of tubes"

"Calculate heat transfer coefficients"

"1.Calculate Re number"

"a) Refrigerant side (inside the tube)"

"Refrigerant properties"

c_p_ref=0.76[Btu/lbm-F]   "Specific heat of Ethylene Glycol"

rho_ref=68.05 [lbm/ft^3]   "Density of Ethylene Glycol"

mu_ref=12*convert(cp,lbm/(ft*h))   "Dynamic viscosity of Ethylene Glycol"

k_ref=0.2398[Btu/h-ft-F]   "Conducticity of Ethylene Glycol"

Pr_ref=mu_ref*c_p_ref/k_ref

m_ref=Q_ref*convert(gpm,ft^3/h)*rho_ref

"Mass flow rate of Ethylene Glycol"

v_ref=mu_ref/rho_ref   "Kinematic viscosity of Ethylene Glycol"

v_dot_ref=Q_ref*convert(gpm,ft^3/h)/(A_port*convert(inch^2,ft^2)*R*N)

"Velocity of Ethylene Glycol"

Re_ref=v_dot_ref*D_in*convert(inch,ft)/v_ref

"b) Air side (outside the tube)"

k_a=Conductivity(AirH2O,T=T_a_in,D=T_a_db_in,P=P_atm)

"Conductivity of the air"

c_p_a=Cp(AirH2O,T=T_a_in,D=T_a_db_in,P=P_atm)

"Specific heat of the air"

mu_a=Viscosity(AirH2O,T=T_a_in,D=T_a_db_in,P=P_atm)

"Dynamic viscosity of the air"

v_a=mu_a/rho_a   "Kinamatic viscosity of the air"

rho_a=Density(AirH2O,T=T_a_in,D=T_a_db_in,P=P_atm)

"Density of the air"

m_a=rho_a*Q_s*convert(cfm,ft^3/h)   "Air mass flow rate"

Re_a=v_dot_a*L_p*convert(inch,ft)/v_a

Pr_a=mu_a*c_p_a/k_a

"2.Transport coefficient inside and outside tubes"

"---DRY CONDITION------------------------------------"

"a) inside coefficient in laminar:X.F.Peng [1995]"

Nu_ref=h_in*D_in*convert(inch,ft)/k_ref

Nu_ref=0.1165*(D_in/(W_c))^0.81*(H_port/W_port)^(-0.79)*Re_ref^0.62*Pr_ref^(1/3)

"b) outside coefficient in laminar: Man-Hoe Kim[2000], Jacobi[2005]"

j=Re_a^(-0.487)*(L_alpha/90)^0.257*(F_p/L_p)^(-0.13)*(H_fin/L_p)^(-

0.29)*(W_tube/L_p)^(-0.235)*(L_l/L_p)^0.68*(SP_tube/L_p)^(-0.279)*(delta_f/L_p)^(-

0.05)

j=h_out/(rho_a*v_dot_a*c_p_a)*Pr_a^(2/3)

"--------------------------------WET AND FROST CONDITION----------------------------"

"a) inside coefficient in laminar: X.F.Peng [1995]"

Nu_ref=h_in*D_in*convert(inch,ft)/k_ref

Nu_ref=0.1165*(D_in/(W_tube/N))^0.81*(H_port/W_port)^(-

0.79)*Re_ref^0.62*Pr_ref^(1/3)

h_in_w=h_in*convert(Btu/hr-ft^2-F,w/m^2-C)

"b) outside coefficient in laminar :Man-Hoe Kim[2000], "

j=Re_a^(-0.512)*(L_alpha/90)^0.25*(F_p/L_p)^(-0.171)*(H_fin/L_p)^(-0.29)*(W_tube/L_p)^(-0.248)*(L_l/L_p)^0.68*(SP_tube/L_p)^(-0.275)*(delta_f/L_p)^(-0.05)

j=h_out/(rho_a*v_dot_a*c_p_a)*Pr_a^(2/3)

 "3. Total heat transfer coefficient and resistances"

R_in=1/(h_in*A_in)

R_material=(delta_tube*convert(inch,ft))/(k_material*A_in)

R_out=1/(h_out*A_out*eta_surf)

R_tot=1/(U*A_out)

R_tot=R_in+R_material+R_out

"1/(U*A_out/R)=1/(h_in*A_in/R)+(delta_tube*convert(inch,ft))/(k_material*A_in/R)+1/(h_out*A_out/R*eta_surf)"

"In frost condition, the resistance of frost needs to be considered:"

"Frost accumulation

delta_frost=0.08[inch]   "Frost thickness (on fin and tubes)"

m_frost=0.7[lbm]   "Mass of frost"

rho_frost=m_frost/(delta_frost*convert(inch,ft)*A_out)

"Frost thermal conductivity: Lee et al.[2003], 50 ≤ frost density ≤ 400kg/m^3"

k_frost=0.132+3.13*10^(-4)*rho_frost+1.6*10^(-7)*rho_frost

R_frost=delta_frost*convert(inch,ft)/(k_frost*A_out)

R_tot=R_in+R_material+R_frost+R_out

"1/(U*A_out)=1/(h_in*A_in)+(delta_tube*convert(inch,ft))/(k_material*A_in)+(delta_fr

ost*convert(inch,ft)/(k_frost*A_out))+1/(h_out*A_out*eta_surf)"

eta_surf=0.9

A_in=(H_port+W_port)*2*l_tube*convert(inch^2,ft^2)*R*N

A_out=(w_tube+delta_tube)*2*L_tube*R*convert(inch^2,ft^2)+2*(R-

1)*H_fin*L_fin/cos(L_alpha)*convert(inch^2,ft^2)

"--DRY CONDITION--"

"LMTD Method: This method will be used with known inlet and outlet temperatures for

both air and refrigerant sides"

Q_dot=U*A_OUT*LMTD

LMTD=((T_a_in-T_ref_out)-(T_a_out-T_ref_in))/ln((T_a_in-T_ref_out)/(T_a_out-

T_ref_in))

"NTU Method: This method will be used with inlet temperatures of both air and

refrigerant sides"

Q_dot=epsilon*C_min*(T_a_in-T_ref_in)

C_min=min(C_ref,C_a)

C_max=max(C_ref,C_a)

C_r=C_min/C_max

C_ref=m_ref*c_p_ref

C_a=m_a*c_p_a

epsilon=HX('crossflow_one_unmixed',NTU,C_a,C_ref,'epsilon')

NTU=U*A_out/C_min

"Energy balance"

Q_dot=C_ref*deltaT_ref

Q_dot=C_a*deltaT_a

"Use the following equations for uncertainty analysis"

{Q_dot_ref=C_ref*deltaT_ref

Q_dot_a=C_a*deltaT_a

Q_dot=(Q_dot_a+Q_dot_ref)/2}

"---------------------------------WET AND FROST CONDITIONS--------------------------"

"LMED Method: This method will be used with known inlet and outlet temperatures for
both air and refrigerant sides"

Q_dot=U*A_out*LMED

LMED=((h_a_in-h_ref_out)-(h_a_out-h_ref_in))/ln((h_a_in-h_ref_out)/(h_a_out-
h_ref_in))

"Use trendline equation to calculated enthalpy"

T_ref_in_si=ConvertTemp(F,C,T_ref_in)

T_ref_out_si=ConvertTemp(F,C,T_ref_out)

"The function of the enthalpy is:

Function H_ref(T)

H_ref:=3.56*T-38

End"

h_ref_in_si=H_ref(T_ref_in_si)

h_ref_in=h_ref_in_si*convert(kJ/kg,Btu/lbm)

h_ref_out_si=H_ref(T_ref_out_si)

h_ref_out=h_ref_out_si*convert(kJ/kg,Btu/lbm)

"NTU Method: This method will be used with inlet temperatures of both air and refrigerant sides"

C_min=min(C_ref,C_a)

C_max=max(C_ref,C_a)

C_r=C_min/C_max

C_ref=m_ref*c_p_ref

C_a=m_a*c_pf_a

epsilon=HX('crossflow_one_unmixed',NTU,C_a,C_ref,'epsilon')

NTU=U*A_out/C_min

{T_a_out=T_ref_in}

"This can be used as initial guess when the program can not converge"

c_pf_a=(h_a_in-h_a_out)/(T_a_wb_in-T_a_wb_out)

T_a_wb_out=WetBulb(AirH2O,T=T_a_out,r=1,P=P_atm)

T_a_out=Temperature(AirH2O,h=h_a_out,r=1,P=P_atm)

"Energy balance"

Q_dot=C_ref*deltaT_ref

Q_dot= m_a*(h_a_in-h_a_out)

"Use the following equations for uncertainty analysis"

{Q_dot_ref=C_ref*deltaT_ref

Q_dot_a=m_a*(h_a_in-h_a_out)

Q_dot=(Q_dot_a+Q_dot_ref)/2}

APPENDIX C: TEST FIN-AND-TUBE COIL MODEL UNDER DRY, WET AND FROST CONDITIONS

"Functions:"

"Refrigerant side heat transfer coefficient"

Procedure HFACTOR_in(D_in,k_ref,Re_ref,Pr_ref,L_ft:h_in)

"Shah and London: for laminar flow"

if (Re_ref<2000) Then

x:=Re_ref*Pr_ref*D_in/L_ft

if (x>33.3) Then

Nu_ref:=1.953*(Re_ref*Pr_ref*D_in/L_ft)^(1/3)

Else

Nu_ref:=4.364+0.0722*(Re_ref*Pr_ref*D_in/L_ft)

Endif

Else

"Mcquiston 2000<Re<10000,assume bulk temperature=wall temperature"

h_in:=1.86*(Re_ref*Pr_ref*D_in/L_ft)^(1/3)*k_ref/(D_in*convert(inch,ft))

Endif

h_in:= Nu_ref*k_ref/(D_in*convert(inch,ft))

End HFACTOR_in

"Air side heat transfer coefficient in dry condition"

Procedure HFACTOR_out(D_out,D_c,D_h,P_t,P_l,F_p,Re_a,Pr_a,R,c_p_a,G_c:h_out,j)

If (R=1) Then

P_1:=1.9-0.23*ln(Re_a)

P_2:=-0.236+0.126*ln(Re_a)

j:=0.108*Re_a^(-0.29)*(P_t/P_l)^P_1*(F_p/D_c)^(-1.084)*(F_p/D_h)^(-

0.786)*(F_p/P_t)^(P_2)

Else

P_3:=-0.361-0.042*R/ln(Re_a)+0.158*ln(R*(F_p/D_out)^0.41)

P_4:=-1.224-0.076*(P_l/D_h)^1.42/ln(Re_a)

P_5:=-0.083+0.058*R/ln(Re_a)

P_6:=-5.735+1.21*ln(Re_a/R)

j:=0.086*Re_a^P_3*R^P_4*(F_p/D_c)^P_5*(F_p/D_h)^P_6*(F_p/P_t)^(-0.93)

Endif

h_out:=j*(c_p_a*G_c)/Pr_a^(2/3)

End HFACTOR_out

"Input file"

"Air side conditions"

P_atm=1[atm]

Q_s=400[cfm]

v_dot_a=Q_s*convert(cfm,ft^3/h)/((N_t*L_ft*P_t*convert(inch^2,ft^2)))

T_a_in=35[F]

T_a_wb_in=33[F]

T_a_db_in=30.25[F]

T_a_out=T_a_in-deltaT_a

RH_a_in=0.82

"Refrigerant side conditions"

T_ref_in=20[F]

T_ref_out=T_ref_in+deltaT_ref

Q_ref=8[GPM]

"Microchannel coil geometry"

k_material=k_('Aluminum', T_ref_in)

H_ft=12[inch]   "Coil height"

L_ft=12[inch]   "Coil length"

W_ft=1[inch]   "Coil depth"

D_in=0.381[inch]   "Tube inside diameter"

D_out=0.405[inch]   "Tube outside diameter"

delta_tube=(D_out-D_in)/2   "Tube thickness"

delta_fin=0.0039[inch]   "Fin thickness"

D_c=D_out+2*delta_fin   "Collar diameter"

FPI=18   "Fin density"

F_p=1/FPI   "Fin pitch"

delta_f=0.0039   "Fin thickness"

P_l=0.866   "Row pitch"

P_t=1   "Tube pitch"

N=12   "Number of circuits"

N_t=12   "Number of tubes per row"

R=1   "Number of rows"

"Calculate heat transfer coefficients"

"1.Calculate Re number"

"a) Refrigerant side (inside the tube)"

"Refrigerant properties"

c_p_ref=0.76[Btu/lbm-F]   "Specific heat of Ethylene Glycol"

rho_ref=68.05 [lbm/ft^3]   "Density of Ethylene Glycol"

mu_ref=12*convert(cp,lbm/(ft*h))   "Dynamic viscosity of Ethylene Glycol"

k_ref=0.2398[Btu/h-ft-F]   "Conducticity of Ethylene Glycol"

Pr_ref=mu_ref*c_p_ref/k_ref

m_ref=Q_ref*convert(gpm,ft^3/h)*rho_ref

                                           "Mass flow rate of Ethylene Glycol"

v_ref=mu_ref/rho_ref   "Kinematic viscosity of Ethylene Glycol"

v_dot_ref=Q_ref*convert(gpm,ft^3/h)/(A_port*convert(inch^2,ft^2)*R*N)

                                           "Velocity of Ethylene Glycol"

Re_ref=v_dot_ref*D_in*convert(inch,ft)/v_ref

"b) Air side (outside the tube)"

k_a=Conductivity(AirH2O,T=T_a_in,D=T_a_db_in,P=P_atm)

                                           "Conductivity of the air"

c_p_a=Cp(AirH2O,T=T_a_in,D=T_a_db_in,P=P_atm)

                                           "Specific heat of the air"

mu_a=Viscosity(AirH2O,T=T_a_in,D=T_a_db_in,P=P_atm)

                                           "Dynamic viscosity of the air"

v_a=mu_a/rho_a   "Kinamatic viscosity of the air"

rho_a=Density(AirH2O,T=T_a_in,D=T_a_db_in,P=P_atm)

                    "Density of the air"

m_a=rho_a*Q_s*convert(cfm,ft^3/h)   "Air mass flow rate"

Re_a=v_dot_a*L_p*convert(inch,ft)/v_a

Pr_a=mu_a*c_p_a/k_a

G_c=m_a/((L_ft-FPI*L_ft*delta_fin)*(H_ft-N_t*D_out)*convert(inch^2,ft^2))

                    "Mass flux evaluated at the minimum flow area"

D_h=4*W_ft*(L_ft-FPI*L_ft*delta_fin)*(H_ft-N_t*D_out)*convert(inch^2,ft^2)/A_out

"2.Transport coefficient inside and outside tubes"

"--DRY CONDITION--"

"a) inside coefficient in laminar"

"Shah and London"

CALL HFACTOR_in(D_in,k_ref,Re_ref,Pr_ref,L_ft:h_in)

 "b) outside coefficient in laminar"

Call HFACTOR_out(D_out,D_c,D_h,P_t,P_l,F_p,Re_a,Pr_a,R,c_p_a,G_c:h_out,j)

"------------------------------WET AND FROST CONDITIONS----------------------------"

"a) inside coefficient in laminar"

CALL HFACTOR_in(D_in,k_ref,Re_ref,Pr_ref,L_ft:h_in)

"b) outside coefficient in laminar"

j=19.36*Re_a^J_1*(F_p/D_c)^1.352*(P_l/P_t)^0.6795*R^(-1.291)

J_1=0.3745-1.554*(F_p/D_c)^0.24*(P_l/P_t)^0.12*R^(-0.19)

j=h_out/(c_p_a*G_c)*Pr_a^(2/3)

"3. Total heat transfer coefficient and resistances"

R_in=1/(h_in*A_in)

R_material=(ln(D_out/D_in))/(2*pi*k_material*L_ft*N_t/N*R*convert(inch,ft))

R_out=1/(h_out*A_out*eta_surf)

R_tot=1/(U*A_out)

R_tot=R_in+R_material+R_out

{1/(U*A_out)=1/(h_in*A_in)+(ln(D_out/D_in))/(2*pi*k_material*L_ft*convert(inch,ft))

+1/(h_out*A_out*eta_surf)}

"In frost condition, the resistance of frost needs to be considered:"

"Frost accumulation

delta_frost=0.08[inch]   "Frost thickness (on fin and tubes)"

m_frost=0.7[lbm]   "Mass of frost"

rho_frost=m_frost/(delta_frost*convert(inch,ft)*A_out)

"Frost thermal conductivity: Lee et al.[2003], 50 ≤ frost density ≤ 400kg/m^3"

k_frost=0.132+3.13*10^(-4)*rho_frost+1.6*10^(-7)*rho_frost

R_frost=delta_frost*convert(inch,ft)/(k_frost*A_out)

R_tot=R_in+R_material+R_frost+R_out

"1/(U*A_out)=1/(h_in*A_in)+(delta_tube*convert(inch,ft))/(k_material*A_in)+(delta_fr

ost*convert(inch,ft)/(k_frost*A_out))+1/(h_out*A_out*eta_surf)"

eta_surf=0.9

A_in=L_ft*pi*D_in*N*convert(inch^2,ft^2)

A_out=(N_t*R*(L_ft-delta_fin*L_ft*FPI)*pi*D_out+W_ft*H_ft*L_ft*FPI*2-

2*pi*D_out^2/4*L_ft*FPI*N_t*R)*CONVERT(INCH^2,FT^2)

"--DRY CONDITION--"

"LMTD Method: This method will be used with known inlet and outlet temperatures for

both air and refrigerant sides"

Q_dot=U*A_out*LMTD

LMTD=((T_a_in_R-T_ref_out_R)-(T_a_out_R-T_ref_in_R))/ln((T_a_in_R-

T_ref_out_R)/(T_a_out_R-T_ref_in_R))

"NTU Method: This method will be used with inlet temperatures of both air and

refrigerant sides"

epsilon=HX('crossflow_one_unmixed',NTU,C_a,C_ref,'epsilon')

C_min=min(C_ref,C_a)

C_max=max(C_ref,C_a)

C_r=C_min/C_max

C_ref=m_ref*c_p_ref

C_a=m_a*c_p_a

NTU=U*A_out/C_min

Q_dot=epsilon*C_min*(T_a_in-T_ref_in)

"Energy balance"

Q_dot=C_ref*deltaT_ref

Q_dot=C_a*deltaT_a

"Use the following equations for uncertainty analysis"

{Q_dot_ref=C_ref*deltaT_ref

Q_dot_a=C_a*deltaT_a

Q_dot=(Q_dot_a+Q_dot_ref)/2}

"--------------------------------WET AND FROST CONDITIONS-------------------------"

"LMED Method: This method will be used with known inlet and outlet temperatures for

both air and refrigerant sides"

Q_dot=U*A_out*LMED

LMED=((h_a_in-h_ref_out)-(h_a_out-h_ref_in))/ln((h_a_in-h_ref_out)/(h_a_out-

h_ref_in))

"Use trendline equation to calculated enthalpy"

T_ref_in_si=ConvertTemp(F,C,T_ref_in)

T_ref_out_si=ConvertTemp(F,C,T_ref_out)

"The function of the enthalpy is:

Function H_ref(T)

H_ref:=3.56*T-38

End"

h_ref_in_si=H_ref(T_ref_in_si)

h_ref_in=h_ref_in_si*convert(kJ/kg,Btu/lbm)

h_ref_out_si=H_ref(T_ref_out_si)

h_ref_out=h_ref_out_si*convert(kJ/kg,Btu/lbm)

"NTU Method: This method will be used with inlet temperatures of both air and refrigerant sides"

C_min=min(C_ref,C_a)

C_max=max(C_ref,C_a)

C_r=C_min/C_max

C_ref=m_ref*c_p_ref

C_a=m_a*c_pf_a

epsilon=HX('crossflow_one_unmixed',NTU,C_a,C_ref,'epsilon')

NTU=U*A_out/C_min

{T_a_out=T_ref_in}

"This can be used as initial guess when the program can not converge"

c_pf_a=(h_a_in-h_a_out)/(T_a_wb_in-T_a_wb_out)

T_a_wb_out=WetBulb(AirH2O,T=T_a_out,r=1,P=P_atm)

T_a_out=Temperature(AirH2O,h=h_a_out,r=1,P=P_atm)

"Energy balance"

Q_dot=C_ref*deltaT_ref

Q_dot= m_a*(h_a_in-h_a_out)

"Use the following equations for uncertainty analysis"

{Q_dot_ref=C_ref*deltaT_ref

Q_dot_a=m_a*(h_a_in-h_a_out)

Q_dot=(Q_dot_a+Q_dot_ref)/2}

APPENDIX D   LABVIEW PROGRAM PROCEDURES

D-1   Start-up operational procedures

A)   Check all the powers to the equipment, chiller, fan, dew point meter, hot water pump, gear pump heater, flow meter and tank mixer.

B)   Run the Labview program

Open the file: C:\frost experiments\control program for the frosting experiments. When you open the program, the following page appears as shown in figure D-1. Give the test name and then click "run" button to create a new folder to store the data. The historical commands and program information are also recorded in the new folder. Once running it, the two lights are on the control board as showed in figure D-2. This means the hot water pump is on and valves in the chilled water loop are in the correct position.
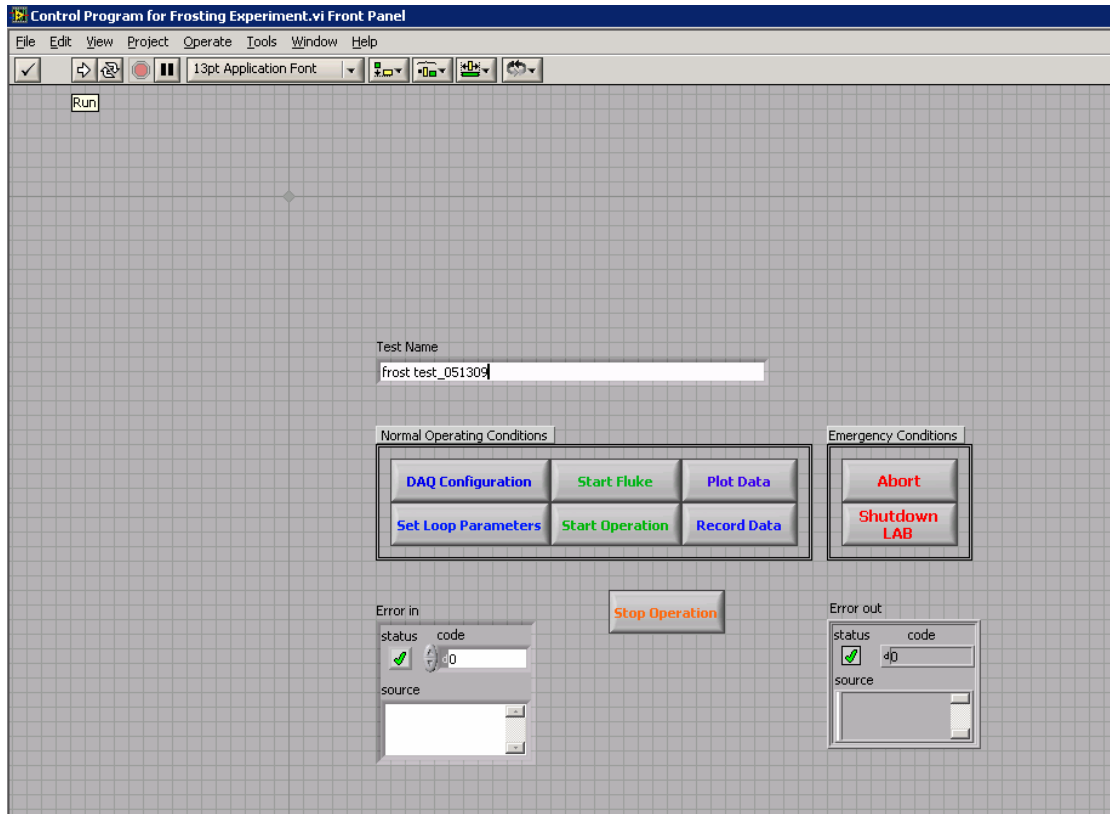
Figure D-1 Labview interface
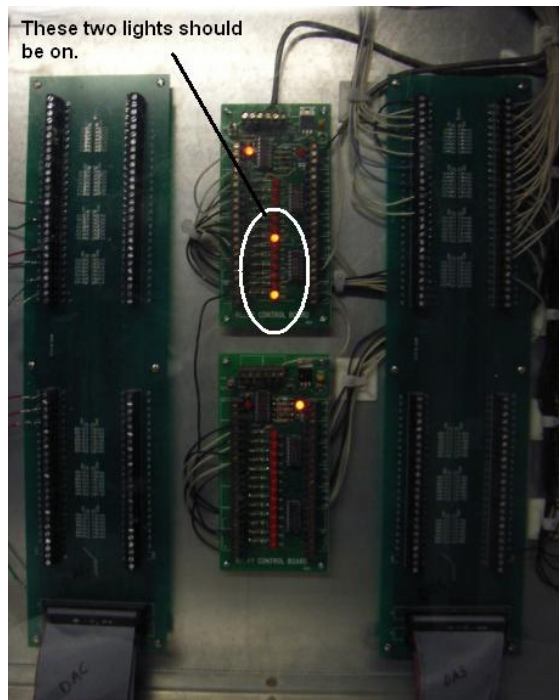
Figure D-2 Control board of the DAQ system in the air flow lab

When Fluke is ready to scan the data, it should show a status as in figure D-3. If the program was improperly closed before, it is necessary to check the FLUKE system. For example, if it performs as in figure D-4, the Fluke is still scanning data from Labview. In this case, the Fluke needs to be reset. Reset procedure is as following: click "LOCAL" button, "SCAN", using ▼ to turn off the scan procedure, "ENTER". After that, the Fluke should look like the image of figure D-3.

Figure D-3 Fluke –ready to scan status

Figure D-4 Fluke –error status (need to reset Fluke before start operation)

C) DAQ system program

Figure D-5 shows the main page of DAQ system program. The following steps are required to start a test:

1) Browse for "Data acquisition frost experiments.cfg" and read the .cfg file;

2) Read module 11, 12, 13 and make sure the check marks are on for "External Trigger");

3) Initialize the program;

4) Stop the execution one time.

If the program shows any error at this part, the most possible reason is that the Fluke is still performing the initial scan of the data from the program. Check the Fluke status and reset the Fluke system if necessary.
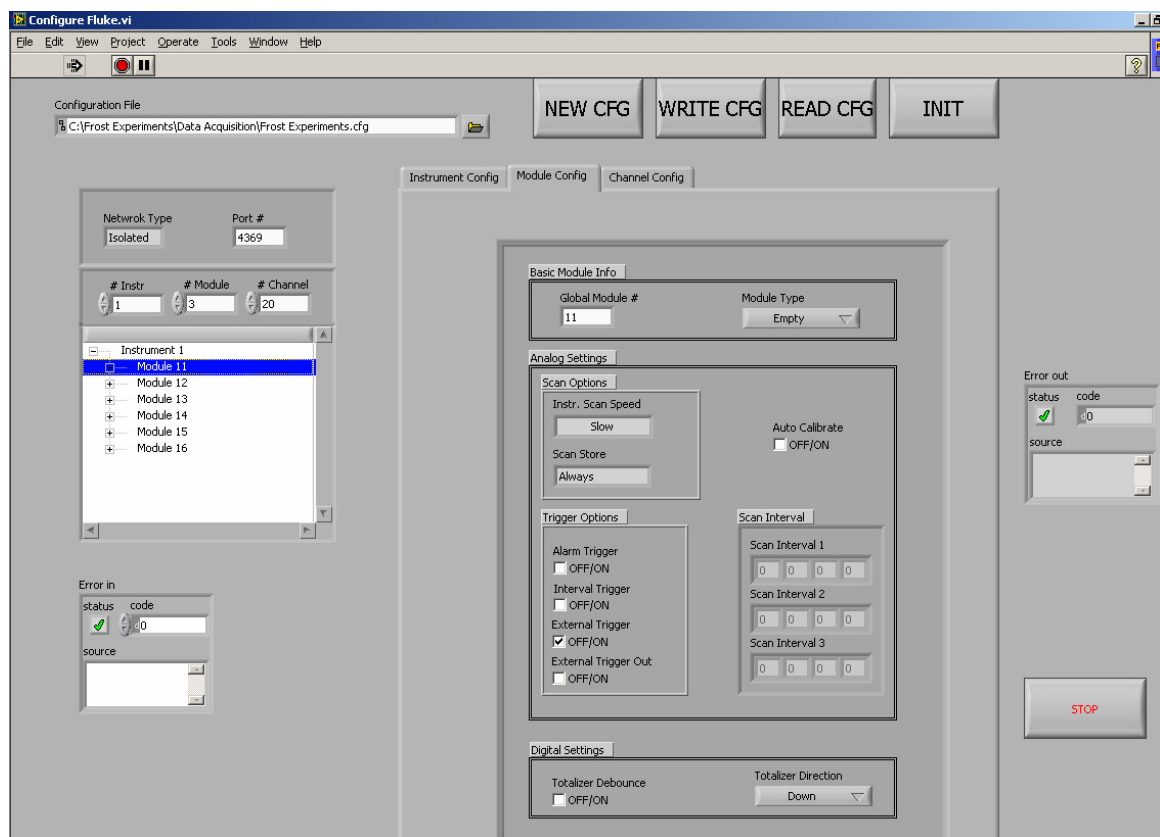
Figure D-5 DAQ configuration

D) Start data acquisition using Fluke system

Once the initialization phase described in step C above is completed. The following page will appear with the read out of all channels. The channel assignments are listed in Appendix F.
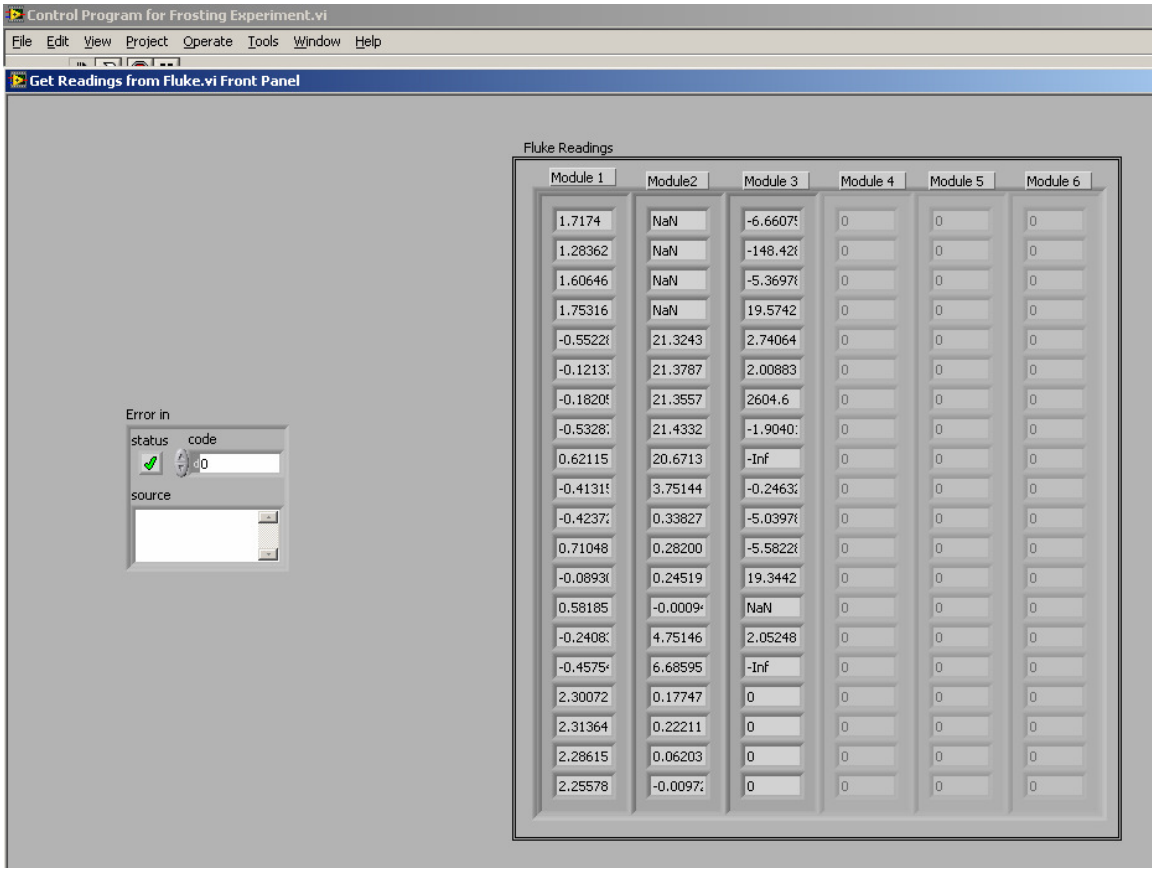
Figure D-6 Fluke readout

E) Plot the measurements during the experiments

Once running the experiment, both air and refrigerant side data, for example dry- and wet-bulb temperatures, air flow rate, refrigerant inlet and outlet temperatures, refrigerant flow rate, are plotted in the windows as functions of time. They are shown in the figure below:
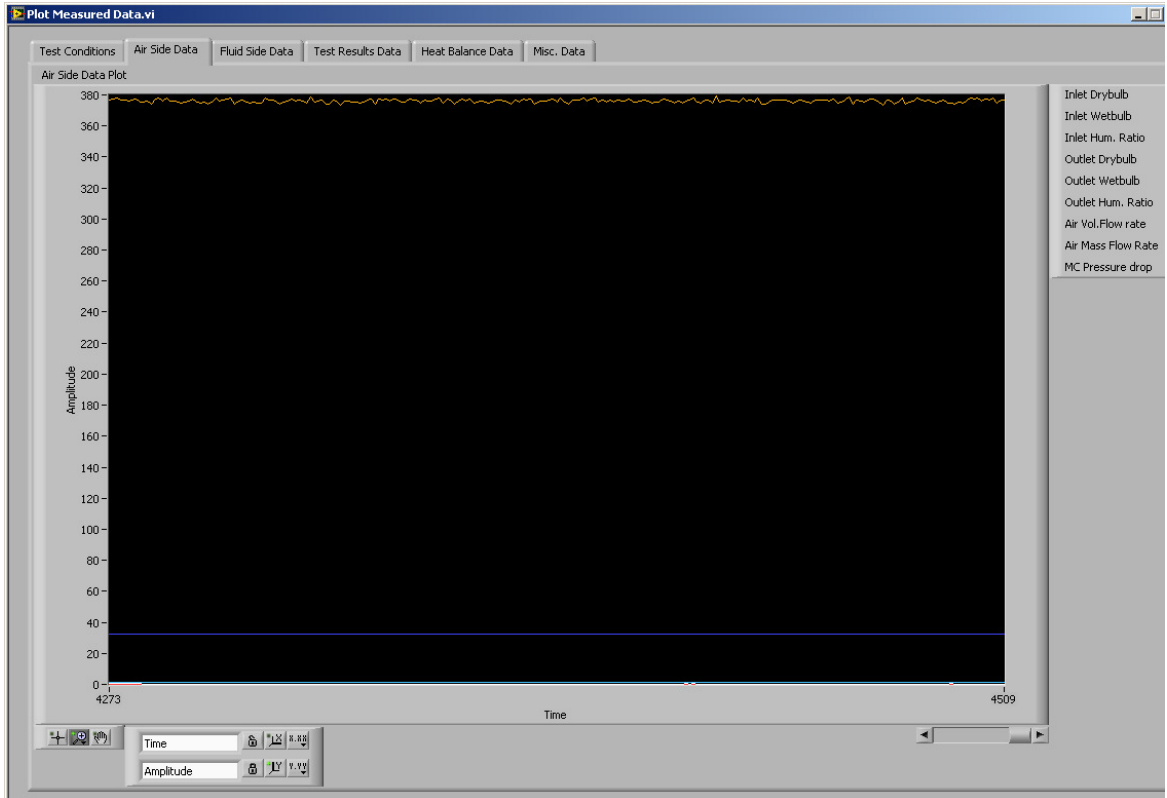
Figure D-7 Data plot

F) Set control variables during the experiments

1) Loop control parameters:

The loop control parameters are shown in figure D-8. In this program, control tanks actually means control of the heaters immersed inside the tanks. Both the heaters can be selected to be controlled either automatically or manually. If the heater in the tank is selected to be controlled automatically, the manual button should be turned off and set point needs to be given. If the tank is needed to run manually, the voltage needs to be adjusted from 0 to 10 (10 means the heater always on, while 0 means the heater off) based on the required heating capacity.
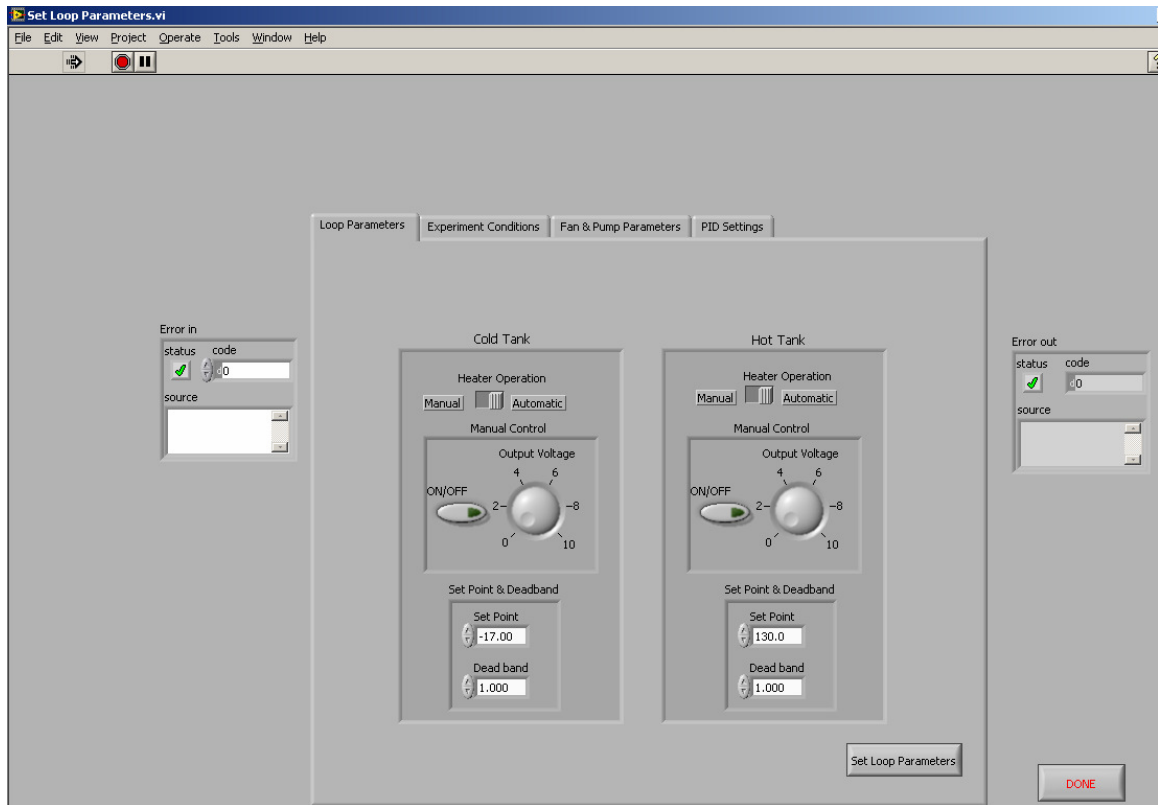
Figure D-8   Loop parameters

2) Set of refrigerant-side and air-side experimental conditions

As shown in figure D-9, the air temperature and air flow rate must be set to certain set points, such as 35 ºF /33 ºF for dry-bulb and wet-bulb temperatures and 200 cfm for the air flow rate. Refrigerant flow rate and refrigerant inlet temperature are input as additional information. These two values will not affect any control of the equipment and sensors. From air dry bulb temperature set point, the flow rate of water in the re-heating coil is controlled, while the air flow set point adjusts the fan speed. Both dry and wet bulb temperatures set points are used to calculated the relative humidity at the inlet of the test section.
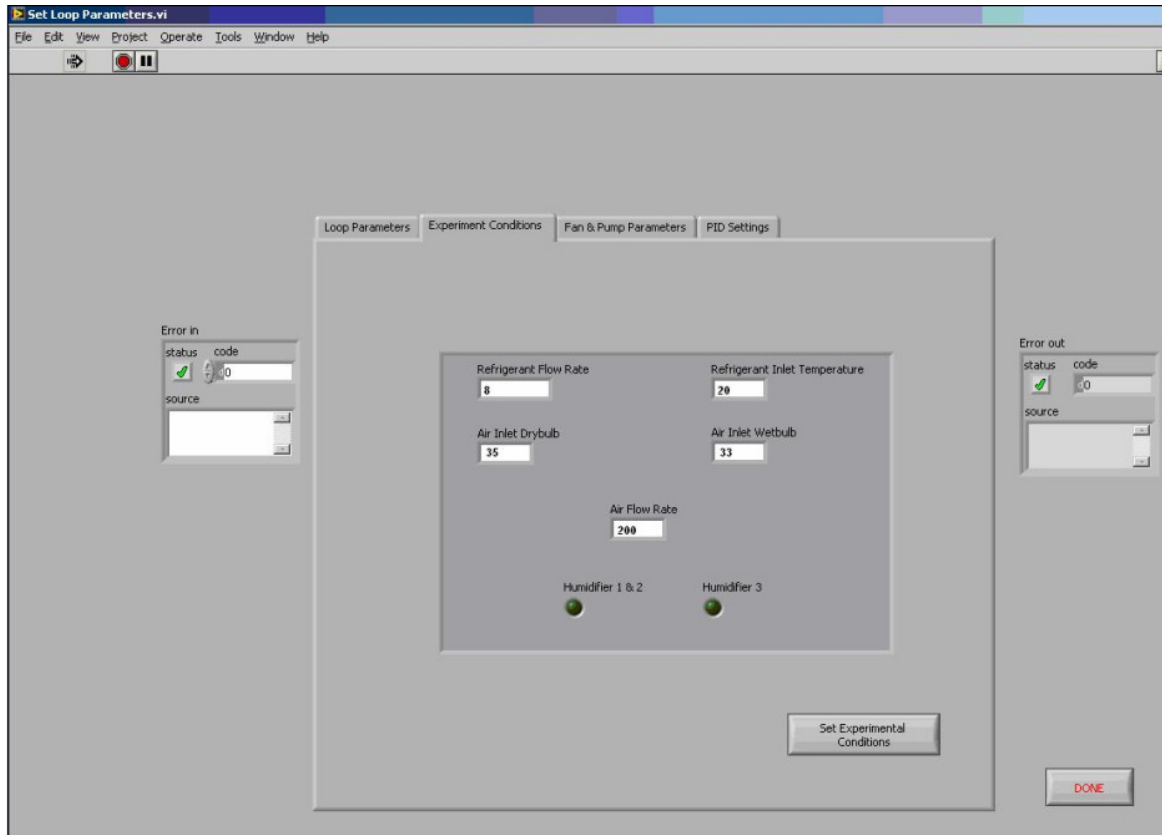
Figure D-9   Experiment conditions

3) Fan and gear pump set points

Figure D-10 shows the setting for the fan in the air side and gear pump in the refrigerant side.

Like the heaters case, the fan and the gear pump can also be selected to run either manually or automatically. The fan is able to directly adjust its set point depending on the air temperature set point input in the previous window "experimental conditions" if choose to run automatically. The corresponding drive needs to be set from "HAND" to "AUTO" based on the selection in Labview program.

If the gear pump is turned on manually, the pump should first run with a small flow rate. In order not to block two check valves, all flow valves are closed before turning the pump on. Once the pump starts running at a low flow rate, and the check

valves open, the two flow valves in either hot or cold tank loops should be opened immediately. The voltage is then adjusted to increase the refrigerant flow rate. In the frosting and defrosting experiment, it is not necessary to run the gear pump in automatic, since the refrigerant flow rate is completely independent from the inlet refrigerant temperature set point. Thus, the gear pump is always controlled manually. It is recommended to start the pump using a 2V output signal which corresponds to approximately 270 RPM and about 2 GPM refrigerant flow rate as shown in figure D-10 below. The flow rate is changed by adjusting output voltage.
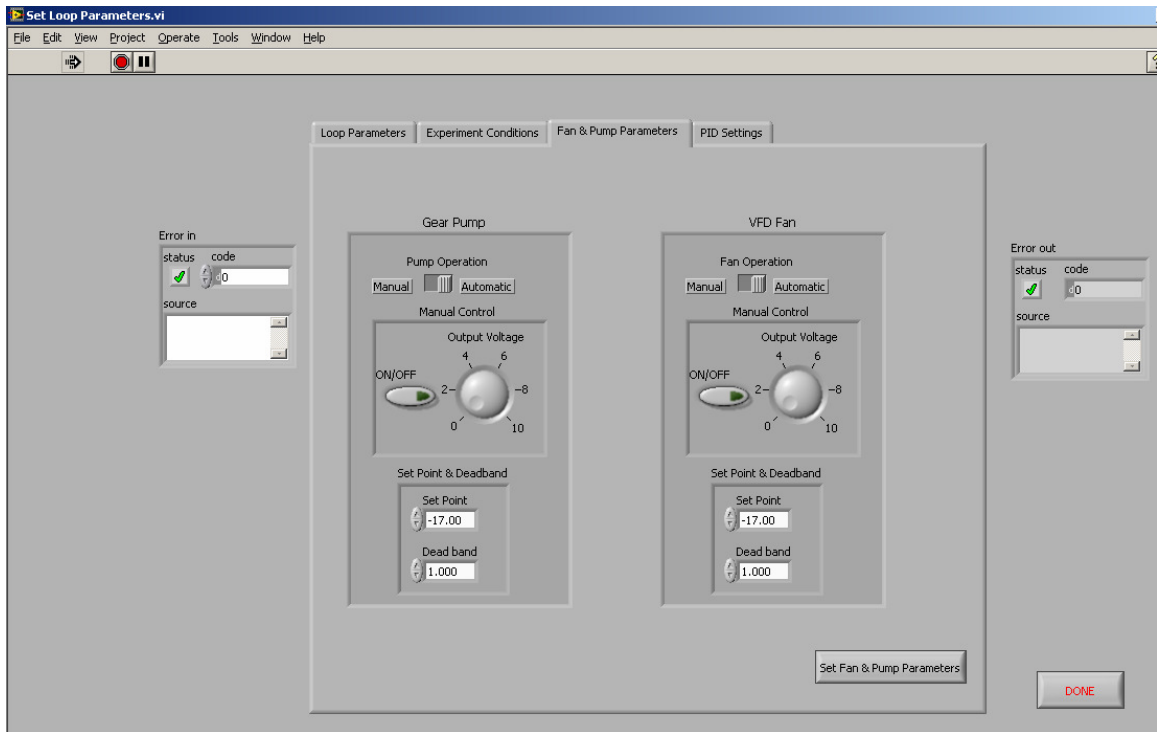
Figure D-10 Fan and the gear pump

4) Proportional–integral–derivative (PID) control settings

It is necessary to appropriately choose the PID controller parameters in order to achieve steady state and stable experimental conditions. The PID settings for the cold tank heater, hot tank heater and air flow are shown in figure D-11 below.
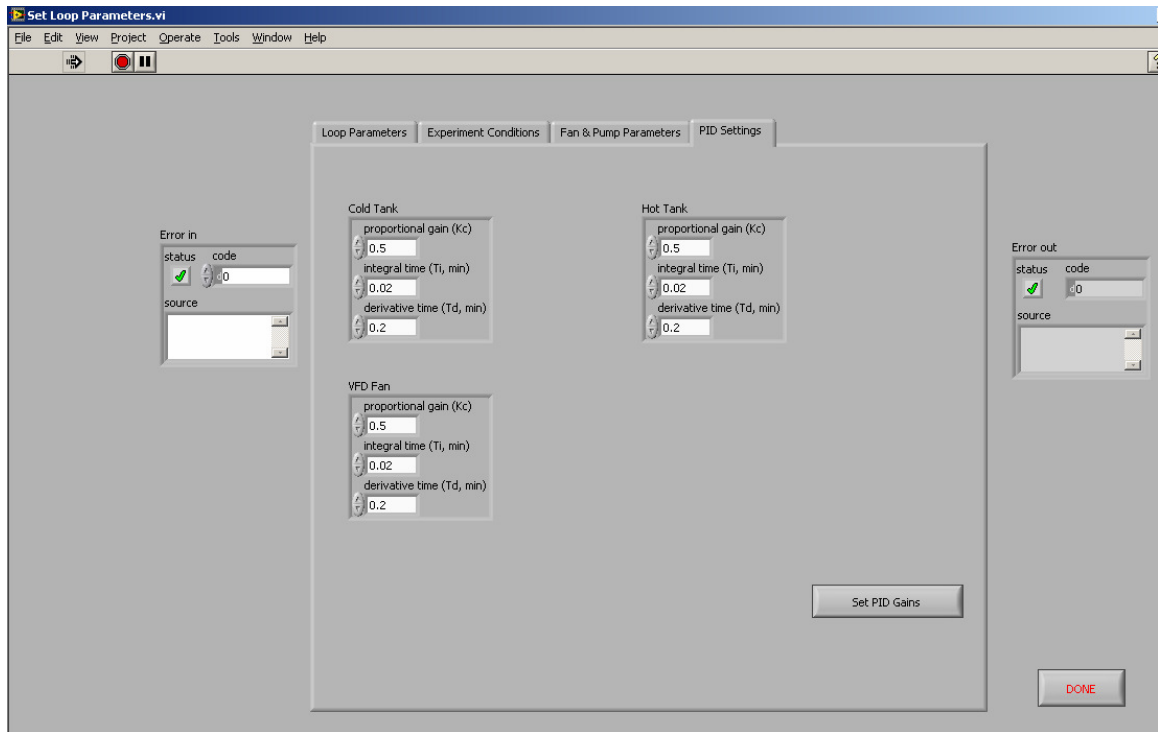
Figure D-11 PID settings

DONE with the loop parameters

G) Start-up operational procedures

The cooling chiller must be turned on and set by using its own control pad. This can be done before starting the Labview program. The fluid leaving temperature set point is input to the control pad of the chiller.

H) Check the gear pump and the heat pump systems

Check that the RPM in the gear pump controller is at least 270 GPM. If the pump runs, open the two valves in the cold and hot tank loops. Turn on the mixer in the tank. Check the hot water pump by touching the second motor from the left on top of the water tank. If it is vibrating, the hot water pump is on.

I) Record data

177

The measurements will be recorded and stored in the file created in the first step of this section. The sample rate is every 4 seconds. To decrease the volume of data points stored in the file, it is recommended to record data only once the chiller fluid leaving temperature reaches its set point.

Figure D-12 is the flow chart of the start procedure of the whole test facility by using Labview program.

D-2 Turn-off operational procedures

A) Stop recording data

Right click and reinitialize data.

B) Shut down the chiller

The chiller must be off before stop the operation. This is because

C) Stop operation

The fan, gear pump, hot water pump and heater are off. In the chilled water loop, the bypass valve opens and main loop valve is closed.

D) Close the two valves in the cart and shut off the tank mixer.

In order not to cause block problem in the check valve, the valves in the temperature control unit should be closed when the system is not running.
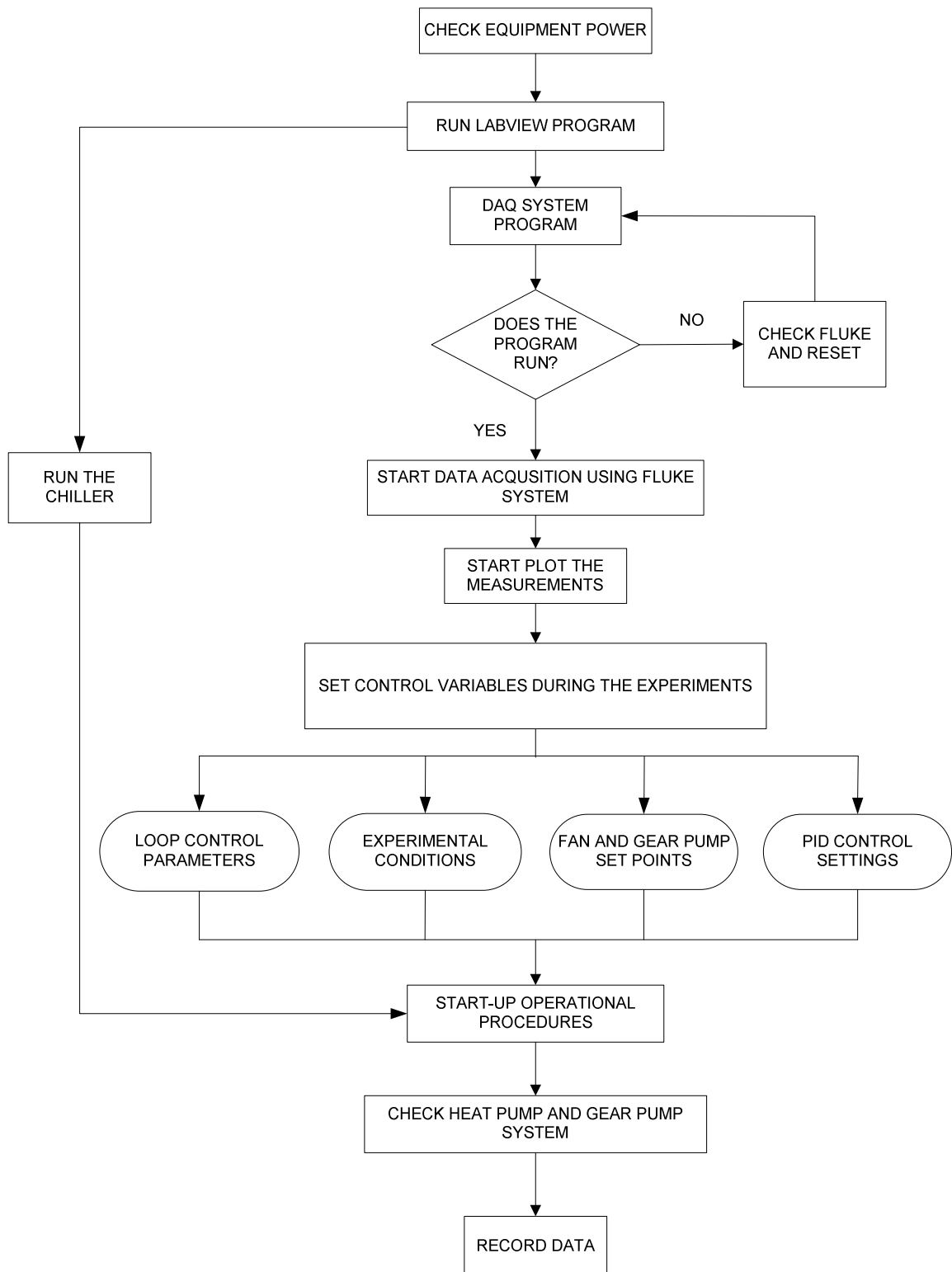
E) Disconnect the equipment power.

Figure D-12   Labview "Start-up" procedure for the frost wind tunnel in the OSU air

flow lab

179

APPENDIX E   CHILLER START UP, RUN AND TURN OFF PROCEDURES

E-1   Chiller start up procedure

A) Before turning on the chiller:

1) Make sure the chiller power has been turned on for at least two hours before enable the chiller compressor and process pump. This is because the crank heater in the compressor must be hot to separate refrigerant and oil and avoid oil mixture with the refrigerant during the first minutes of compressor operation.

2) Check that the chilled water supply valves at the corner of the air flow lab. The valve in the bypass line should be closed and the main line valve should be open. If it is not so, turning on the labview program first.

B) Turn on the chiller if the valves are in right position:

1) Turn on the recirculation pump and switch to "HAND".

2) Turn on the TC power pump.

3) Open the valves on the dynalene process loop. These valves need to keep closed before the pump on, or the liquid would drain to the chiller tank, cause cavitation issue for the process pump.

4) Run the chiller.

5) Turn on the chiller compressor. You may need to wait few minutes (no more than 2 minutes) for the compressor to actually start. The time delay imposed by its own control.

6) Switch the circulation pump from "HAND" to "AUTO".

C) Start the Labview data acquisition program

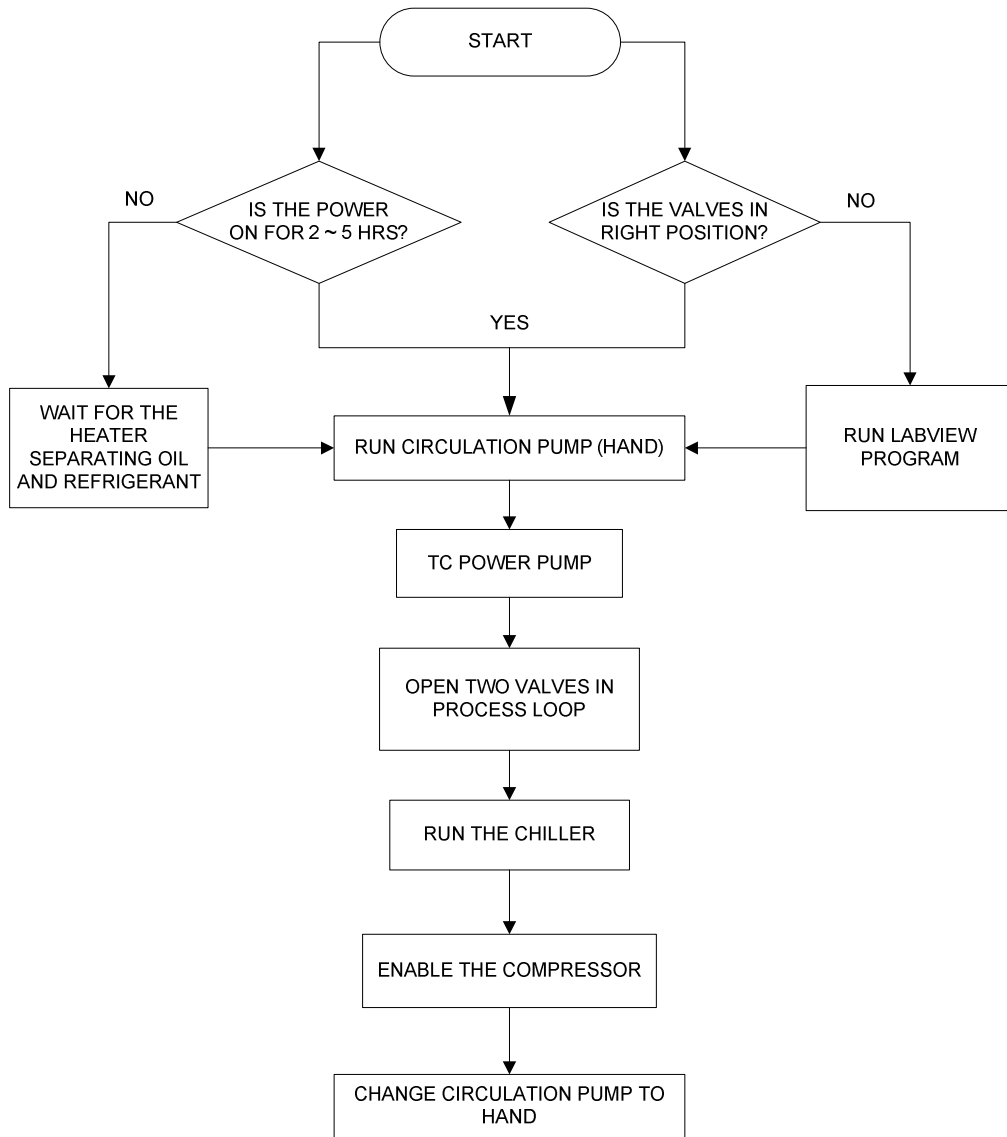Figure E-1 is the flow chart of running the chiller.

Figure E-1   Chiller procedure

E-2   Turn off chiller procedure

A)   Switch off the chiller compressor.

B)   Close the valves in inlet and outlet loop, and then turn off the recirculation and process pump.

C)   Turn off the pumps and switch off the chiller.

D)   Check alarm status from time to time. If there is an alarm on, stop the chiller as soon as possible. If there is an emergency situation, press the "EMERGENCY" button directly near the chiller control board to turn off the chiller at once.

E-3   Change the set point of leaving fluid temperatures

The temperature of process fluid (Dynalene HC40) can be adjusted in the range from -20 ºF to 130 ºF. The temperature can be set by entering the set point to the control pad of the chiller. The procedure gives as follows:

A)   Check the set point from the control panel. If need to be changed, press ⟲ and use ▲ ▼ to adjust the set point temperatures.

B)   Change the upper and lower temperature limits.

1) Press and hold ⟲ and press any ▲ ▼ at the same time.

2) Choose "SETUP SELECT", ⟲

3) Enter password: "1", ⟲

4) Using ⟲ to select changing subject. Upper and lower limits are the two values that need to be adjusted with the set point. Press ⟲ to find "SPUL" (set point upper limit). Use ▲ ▼ to set the upper limit 3 degrees higher than the set point. Still use ⟲ to select "SPLL" (set point lower limit) and set it 3 degrees below.

5) Hold ⟲ and press any ▲ ▼ to get back to "SET P SELECT" (set point selection).

6) Go to "OPER SELECT" by using ▲ ▼, ⟲.

C)   Change evaporator set point by using the upper panel if necessary. By default the evaporator set point is at -28 ºF, which is the lowest leaving fluid temperature the chiller is able to achieve.

APPENDIX F: CHANNEL ASSIGNMENTS FOR FLUKE

Module number	Channel number	Type of Measurement	Units	Location	Source	Channel Setting
101	10101	Temp (Drybulb)	C	Inlet to MC	Thermocouple	THERM
101	10102	Temp (Drybulb)	C	Inlet to MC	Thermocouple	THERM
101	10103	Temp (Drybulb)	C	Inlet to MC	Thermocouple	THERM
101	10104	Temp (Drybulb)	C	Inlet to MC	Thermocouple	THERM
101	10105	Temp (Drybulb)	C	Inlet to MC	Thermocouple	THERM
101	10106	Temp (Drybulb)	C	Inlet to MC	Thermocouple	THERM
101	10107	Temp (Drybulb)	C	Inlet to MC	Thermocouple	THERM
101	10108	Temp (Drybulb)	C	Inlet to MC	Thermocouple	THERM
101	10109	Temp (Drybulb)	C	Inlet to MC	Thermocouple	THERM
101	10110	Temp (Drybulb)	C	Inlet to MC	Thermocouple	THERM
101	10111	Temp (Drybulb)	C	Inlet to MC	Thermocouple	THERM
101	10112	Temp (Drybulb)	C	Inlet to MC	Thermocouple	THERM
101	10113	Temp (Drybulb)	C	Inlet to MC	Thermocouple	THERM
101	10114	Temp (Drybulb)	C	Inlet to MC	Thermocouple	THERM
101	10115	Temp (Drybulb)	C	Inlet to MC	Thermocouple	THERM
101	10116	Temp (Drybulb)	C	Inlet to MC	Thermocouple	THERM
101	10117	Temp (Dewpoint)	C	Outlet of MC	Chilled Mirror	VDC
102	10210	Temp (Dewpoint)	C	Inlet to MC	Chilled Mirror	VDC
102	10211	Temp (Drybulb)	C	Nozzle	Thermocouple	THERM
102	10212	Temp (Drybulb)	C	Outlet to MC	Thermocouple	THERM
102	10213	Temp (Drybulb)	C	Outlet to MC	Thermocouple	THERM

Continued Appendix F

Module number	Channel number	Type of Measurement	Units	Location	Source	Channel Setting
102	10214	Temp (Drybulb)	C	Outlet to MC	Thermocouple	THERM
102	10215	Temp (Drybulb)	C	Outlet to MC	Thermocouple	THERM
102	10216	Temp (Drybulb)	C	Outlet to MC	Thermocouple	THERM
102	10217	Temp (Drybulb)	C	Outlet to MC	Thermocouple	THERM
102	10218	Temp (Drybulb)	C	Outlet to MC	Thermocouple	THERM
102	10219	Temp (Drybulb)	C	Outlet to MC	Thermocouple	THERM
102	10220	Temp (Drybulb)	C	Outlet to MC	Thermocouple	THERM
103	10301	Temp (Fluid)	C	CC Inlet	Probe	THERM
103	10302	Temp (Air)	C	MC Out	RTD	RTD
103	10303	Temp (Fluid)	C	Cold Tank	Probe	THERM
103	10304	Temp (Fluid)	C	Hot Tank	Probe	THERM
103	10305	Pressure (Delta P)	Pa	Nozzle	Setra Pressure Transducer	VDC
103	10306	Pressure (Delta P)	Pa	Microchannel	Setra Pressure Transducer	VDC
103	10307	Mass Flow	Kg/s	Cart	Micromotion	FREQ
103	10308	Temp (Liquid)	C	MC In	RTD	RTD
103	10309	Temp (Liquid)	C	MC Out	RTD	RTD
103	10310	Temp (Air)	C	MC In	RTD	RTD
103	10311	Temp (Liquid)	C	To MC	Probe	THERM
103	10312	Temp (Liquid)	C	From MC	Probe	THERM
103	10313	Temp (Liquid)	C	To Cold Tank	Probe	THERM
103	10314	Temp (Liquid)	C	To Hot Tank	Probe	THERM
103	10315	Temp (Liquid)	C	CC outlet	Probe	THERM

VITA

SHANSHAN CAI

Candidate for the Degree of

Master of Science

Thesis: DESIGN OF AN EXPERIMENTAL FACILITY FOR FROST GROWTH

STUDY IN MICROCHANNEL HEAT EXCHANGERS

Major Field: Mechanical Engineering

Biographical:

Personal Data: Born in Wuhan, China on September 27, 1985.

Education: Received a Bachelor of Science degree in Building Environment and Equipment Engineering from Huazhong University of Science and Technology, Wuhan, China in June 2007. Completed the requirements for the Master of Science with a major in Mechanical Engineering at Oklahoma State University, Stillwater, Oklahoma in July 2009.

Experience: Employed by Oklahoma State University, Department of Mechanical and Aerospace Engineering, as a graduate research and teaching assistant from August 2007 to present.

Professional Memberships: None

Name: SHANSHAN CAI   Date of Degree: July, 2009

Institution: Oklahoma State University   Location: OKC or Stillwater, Oklahoma

Title of Study: DESIGN OF AN EXPERIMENTAL FACILITY FOR FROST GROWTH
              STUDY IN MICROCHANNEL HEAT EXCHANGERS

Pages in Study: 184   Candidate for the Degree of Master of Science

Major Field: Mechanical Engineering

Scope and Method of Study: This report focused on the new experimental methodology
       developed to investigate the frost and defrost thermal hydraulic performances of
       louvered folded fin microchannel heat exchangers under initial frost cycle, defrost
       cycle, and subsequent re-frost cycles. The required laboratory conditions are
       35/33 ºF dry-/wet-bulb temperature, with the air velocity around 100 ~ 300 fpm.
       In the air side, the required conditions were reached by a humidification, a
       cooling and a re-heating process with a fan, a refrigeration coil, a humidifier and a
       re-heating coil. In the refrigerant side, the required inlet coolant temperature was
       controlled by an automatically controlled heater and a plate heat exchanger
       connected with the chiller. The frost accumulation was measured by a precision
       scale for frost weight, and a videoscope for frost thickness. Uncertainties on U
       and h_{out} were investigated based on both precision and bias uncertainties. EES
       (Engineering Equation Solver) is the main simulation tool in this study.

Findings and Conclusions: A stable 35/33 ºF dry-/wet-bulb temperature condition can be
       reached with proper control of the chiller and refrigeration coil flow rate.
       Temperature variation in the air stream before the test evaporator was within 1.5
       ºF, which was an acceptable uniformity of the air flow. The uncertainties on heat
       transfer coefficient (U) and air side heat transfer coefficient (h_{out}) were calculated
       for both 1 ft x 1 ft microchannel and finned tube heat exchangers. For
       microchannel heat exchangers, the uncertainties on U are around ±7% in dry
       condition, ±10% for wet and ±15% for frost conditions. The uncertainties on h_{out}
       are 2% higher than U. For fin-and-tube heat exchangers, the uncertainties are
       much higher. Recommended flow rates are 300 to 500 cfm in the air side and 3 to
       5 gpm in the refrigerant side. Avoid frost accumulation on the refrigeration coil is
       the main problem that needs to be solved in the future.

ADVISER'S APPROVAL: Dr. Lorenzo Cremaschi